**Представляем
научные достижения миру.
Естественные науки**

Saratov State University

Presenting
Academic Achievements to the World.
Natural Science

Papers from the conference for young scientists
«Presenting Academic Achievements to the World»

March 14–15, 2012
Saratov

I s s u e 3

Saratov
Saratov University Press
2012

Саратовский государственный университет им. Н. Г. Чернышевского

Представляем научные достижения миру. Естественные науки

Материалы научной конференции молодых ученых
«Presenting Academic Achievements to the World»

Март 14–15, 2012
Саратов

В ы п у с к   3

П71 **Представляем научные достижения миру. Естествен-**
ные науки : материалы научной конференции молодых ученых
«Presenting Academic Achievements to the World». – Саратов : Изд-
во Сарат. ун-та, 2012. – Вып. 3 – 144 с. : ил.

В данном сборнике опубликованы материалы участников секции естественных наук научной конференции молодых ученых «Presenting Academic Achievements to the World», которая состоялась в Саратовском государственном университете 14-15 марта 2012 года. В сборник включены статьи с результатами исследований в области физики, химии, географии, геологии и информационных технологий.

This publication assembles papers given at the conference for young scientists «Presenting Academic Achievements to the World» which was held in March 14-15, 2012 at Saratov State University. The articles present the results in such fields of natural science as Physics, Chemistry, Geography, Geology and Information Technology.

Работа издана в авторской редакции

LITHOFACIES AND PETROPHYSICAL FORMATION CHARACTERISTICS OF THE HORIZON B2 IN THE KROTOVSKY STRETCH (SARATOV REGION)

K. M. Antonov, S. V. Astarkin

Saratov State University

The southern slope of the Zhigulevsk arch is one of promising directions for searches of small and average oil fields. Due to industrial inflows of hydrocarbon in terrigenous depositions of Bobrikovskian horizon (B2) there have been struck such fields as Krotovsk, Bogorodsk, Ostroluksk, etc. During Bobrikovskian time in this region various genetic types of depositions were forming in conditions of short-term transgressions and regressions. This has a major influence on oil-and-gas-bearing capacity of the investigated area. Hence, a comprehensive study of Bobrikovskian horizon formations is of great theoretical and practical importance.

This article is based on the research data from lithofacies and petrophysical investigations of core material from four new holes drilled within the Krotovsk stretch (the southern slope of the Zhigulevsk arch, Volga river basin in Saratov region). The purpose of our research is to find out the conditions of formation, geological aspects of voids and structure pattern of productive depositions in Bobrikovskian horizon on a sedimentary section.

The complex of lithofacies studies includes:

• Stratified megascopical description of drill core columns with control study of single core samples with the use of the binocular microscope;

• Lithologic study of core samples that have been used for defining reservoir properties with the use of the binocular microscope;

• Mineralogical investigation of primary formations in standard microsections;

- X-ray and mineralogical study of primary formations and clay minerals;
- While describing the core we put an emphasis on its fracture, cavern porosity, and void structure;
- While describing the core layer-by-layer we put an emphasis on textural characteristics of primary formations, contacts conditions between the layers with different lithological characteristics.

The main targets of the reservoir formation petrophysical studies of horizon B2 are to:
- define PIGN;
- define absolute gas-permeability under atmospheric conditions;
- define mineralogical and bulk density;
- define electrical resistivity, the velocity of longitudinal waves and the open porosity in the temperature and pressure conditions;
- carry out capillary study to assess the residual water saturation and the saturation parameters.

In the investigated holes, the formation of Bobrikovskian horizon rest unconformably on underlying carbonate rocks of late Tournaisian age. The junction is ragged and corrugated. Chalkstones on junction are strongly pyritised and also there is typical hard ground, which generated due to fast transgression of Bobrikovskian sea basin after late Tournaisian regression. Bobrikovskian horizon depositions are bridged by clays and mudstones of the Tula horizon of middle Visean sublevel.

The cross-section of Bobrikovskian horizon is represented by a stratum of interlayering mudstones, siltstones and sandstones.

Mudstones black and dark grey, micro- and thinly-horizontaly laminated, micaceous. In the district of well borings №3 and №4 mudstones are strongly fissured, with lenticles of pyrite up to 2-8 meters. Bedding surfaces contain coalised plant remains and plates of muscovite. There are light grey round-circular lenticles of clay-coal composition in size to 1.5-5, which occur in mudstones sporadically.

Siltstones are dark grey, argillaceous, often sandy and quartzous with thin parallel horizontal and gentle diagonal bedding and argillaceous cement. Lamination is caused by the presence of thin distorted lenticles, pays of grey mudstone and close-grained sand lenses with argillaceous cement. The formation is pyritised. The bed joints are strongly distorted and contain multiple plates of muscovite and micropays of carbonaceous material.

Sandstones are quartzous, grey and sometimes brownish due to hydrocarbon imbibitions. They vary from fine-grained to coarse-grained with laminated texture which carries pyrite nodules on separate leases. Lamination is horizontal, corrugated and slightly loosened by bioturbation occurrences. Stratification is due to the presence of multiple lenticels and pays (thickness up to 1.5-2mm) of silty-argillaceous-carbonaceous and argillaceous-carbonaceous compositions. Stratification planes are covered by black membranes and large abundant scales of muscovite.

The classic material is introduced by subrounded, angular, isometric and elongated quartz grains of size about 0.03-0.25mm (with prevalence of grains about 0.15-0.2mm). The borders between quartz grains contain conformal, introductional and contactive joints. The cement varies from dark-grey to black, it belongs to argillaceous-carbonaceous bazal-pore and to pore-membrane types, enriched by thin-scattered pyrite. The content of argillaceous-carbonaceous material varies from 5-10% up to 20-30%. On the leases deprived of argillaceous admixture, the sandstone is highly porous, quartz grains are slightly compressed with contact overlap.

In the lithofacies aspect the Bobrikovskian horizon formations in holes № 3 and №4 were reshaped in a more deep-water, no-flow area, than the area of hole №1 and №2 of the Krotovsk stretch. This conclusion is proved by a more argillaceous type of the cross-section, as well as the presence of multiple pyrite nodules, even in sand streaks, and those of coal seams. Such formation features are typical for stagnant, regenerative conditions of sedimentations, with addition of significant bulks of organic matter and hydrosulphuric contamination near bottom parts. Presence of silty and fine-grained sand streaks indicates that some insignificant hydrodynamic stiffening took place.

Textural features and structural characteristics indicate that depositions were reshaped in shallow marine conditions due to the rough sea and currents.

The sediment cross-section has a characteristic cyclic structure. Cyclites have a transgressive constitution, with granularity reduction up the section [Барабошкин, 2008]. There are clastic variations of medium size at the bottom of cyclites. The variations consist of sandstones with lentiforms and horizontal stratifications. At the middle layer cyclites contain siltstones with parallel horizontal and slight diagonal bedding, at top they contain thin-horizontal mudstones.

Reservoir formations are associated with the bases of cyclites and linked to middle-fine-grained sandstones. The capacity of sand streaks fluctuates from 0.9-1.5m to 6-6.5m. In sandstones voids are linked to an interparticle porosity. The reduction of voids is linked to penecontemporaneous processes: insignificant reactivation of quartz grains, incorporation and formation of conformal contacts. The quantity and type of argillaceous cement also influences the porosity value.

Within the investigated territory it is possible to mark four collector layers.

Layer I has thickness of 4.3m, and is characterized by porosity values of 19.06% and oil-and-gas saturations of 75.02%. It is presented only at a cross-section of the hole №2.

Layer II has thickness of 0.75m, porosity value of 23.1%, oil-and-gas saturation of 85.8%. The given layer is presented only at a cross-section of holes №1 and №2.

Layer III has thickness of 0.4m, porosity value of 20.6%, oil-and-gas saturations of 75.4 %. It is presented only at a cross-section of the hole №1.

Layer IV is found in cross-sections of all the holes drilled within the Krotovsk stretch. Its thickness fluctuates from 0.8m to 6.5m. Porosity varies from 16.4% to 25.7%, oil-and-gas saturation varies from 69.3% to 89.2%.

It should be noted, that layers I and II are associated with lithological screened accumulations, where reservoir formation (sandstone) is replaced by non-reservoir formation (mudstone). There is a deposit limited from different directions which is a sandy lenticle confined to the reservoir.

On the basis reasoning from complex lithological and petrophysical research of the core we have defined three litologo-petrophysical formation types (LPT).

LPT I is defined within the range of 1227-1236m and is introduced by sandstones of dark-brown colour. It is quartzous, irregularly argillaceous and broken-layered, probably bioturbated, irregularly pyritised, medium hard, with a hydrocarbonate smell. Calculated statistical particle-size indexes GSO, GMD, GAS, GEX [Фролов, 1993] are indicative of medium-grained composition, good grading, negative skew and excess quantity from 0.6 to 1.8.

LPT II is defined within the range of 1223-1227m and is introduced by sandstones of grey and brown colours. It is quartzous, layers are argillaceous, horizontally thin-falteringly laminated, pyritised, medium hard, with faint hydrocarbonate smell. Calculated statistical particle-size indexes are indicative of grain composition heterogeneity (from fine-grained to medium-grained) and different extent of grading (from good to medium), negative skew and excess quantity from 0.7 to 1.2

LPT III is defined within the range of 1220-1223m and is introduced by sandstones of dark brown colours. It is quartzous, irregularly argillaceous, lensly-broken-layered, easily broken with hand. It has a strong hydrocarbonate smell and is porous, fine-grained. The marked LPT III is characterized by fine-grained composition, good grading, negative skew and excess quantity from 1.1 to 1.4.

Particle-size analysis data is can be used for constructing genetic granulometric composition diagrams that show various facies environments (Fig. 1).

On the basis of our researches it is possible to draw the following conclusions: depositions of Bobrikovskian horizon were formed in shallow marine conditions and have a specific transgressive cyclic structure; reservoir formations are associated with the bases of sedimentary cycles and linked to middle-fine-grained sandstones.

REFERENCES

1. *Барабошкин Е. Ю.* Практическая седиментология (терригенные коллектора). М. : ХЕРИОТ-ВАТТ ЦЕНТР, 2008. 155 с.
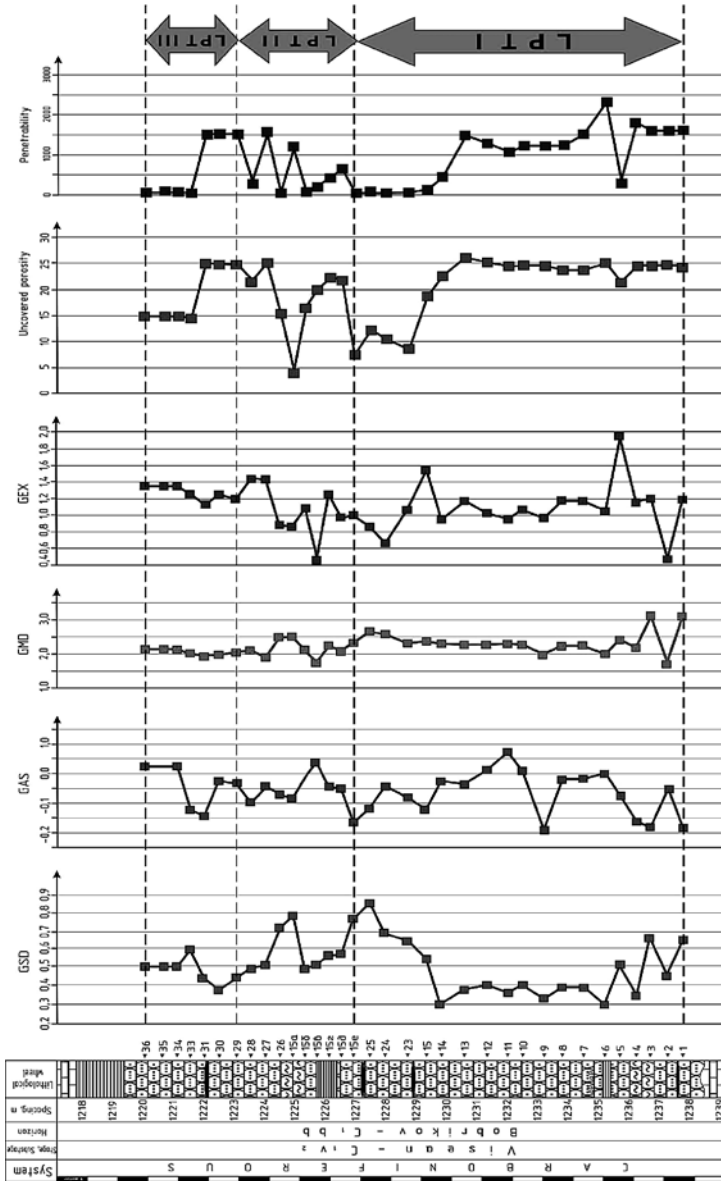2. *Фролов В. Т.* Литология : учебное пособие. Кн. 2. М. : Изд-во МГУ, 1993. 432 с.

Fig.1. Genetic and petrophysical formation characteristics B2

INDUCTANCE OF THE COIL CHANGED BY ELECTRIC FIELD

Ashanin M. E., Semenov A. A.

Saratov State University

INTRODUCTION

Basis of modern microelectronics are condenser and resistive element, and also inductance coils. The principle of transformation electric energy in the magnetic underlies work large quantity of devices. Inductance results from the magnetic field forming around a current-carrying conductor which tends to resist changes in the current. Electric current through the conductor creates a magnetic flux proportional to the current. A change in this current creates a corresponding change in magnetic flux which, in turn, by Faraday's law generates an electromotive force (EMF) that opposes this change in current. Inductance coils aren't the standardized products, unlike resistors and condensers. They are made for specific goals and have such parameters which are necessary for transformations of electric signals, currents and voltages.

Inductance for enough long solenoid is equal:

$$L = \mu_0 \mu \frac{N^2 S}{l} = \mu_0 \mu \; n^2 V,$$

where, μ_0 is a magnetic constant, μ is a relative magnetic constant, $n = N/l$ is a number of coils on length's unit, S is a square of coil section, l is a solenoid length, $V = S \times l$ is a solenoid volume. Inductance value is proportional to coils number, the occupied volume and magnetic constant. Formulas for calculation inductance of coils another form are more difficult and cannot have analytical form, but the basic proportions for all parameters remain. For change inductance of the coil it is necessary to change it physically. It means change number of coils, the square of cross-section cut or the solenoid length. It is impossible without intervention in design. This difficulty can be overcome, using the cores placed in the coil and capable to change its Q-factor. However, this method has lacks. Inductance change will depend on arrangement core in the coil.

MATERIAL AND METHODS

Constructional basis of the inductance coil is dielectric frame. The wire is reeled up on the frame in spiral form. The winding can be single-layered (fig. 1a), and multilayered (fig. 1b). In certain cases, the multilayered winding becomes partitioned (fig. 1c). Flat spiral inductance coils are applied in integrated schemes (fig. 1d).

Magnetic and not magnetic cores apply to inductance increase. Not magnetic cores use more often. The magnetic core in the coil concentrates a magnetic field and increases its frame. If we move core in frame it's change

inductance. Usually not magnetic cores are designed in circuited coil form inductively connected with the coil. Valuable property of not magnetic cores is their high stability. These cores are especially often applied in coils of generators HF and VHF devices. Not magnetic cores reduce inductance of the coil approximately on 3-5% and enter some additional active resistance. Q-factor of the coil decreases on 5-10%. Not magnetic cores made of copper or brass, and of dielectric on VHF. [1]
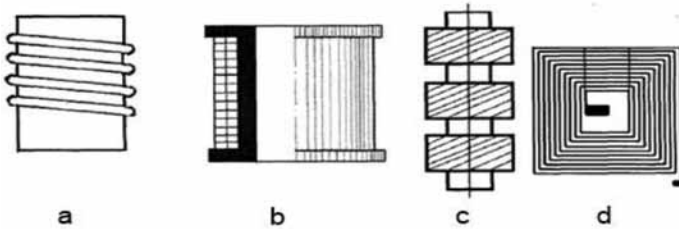

Fig. 1 Design of the inductance coil: a) single-layer; b) multilayer; c) multilayer partitioned; d) flat spiral.

Use as the pin-diode core became the revolutionary approach. When to pin-structure submit direct voltage area of intrinsic semiconductor sated with charge carriers which cooperate with a coil field. The primary variable magnetic field lead to vortical currents. Coil electromagnetic field will change under the vortical currents influence. This field change causes such effect, what would turn out if we change coil characteristics.[2]

Generally inductance value is influenced by physical characteristics the pin-diode material. Inductance is influenced by its electric and magnetic properties defined by its structure: electric conductivity, magnetic permeability, the geometrical form, defects [2, 3].
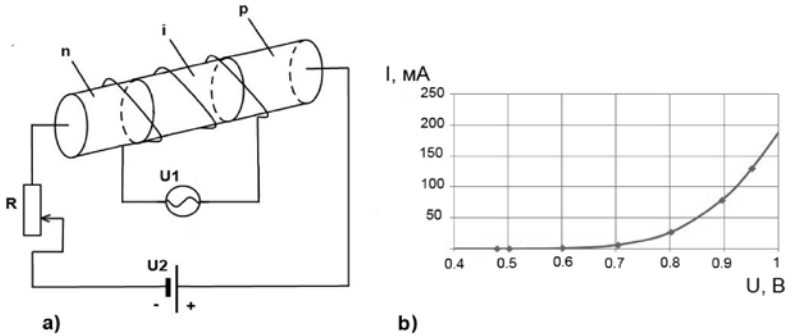

Fig. 2 a) pin-diode and coil schematic image; b) pin-diode current–voltage characteristic

Fig. 2a shows the pin-diode and coil schematic image. Voltage U1 create variable magnetic field which influence on free charges. The pin-diode is a diode with a wide, lightly doped 'near' intrinsic semiconductor region between a p-type semiconductor and an n-type semiconductor region. When the diode is forward biased, the injected carrier concentration is typically several orders of magnitude higher than the intrinsic level carrier concentration. Fig. 2b illustrates dependence I (U). Concentration of charge carriers in intrinsic semiconductor region depends on voltage U2. Quantity charge carriers can be changed on potentiometer R. Hence, vortical currents inductance will change too under the influence of voltage.

RESULTS AND THEIR DISCUSSION

It is necessary to notice that found out effect appreciably depends on parity of the coil and pin-structure geometrical sizes. If diameter coil wire is 10^-3 m, than dependence I(U) is weak. The great value has a choice of pin-diode exemplar. Diodes have considerable characteristics disorder within party. Also manufacturing coil quality influences on inductance and Q-factor.
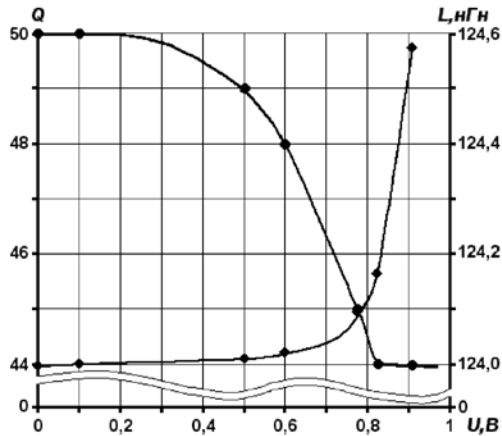

Fig. 3 Experimental characteristics of inductance coil: dependence Q-factor of displacement voltage value
(——♦——), dependence inductance of displacement voltage value (——♦——).

On fig. 3 we can see that Q-factor decreases if current proceeds through pin-structure.[4] Q-factor decreases in connection with power losses. It occurs to growth of number injected charge carriers. The pin-diode without displacement voltage decreases primary inductance value on 0.5%, but pin-diode with displacement voltage increases inductance value on 1-3%. Coil Q-factor decreases on 15÷18%.

CONCLUSION

Researches show that coil with the pin-diode as core is inductive element operated with electric field. These coils are interesting for constructing modern radio-electronic equipment, generators, modulators, filters, frequency-selective amplifiers VHF.

GRATITUDE

I most grateful to Semenov A. A. for help and valuable advices in article writing.

REFERENCES

1. *Баранов В. М., Карасевич А. М., Сарычев Г. А.* Диагностика материалов и конструкций. М.: Высш. шк., 2007. С. 293–294.
2. *Баранов В. М., Карасевич А. М., Сарычев Г. А.* Испытания и контроль качества материалов и конструкций. М.: Высш. шк., 2004. С. 186–189.
3. *Дьяконов В. П.* Лавинные транзисторы и тиристоры : Теория и применение. М.: Солон-Пресс ООО, 2008. 382 с.
4. *Семёнов А. А., Усанов Д. А.* Индуктивность, перестраиваемая электрическим полем // Изв. вузов. Электроника, 2009. № 4(78). С. 34–40.

DRIP IRRIGATION OF APPLE TREE NURSERIES IN THE NONCHERNOZEM ZONE

A. Y. Burmistrova

*The Russian State Agrarian University –
Moscow Agricultural Academy named after K. A. Timiryazev*

The Central Region is one of the most productive agricultural districts in the Nonchernozem zone where highly intensive orcharding is widely spread, about 80% of all perennial plantings being concentrated here (Синалаев, 2002). The production of planting stock influences greatly the fruit tree species and variety composition of orchards, as well as the size of cultivated areas and their productivity. Thus, nursery gardens are assumed to be the foundation of successful fruit-growing. In recent years the demand for high-quality trees has noticeably exceeded supply. Besides, young apple trees are the best-selling species in the Moscow region and account for 67,5% of the total number of sold nurslings (Waterman P., 1993, Иволгин, 2002).

Water supply during the whole growing season is known to be one of the most important factors affecting the normal growth and development of plants. Proper scheduling of irrigation is critical for nursery trees since they have no roots when planted (Waterman P., 1993). Also irrigation schedule contributes

to production costs and environmental safety when highly-profitable crops are cultivated. Irregular water supply can retard growth and development of the aboveground and underground plant parts. Drip irrigation enables to maintain the optimum soil moisture level in accordance with biological water requirements of an irrigated crop. Moreover, such an irrigation system can be fully automated (Нестерова, Зонн, Вейцман, 1973).

Drip irrigation is an irrigation method allowing water to drip slowly to the roots of plants, either onto the soil surface or directly onto the root zone, through a network of valves, pipes, tubing, and emitters. Drip irrigation is the most suitable one for row crops (vegetables, soft fruit), tree and vine crops when one or more emitters can be provided for each plant. Generally, only highly valuable crops are considered to be grown using drop irrigation because of the high capital costs spent on installing a drip system (Ахмедов, 2008).

The higher the temperature, the higher is the effectiveness of drip irrigation, as its efficiency increases alongside with the temperature growth and reaches its maximum in arid zones. On the other hand, humid climatic conditions in the Nonchernozem zone result in a highly-non-uniform distribution of rainfall throughout the vegetation season, which makes drip irrigation a promising watering method for fruit tree nurseries in the Central Region. Furthermore, according to some authors (Сабиров, Раззаков, 1990), in overly wet climate of the Netherlands, drip irrigation has been found to improve the survival rate of young trees and enhance the shoot growth by 30-40%.

To date there is no scientifically reliable recommendations on the irrigation rate to be applied in the field where the fruit tree nursery stock is produced (Шугай, 2005). The frequency and duration of each watering vary with the soil type and climatic conditions. Consequently, it is necessary to conduct researches within a particular region.

The main aim of the given research is to optimize the irrigation schedule for young apple trees cultivated under drip irrigation in the nursery gardens located in the Moscow region as well as to reveal how different levels of soil moisture affect their growth and development in order to provide the region with high-quality planting stock. The objectives involve the specification of the optimal soil moistening interval and its permanent maintenance in the root layer on the permanent basis. A root layer is the soil horizon where about 90% of all plant roots are concentrated. One more objective of the study is aimed at determining plant biological parameters such as the leaf area, the plant height, the stem diameter and examining the root system formation for evaluating the influence of various irrigation regimes on apple trees development.

In May 2011 a field experiment on developing the drip irrigation technology for young apple trees was launched in the nursery on the territory of the Michurin Garden, which belongs to the Russian State Agrarian University – Moscow Timiryazev Agricultural Academy. The two most popular varieties – *Beli Naliv* and *Medunitza* – which are widely grown in the Moscow region were chosen as the objects of research. The scions of the mentioned varieties

were grafted onto clonal semi-dwarf apple rootstocks 54-118 recommended for the Central Region due to such qualities as winter hardiness and drought resistance.

Drip irrigation is known to be suitable for most soils. On clay soils water must be supplied slowly to avoid surface water ponding and runoff. On sandy soils higher emitter discharge rates is required to ensure adequate lateral wetting of the soil. In the experimental plot the soil is characterized as the one of the sod-podzol type with middle loam texture on the covering silt.

The climate in the Moscow region is continental, but mild. There are no severe frosts or extremely hot periods, although certain deviations from the normal seasonal temperatures have become quite frequent in recent years. On average there are 194 days of above-zero and 103 days of below-zero temperature in Moscow annually. The field experiment can be conducted during the warm season, that is, during the vegetation period of plants. According to meteorological data, the first year of research (the year of 2011) was characterized by rather high temperatures and little rainfall, so it was quite droughty.

In the reclamation practice the soil moisture content is assumed to be expressed as a percentage of field capacity (FC). The average field capacity of the soil on the experimental plot amounts to 34,8% of absolutely dry soil weight.

Four different irrigation treatments have been used in the experiment, each being repeated three times. In the first variant the pre-irrigation moisture level was 70-75% of FC, which means that watering of apple trees started every time when the soil moisture content reduced to 70-75% of FC. The second irrigation treatment was characterized by lower pre-irrigation moisture content – 60-65% of FC. For the third variant a mixed irrigation regime was chosen: high water content was maintained in the soil during the first year of trees development with pre-irrigation moisture level 70-75% of FC and for the second and the third years it will be decreased to 60-65% of FC. This is due to higher susceptibility of young trees to the lack of moisture at the initial growth stages, as the root system has not formed yet. Consequently, in the first year of this investigation (2011) the conditions in the first and the third variants were the same. As a control, the treatment without irrigation was included in the experiment.

For the field experiment a special drip irrigation system has been designed and installed on the plot in the nursery garden. The drippers have a self-compensating system guaranteed by a silicon membrane that minimizes flow rate fluctuations when the working pressure changes. The dripper is equipped with an inlet filter to reduce potential blocking-up in case of low-quality water supply. The flow rate of one dripper is 3,8 liters per hour.

As far as one-year-old apple trees cannot bear fruits, it is impossible to evaluate their productivity by measuring the fruit yield. In order to find out the optimal irrigation cycle some other biological parameters are measured, such as the tree height, the stem diameter at 5 cm above the ground, leaf area and

the pattern of the root system development. The growth of underground and aboveground parts has been proven to influence the future yield of apple trees.

The two methods are used commonly for evaluating the soil water status. The first one is the gravimetric moisture determination, which is a simple direct method based on drying the soil samples. The drying procedure involves placing the open containers into an electrically heated oven at 105°C until the mass stabilizes at a constant level. In the second method the soil moisture is measured by means of tensiometers, which are the most widely used and least expensive water potential measuring devices.

According to the data obtained for the first year of research, the highest plants were registered in the 1st and the 3rd variants, i.e. in the soil with the maximum water content (Fig. 1). For *Beli Naliv* the average height of trees was 135,8 cm and 140,0 cm, correspondingly, and for *Medunitza* – 138,6 cm and 132,5 cm. The less available moisture content in the soil, the shorter the trees, the minimum values were registered in the control treatment without irrigation while the second variant remains in-between. Such a tendency is typical of both varieties.
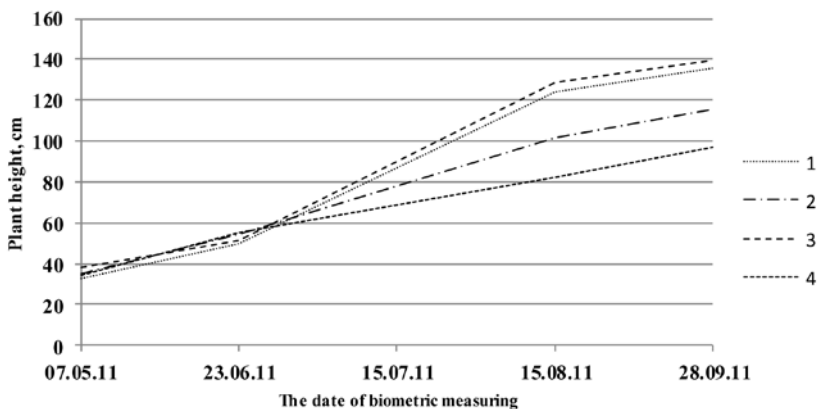

Fig. 1. The growth dynamic of *Beli Naliv* apple trees depending on irrigation treatment. 1 – 70-75% of FC; 2 – 60-65% of FC; 3 – mixed (70-75% of FC); 4 – a control treatment without irrigation.

The maximum shoot increment in all trials was recorded during the period of the most active vegetation growth from later June till the mid-August (Fig. 2). Generally, for both varieties the increase in growth in better moistened variants fluctuates between 81 and 88 cm, which significantly exceeds the level in other treatments. The control treatment without irrigation is characterized by minimum growth of 46-54 cm. Trees grew with nearly the same intensity at other development stages. Such a tendency hae been noticed for both apple

varieties. Moreover, the trees grown under the control treatment experienced growth waves due to irregular precipitations. Trees in this variant started to grow actively when it rained, but the growth retarded duing the drought periods.
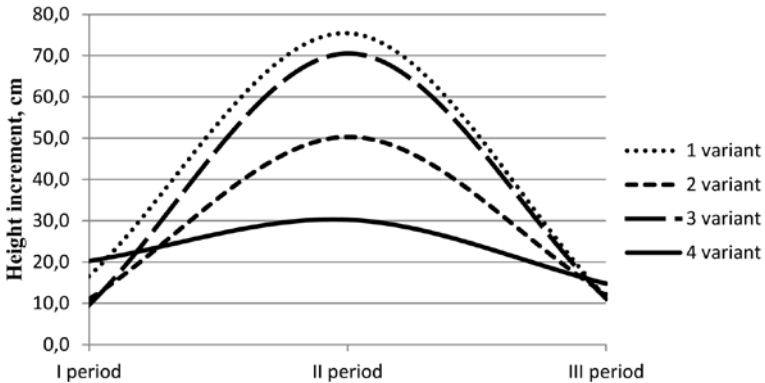

Fig. 2. Height increments of *Beli Naliv* apple trees for various periods during the growing season: I period – from May, 7, to June, 23; II period – from June, 23, to August, 15; III period – from August, 15, to September, 28.

The next measured parameter is the leaf area, which reaches the maximum of 1400-1500 cm^2 under more intensive irrigation (the 1st and the 3rd treatments) and minimum – in the control treatment (800-900 cm^2). It is worth mentioning that the variety "Beli Naliv" is more responsive to the increase in available soil moisture content compared to "Medunitza". In the field experiment, the control treatment is characterized not only by insufficient amount of moisture, but also by its irregular supply. The obtained results correspond well to the literature data and confirm the fact that such soil moisture conditions restrict the growth of leaves and reduce assimilating area of a tree (Соловьева, Кордун, 1968).

Nevertheless, statistical analysis of stem diameters has not revealed any significant differences between the studied treatments. Thus, it is difficult to estimate the influence of irrigation on such a biological feature relying on the results of the first experimental year.

Moreover, there are no significant distinctions in the pattern of the root system development. The majority of roots are concentrated in the horizon of 10-20 cm, and the longest roots reach 38-42 cm in length. However, it should be mentioned that more intensive soil moistening favours better development of small roots, thus increasing the absorbing capacity of the root surface area.

Finally, the obtained experimental data have allowed calculating such a parameter as evapotranspiration, the latter being an important part of the irrigation cycle. As it was expected, the highest evapotranspiration rates were

observed in the 1st and the 3rd variants, when larger amounts of water were supplied, the lowest evapotranspiration was typical of the treatment without irrigation. The maximum daily evapotranspiration of apple trees was registered at the stage of intensive growth (July – August) and coincided with the period of the highest daily temperatures.

On the basis of the obtained data the following conclusions have been made:

1. The evapotranspiration rate varies from 2589 m^3/ha to 3252 m^3/ha depending on the irrigation schedule, and it increases with the growth of irrigation rates. Such a tendency is registered for the values of mean daily evapotranspiration which fluctuate between 18,66 m^3/ha and 22,62 m^3/ha.

2. Moisture deficit in the soil affects severely the development of trees at the stage of their most intensive vegetation growth.

3. Insufficient and irregular soil moistening reduces the leaf surface area of a tree, the size of leaves and the number of leaves per tree. As a result the plants fail to complete their vegetation cycle before frosts and can hardly survive winter.

4. Higher soil moisture content promotes the development of small roots, which leads to the increase in absorbing surface and absorbing capacity of the root system.

5. The biological parameters and evapotranspiration rates obtained during the first year of research have proved that the most favourable wetting conditions are provided in the better moistened variants, when the soil water content is maintained at the level of 70-95% of FC. However, it is necessary to verify that such an irrigation treatment allows trees to complete their vegetation growth in due time in order to prepare properly for the winter period.

REFERENCES

1. *Ахмедов А. Д.* Техника и технология возделывания сельскохозяйственных культур при капельном и внутрипочвенном орошении / А. Д. Ахмедов, Е. А. Ходяков, Е. П. Боровой, М. В. Мазепа. Волгоград : ИПК ФГОУ ВПО ВГСХА «Нива», 2008. 228 с.
2. *Иволгин В. С.* Оптимизация по критериям ресурсосбережения производственных процессов в плодово-ягодных питомниках : автореф. дис. … канд. техн. наук. М., 2002. 19 с.
3. *Нестерова Т. С.* Капельное орошение / И. С. Зонн, Е. А. Вейцман. М.: ВНИИТЭ-ИСХ, 1973. 63 с.
4. *Сабиров М. К., Раззаков М. Д.* Влияние капельного орошения на рост и урожайность садов (обзор). Научно-исследовательский институт научно-технической информации и технико-экономических исследований Госплана УзССР. Ташкент, 1990. 24 с.
5. *Синалаев А. Н.* Оптимальная организация процессов производства и реализации саженцев в плодово-ягодных питомниках : автореф. дис. … канд. экон. наук. М., 2002. 16 с.

6. *Соловьева М. А., Кордун В. П.* Влияние влажности почвы на ростовые процессы, структурные изменения и оводненность тканей у яблони // Водный режим растений и их продуктивность / Под ред. д-ра биол. наук Н. С. Петинов. М.: Наука, 1968. С. 227–236.

7. *Шугай П. Ю.* Режим капельного орошения школки плодовых культур при повышенных температурах окружающей среды : дис. … канд. техн. наук. Краснодар, 2005. 205 с.

8. *Waterman P., Hogue E. J., Quamme H.* 1993. Tree fruit home nurseries. Published by Okanagan Valley Tree Fruit Authority. 47 p. URL: http://www.al.gov.bc.ca/treefrt/ product/Tree_Fruit_Home_Nurseries.pdf.

SALTING-IN PHENOMENON FOR THE QUATERNARY SYSTEM WATER – PYRIDINE – BUTYRIC ACID – POTASSIUM IODIDE

Z. V. Chepurina, D. G. Cherkasov

Saratov State University

Currently in the technological practice so-called nonconventional extraction systems are increasingly being used that do not contain highly volatile and flammable organic solvents. One reason for the segregation of these systems is the chemical interaction between the components of the aqueous solution, leading to the formation of compounds in the liquid phase with limited solubility in water and the appearance of a closed bimodal curve (Мерцлин, 1936). Introduction of salting-in or salting-out agents in such systems can either expand or reduce its size up to complete homogenization of the system. It should be noted that the impact of the fourth component (salting-in or salting-out agent) on the phase behavior of systems and topological transformation of its phase diagram with the temperature remains quite unexplored.

The aim of the investigation was to determine the solubility by means of the visual-polythermal method and at locating the critical points with the aid of phase-volume ratios in component mixtures on nine sections in cut of triangle of the quaternary system water – pyridine – butyric acid – potassium iodide.

The used substances were purified and identified. Water was obtained in redistillator DEM-20 "MERA-POLNA". Pyridine was drained over potassium hydroxide during a week, then decantation was used to separate from the residue. It was drawn over on the fur-tree deflegmator 0.3 m height and the fraction boiling in the range of temperatures 115–116°C was selected. Butyric acid was drained over magnium sulfate during a week with periodic stirring, then decantation was used to separate from the residue. It was drawn over on the fur-tree deflegmator 0.2 m height and the fraction boiling in the range of temperatures 164–165°C was selected. Potassium iodide was thin pounded in an agate mortar and dried in vacuum over oxide phosphorus (V) at 120°C to constant weight. The absence of moisture in salt was supervised the thermo-

gravimetric analysis. The prepared substances were stored over calcinate calcium chloride in exicators with protection against sun rays.

Mixtures of components of a cut were characterized by the constant maintenance of salt (2.50 wt. %). Phase equilibria and critical phenomena were studied by means of the visual-polythermal method in component mixtures on nine sections of the concentration triangle of the cut (Аносов, Озерова, Фиалков, 1976). The four-component mixtures on I-VII sections were characterized by the variable content of pyridine and by the constant content of butyric acid and water for every section: 21.00:79.00(I), 28.00:72.00(II), 29.00:71.00(III), 31.00:69.00(IV), 36.00:64.00(V), 44.00:56.00(VI), 53.00:47.00(VII). The four-component mixtures on VIII и IX sections were characterized by the variable content of water and by the constant content of butyric acid and pyridine for every section: 28.00:72.00(VIII), 40.00:60.00(IX). Schematic position of sections of two types on a cut triangle is shown on fig. 1. The component solubility polytherms appear as parabolas in all sections.
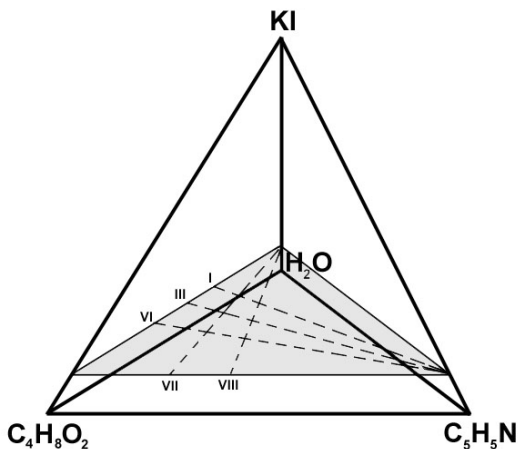

Fig. 1. Schematic position of the cut and sections (I, III, VI, VII, VIII) on the plane of the cut of composition tetrahedron of water – pyridine – butyric acid – potassium iodide system.

Having located the maxima on the polytherms, we plotted the maximum temperatures of two-liquid phase state existence against the content of pyridine and butyric acid in component mixtures (Fig. 2). The coordinates of the maxima of these curves correspond to the maximum temperature of two-liquid phase state existence in the given system (44.8°C) with a mixture composition: 2.50 wt. % KI, 57.40 wt. % H_2O, 16.66 wt. % C_5H_5N and 23.44 wt. % $C_4H_8O_2$.

Similarly, the dependence on temperature of the mentioned components maintenance at the critical solubility points was plotted, which showed a maximum at 43.0°C while the composition was 2.50 wt. % KI, 49.77 wt. % H_2O, 19.09 wt. % C_5H_5N, 28.64 wt. % $C_4H_8O_2$ (Fig. 3).
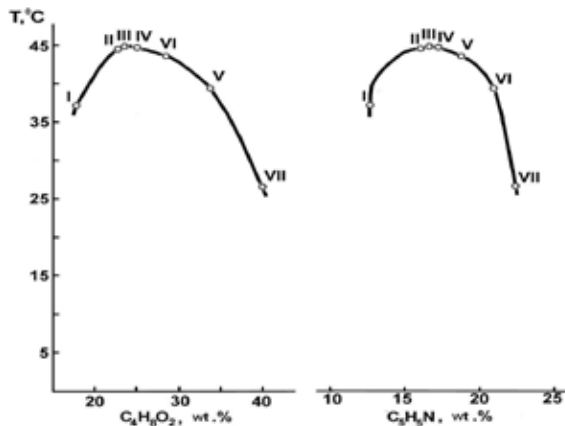

Fig. 2. The dependence of maximum temperatures of two-liquid phase state on the content of pyridine and butyric acid in component mixtures in the cut of the quaternary water – pyridine – butyric acid – potassium iodide system.
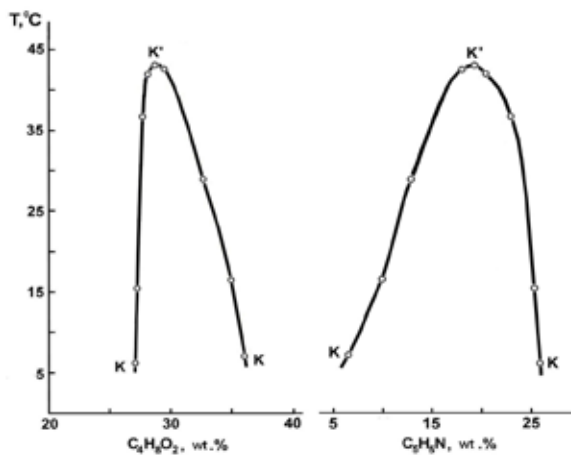

Fig. 3. The dependence of components maintenance at the critical solubility points on temperature in the cut of the quaternary water – pyridine – butyric acid – potassium iodide system.

Results of polythermal researches were used to construct isotherms of solubility on the cut triangle of the quaternary system at temperatures: 5.0, 20.0, 40.0 and 44.00°C (Fig. 4).
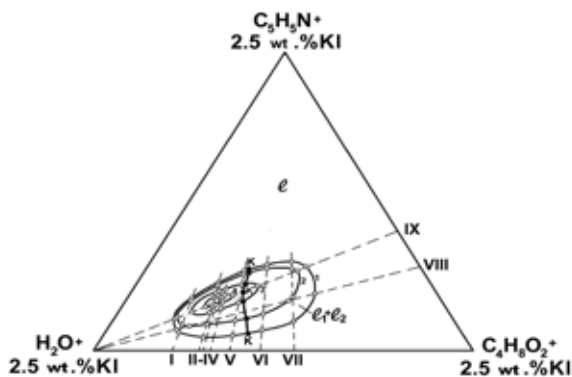

Fig. 4. Phase state isotherms (wt %) on the cut triangle of the quaternary water – pyridine – butyric acid – potassium iodide system at temperatures (°C): *1*–5.0, *2* – 20.0, *3* – 40.0, *4*–44.0.

There is a closed binodal curve on the solubility isotherms in phase diagram on the cut which bounds the two-liquid phase state region and contains two critical points besides 44.0°C. The area of the delamination at more high temperature is located inside the region of the delamination at lower temperature. As temperature increases, the area of the delamination region diminishes and this region shrinks to a non-critical point at 44.8°C. The maximum temperature of two-liquid phase state existence in the given system (44.8°C) appears below similar maximum temperature (52.0°C) in the system water – pyridine – butyric acid (Cherkasov, Smotrov, Ilin, 2008). Introduction of potassium iodide in mixtures liquid system increase component solubility and possesses salting-in action in water-organic solutions.

REFERENCES:

1. *Аносов В. Л., Озерова М. Н., Фиалков Ю. Я.* Основы физико-химического анализа. М.: Наука, 1976. 504 с.
2. *Мерцлин Р. В.* О системах с верхней тройной критической точкой // Журн. общ. химии. 1936. Т. 6. № 12. С. 1828–1840.
3. *Cherkasov D. G., Smotrov M. P., Ilin K. K.* // Russian Journal of Applied. 2008. Vol. 81, № 2. P. 229–233.

THE MEASUREMENT OF THE OUTGOING SHORT-WAVE RADIATION (OSR) FROM SATELLITE "METEOR-M" № 1

M. Y. Chervyakov, Y. A. Sklyarov

Saratov State University

A new "Meteor" satellite program has been started in Russia. The first satellite of new generation "Meteor-M" № 1 was put into orbit on September 16, 2009. The equipment IKOR – "The Measuring instrument of short-wave reflected radiation", created in Saratov State University under the direction of Yu. A. Sklyarov was installed on this satellite. Radiometer IKOR is intended for satellite monitoring of the outgoing reflected short-wave radiation, which is one of the components of Earth radiation balance, and albedo of the Earth-atmosphere system. Such information can be used in different models of long-term weather forecasts, in researches of climate change trends and also in calculation of absorbed solar radiation values. The received data from satellite "Meteor-M" № 1 are gathered in Research Centre for Earth Operative Monitoring, Moscow.

The satellite "Meteor-M" № 1 has been launched into heliosynchronous orbit with the following parameters: the inclination to an equator plane i is 98,786 °, the average height over the Earth surface is 832 km, the orbiting time is 101,307 minutes, the angular distance ω on the equator between the descending knot of the orbit and the circle of declination of the Sun is approximately 27,3°, speed of movement of the satellite on the orbit is ≈7 km/s. The equator crossing time on the sunny side in the descending knot is about 9 hours, in ascending one – about 21 hours of local solar time. The repetition period of geometrical conditions of observation from the satellite "Meteor-M" № 1 is 4, 67 days. Due to the angular diameter of the IKOR's field of view for the satellite "Meteor-M" № 1 (in geocentric coordinates it is 8,8°) and the angular speed 3,55 degree/minute, the satellite passes the field of view for 2,5 minutes. As the rate of records is 1/s, it takes for the full field of view 148 counts. The period of the same orbit repetitions is carried out in 14 days that corresponds to 199 orbits. During its work the satellite has already made more than 12 thousand orbits (February 2012).

For measurement processing there have been created the programs, allowing carrying out decoding of raw measurements in the orbit, their binding to the telemetering information (definition of the moment of local time and geographical coordinates of measured sites).

The following stage of processing is calculation of daily averaged quantities of the measured values and then evaluation of monthly averaged values of outgoing short-wave radiation (OSR), albedo and absorbed solar radiation (ASR). Daily averaged and monthly averaged values are climatologically significant. The special attention is given to calculation of absorbed solar radia-

tion since it is a driving force of the processes occurring in the atmosphere, in the ocean and on the Earth's surface.

Further programs of absorbed solar radiation processing have been developed, allowing quantitatively estimating values of radiation incoming on any chosen sites of the terrestrial surface, comparing ASR between them (Fig. 1).
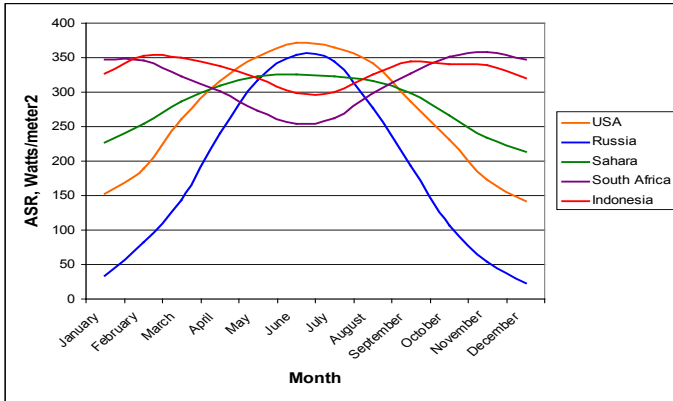

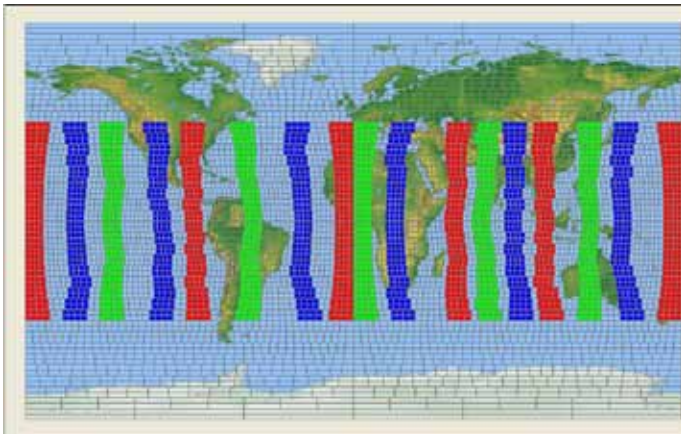Fig. 1. Annual variation of absorbed solar radiation (ASR) on the equal areas (2010)

Fig. 2. Meridional cross-sections

Distributions of absorbed solar radiation in meridional direction have been estimated that allows defining latitudinal distributions of absorbed radiation in any strips of the surface. For example distributions of absorbed solar radiation with 10º width on a longitude in directions to the north and the south

from the equator (Fig. 2) have been separately estimated. It allows to compare intensity of absorbed solar radiation transfer from tropical latitudes where this energy is maximum to high northern and southern latitudes, and to solve many other problems. For instance, (Fig. 3) the latitudinal distribution of absorbed solar radiation is given for some months of the year 2010.
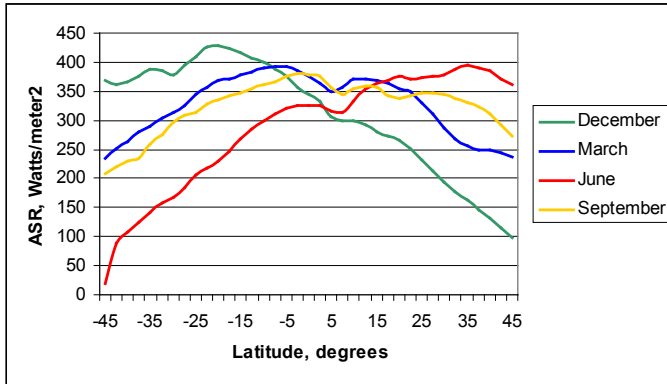

Fig. 3. Latitudinal distribution of absorbed solar radiation for some months of the year 2010 in Atlantic region
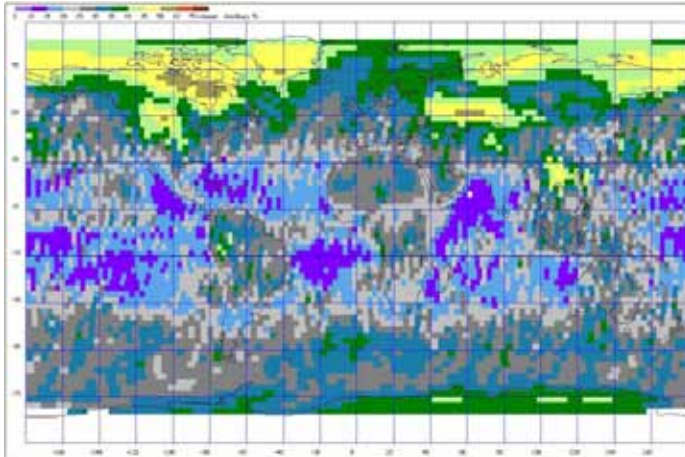

Fig. 4. The map of global distribution of monthly averaged values of albedo (May 2011)

Satellite "Meteor-M" № 1 is heliosynchronous that allows observing from North to South poles. The basic products of data processing are given in the form of global maps of distribution OSR, albedo and absorbed solar radia-

tion. Such maps were made for each month during observation period. Fig. 4 presents the map of global distribution of monthly averaged values of albedo.

Calculation of monthly averaged quantities of the selected values gives the opportunity to estimate also their variations in time, i.e. intrayear and interannual. Value of interannual variations will be defined by operational time of the satellite and the radiometer.

The authors are indebted to A. A. Sosnovskaya for the help in translation of the text.

REFERENCES

1. *Скляров Ю. А., Бричков Ю. И., Семёнова Н. В.* Радиационный баланс Земли. Введение в проблему. Саратов : Изд-во СГУ, 2009. 185 с.
2. *Скляров Ю. А., Фейгин В. М., Воробьёв В. А., Котума А. И., Семёнова Н. В., Червяков М. Ю.* Первые результаты обработки со спутника «Метеор-М» № 1 // Погода и климат: новые методы и технологии исследований : сб. науч. тр. / под ред. Калинина Н. А. Пермь : Изд-во Перм. гос. ун-та, 2010. С. 52–56.
3. *Скляров Ю. А., Воробьев В. А., Котума А. И., Семенова Н. В., Фомина Н. В., Червяков М. Ю., Фейгин В. М.* Уходящая коротковолновая радиация и альбедо на верхней границе атмосферы по наблюдениям с ИСЗ «Метеор-М» № 1 : материалы VIII Всерос. конф. «Современные проблемы дистанционного зондирования Земли из космоса». М. : ИКИ РАН, 2010. С. 53–54.

ON-OFF INTERMITTENCY OF THALAMO-CORTICAL OSCILLATIONS IN THE ELECTROENCEPHALOGRAM OF RAT WITH GENETIC PREDISPOSITION TO ABSENSE EPILEPSY

V. V. Grubov

Saratov State University

Introduction

Radiophysics and electronics designed numerous methods for analysis of complex oscillatory processes. Nowadays these methods find a use in different spheres of science, even in physiology and medicine. Radiophysical methods seem to be very useful in analysis of dynamics of neural network. Such network is a complex object consisting of great number of individual oscillatory elements – neurons.

A usual way to obtain information about brain activity is to record an electroencephalogram (EEG). EEG is an averaged sum of electric currents generated by a small group of neurons. Traditionally, one can mark out few frequency ranges on EEG (alpha, beta, etc.) It is well known that there is a clear correlation between the activity in specific frequency range on EEG and the functional state of organism. So, one of the most important objects in brain

activity research is to study some forms of rhythmic activity and regularity of their appearance.

Sleep spindles are among the most numerous spontaneous oscillations that are abundantly present on EEG of humans and animals during non-REM sleep (*De Gennaro and Ferrara, 2003*). Sleep spindles can be recorded in cortical surface and thalamus as brief episodes of 9–14 Hz oscillation with specific spindle-like form. Basic electrophysiological studies show that sleep spindles are initiated by reticular thalamic nuclei and spread throughout thalamus to cortex. Thalamo-cortical neural network, which normally produces sleep spindles, under certain conditions could give rise to epileptic spike-wave discharges (SWD) (*Steriade et al., 1993; Kostopoulos, 2000*).

It is well known that sleep spindles and spontaneous SWD are characterized by similar temporal distribution across sleep-waking cycle. In particular, both EEG events are predominant in drowsy state and in transition from wakefulness to sleep. Relationship between SWD, sleep spindles and mechanisms of sleep is very complicated and it is not well understood. In particular, in Genetic Rats with Absence Epilepsy (GAERS), SWDs develop from wake-related 5–9 Hz oscillations, which are distinct from spindle oscillations (7–15 Hz) (*Pinault et al., 2006*). 5–9 Hz oscillations originate from the cortex (*Pinault et al., 2006*), in opposite to sleep spindles, whose pacemaker is known to be located in the thalamus (*Steriade et al., 1993*). Spontaneous medium-voltage 5–9-Hz oscillations usually present in EEG during awake immobility, but they do not always lead to spike-and-wave discharges (*Pinault et al., 2001*). In addition to that, 5–9 Hz oscillations can be recorded in non-epileptic rats and never give rise to SWD (*Pinault et al., 2001*). Despite considerable progress in attempts to explain the cellular mechanisms of 5–9 Hz oscillations, temporal dynamics of these oscillations have not been investigated so far.

The current paper examines three kinds of thalamocortical oscillatory patterns: SWD, sleep spindles and 5–9 Hz oscillations, in respect to their intrinsic time–frequency structure and global dynamics.

Materials and methods

EEGs were recorded in six male WAG/Rij rats. A recording electrode was implanted epidurally over the frontal cortex for the reason that SWD and spindles showed their amplitude maximum in this zone. Ground and reference electrodes were placed over the two symmetrical sides of the cerebellum. EEG recordings were made in freely moving rats continuously during a period of 24 h. EEG signals were fed into a multi-channel differential amplifier via a swivel contact, band-pass filtered between 0.5 and 100 Hz, digitized with 1024 samples/s/per channel.

Diagnostic method describing in this paper uses continuous wavelet transform (CWT). CWT means the convolution of EEG signal $x(t)$ with basic wavelet function $\varphi_{s,\tau}(t)$.

$$W(s,\tau) = \int_{-\infty}^{+\infty} x(t)\varphi_{s,\tau}^*(t)\,dt$$

$$\varphi_{s,\tau}(t) = \frac{1}{\sqrt{s}}\varphi_0\left(\frac{t-\tau}{s}\right)$$

where s is time scale and τ is time shift of wavelet function.
Complex Morlet wavelet was used as basic function

$$\varphi(\eta) = \frac{1}{\sqrt[4]{\pi}}\,e^{i\omega_0\eta}\,e^{\frac{\eta^2}{2}}$$

where ω_0 is an empirically defined parameter. In present study $\omega_0 = 2\pi$.

Distribution of wavelet energy over the time scale was visually inspected in order to determine the most characteristic frequency bands F_s that would explicitly characterize SWD, sleep spindles and 5–9 Hz oscillations. These characteristic frequency bands were determined, and integration was performed over each of the selected bands.

$$\omega(t) = \int_{F_s}\left|W(s,t)\right|ds$$

Wavelet power $\omega(t)$ in specific frequency bands F_s was computed and used in automatic detection system as criteria for selective identification and localization of the investigated EEG patterns.

Automatic detection system employed specific wavelet-based algorithm described earlier (*Ovchinnikov et al., 2010*). This method based on calculation of wavelet energy $\omega(t)$ in the predetermined frequency bands F_s for SWD, sleep spindles and 5–9 Hz oscillations. The value $\omega(t)$ was then compared with the threshold value ω_c and presence of oscillatory pattern was recognized under condition (t) > ω_c. This method provided specific discrimination of SWD in background EEG by an increase of cumulative wavelet power in two frequency bands $F \in$ [8, 14] and [30, 50] Hz. The accuracy of detections was 95–98% in all animals.

Sleep spindles in the EEG showed an increased wavelet power in the frequency range of 10–15 Hz. This feature was necessary, but not sufficient for selection of sleep spindles in EEG. Being selected in 10–15 Hz frequency band, sleep spindles were often mixed up with SWD. In order to prevent error spindle detections, EEG segments with previously detected SWD were set to zero (*Sitnikova et al., 2009*).

Selective detection of sleep spindles and 5–9 Hz oscillations in EEG was based on measurements of wavelet energy in two frequency bands $F_{s1} \in$ [5–9] Hz and $F_{s2} \in$ [10–15] Hz. Threshold levels ω_{1c} and ω_{2c} were chosen empirically for $\omega_1(t)$ and $\omega_2(t)$ correspondingly to provide the most accurate localization of sleep spindles in time domain. The presence of a sleep spindle was detected if wavelet power in the frequency range of 10–15 Hz, $\omega_2(t)$, exceeded the threshold ω_{2c} and $\omega_2(t)$ was greater than wavelet power in 5–9 Hz, $\omega_1(t)$:

$$\omega_2(t) > \omega_{2c} \qquad \omega_2(t) > \omega_1(t)$$

5–9 Hz oscillations were identified based on the following condition:

$$\omega_1(t) > \omega_{1c} \qquad \omega_2(t) < \omega_1(t)$$

i.e., wavelet power in 5–9 Hz, $\omega_1(t)$, exceeded the threshold ω_{1c} and $\omega_2(t)$ was smaller than wavelet power in 5–9 Hz.

Presence of rhythmic alpha/theta components in EEG, that were neither associated with sleep spindles nor with 5–9 Hz oscillations, is a difficulty encountered in performing automatic selection. These rhythmic components corresponded to short-term increase of instantaneous wavelet energy in the frequency bands F_{s1} and F_{s2} and sometimes caused false detections. In order to prevent incorrect detections, instantaneous wavelet energy $\omega(t)$ was averaged across time window T = 0.5 s.

$$\langle \omega(t) \rangle = \frac{1}{T} \int_T \omega(t)\, dt$$

The averaged wavelet energy $\langle \omega(t) \rangle$ was substituted for $\omega(t)$ and this improved quality of automatic detection.

Results

Time–frequency characteristics of the investigated phenomena were studied in frontal EEG recordings using CWT. This analysis was aimed to define the spectral features that would explicitly characterize each class of the investigated EEG patterns; these features were also used as selection criteria in the automatic detection system.

Criteria for assessing sleep spindles in EEG were derived from animal EEG research (*Steriade et al., 1993*). In WAG/Rij rats, sleep spindles represented a sequence of 8–14 Hz waves, they were characterized by twofold increase in amplitude as compared to EEG background, had waxing–waning morphology and minimal duration of 0.5 s. According to Morlet-based wavelet analysis, sleep spindles in WAG/Rij rats showed a marked increase wavelet power in 10–15 Hz (Fig. 1, *a, c*). Wavelet spectrum of sleep spindles was often contaminated with additional low-frequency components (Fig. 1) and high-frequency bursts (occasional spikes). There were substantial frequency fluctuations within one spindle train (i.e., intraspindle frequency variation) and mean frequency of different sleep spindles also varied (i.e., between-spindle frequency variations). The averaged frequency of sleep spindle per rat varied from 12.1 Hz to 14.1.

5–9 Hz oscillations (Fig. 1, *b, d*) characterized by spindlelike waveform. Frequency of these oscillations was lower than that in sleep spindles, and matched the frequency of epileptic spike-wave discharges (i.e., 7–9 Hz).

SWD appeared in EEG as a sequence of repetitive highvoltage negative spikes and negative waves (Fig. 2). The envelope of SWD was rectangular due to the presence of large spike components with approximately the same amplitude, and this waveform differed from the waxing–winning waveform of

sleep spindles (Fig. 1). In addition to that, SWD had a longer duration (several seconds) then sleep spindles (0.5–2 s). Wavelet spectrum of SWD usually displayed two dominant frequency components (Fig. 2): mean frequency ~8–9 Hz and its harmonics in 16–18 Hz. Sharp spike components of SWD can be recognized in wavelet spectrum as high-frequency bursts (above 20 Hz).
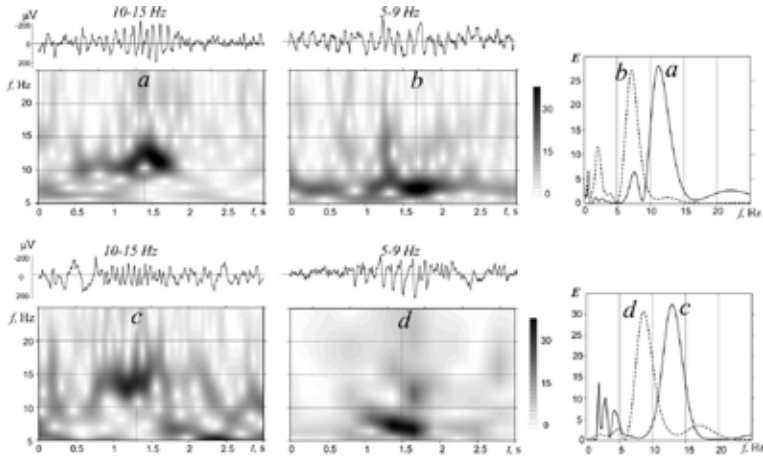

Fig. 1. EEG examples of sleep spindles (10–15 Hz) and 5–9 Hz oscillations and corresponding Morlet-based wavelet spectra. Right plates show distribution of instantaneous wavelet energy E (fs) as measured in sleep spindles (a, c, solid lines) and in 5–9 Hz oscillations (b, d, dotted lines), indicating that peak frequencies of these phenomena lie in two clearly distinctive frequency bands.
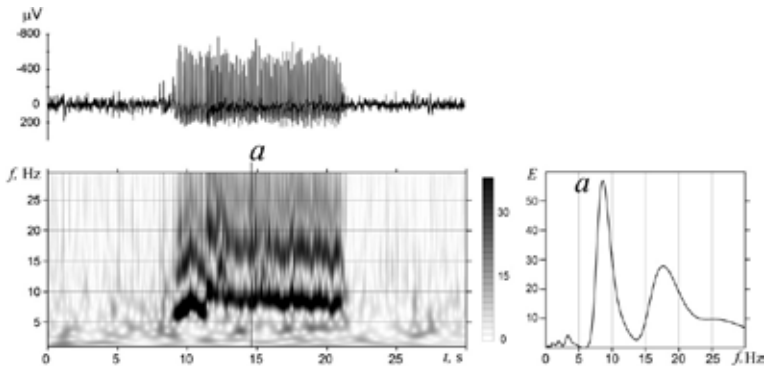

Fig. 2. Typical SWD as recorded in the frontal EEG, its Morlet-based wavelet spectrum and distribution of instantaneous wavelet energy as measured at the time point 'a'. Note the two prominent peaks in instantaneous energy distribution: the first largest peak in the fundamental frequency ~8–9 Hz and the second peak in harmonic range ~16–18 Hz.

SWD, sleep spindles and 5–9 Hz oscillations were automatically detected in EEG using wavelet-based algorithm. Table 1 shows the number of the investigated EEG events and their mean duration.

Basic characteristics of investigating patterns

Rat ID	Sleep spindles		5–9 Hz oscillations		SWD	
	N	Mean duration, s	N	Mean duration, s	N	Mean duration, s
1	3312	0.8	1378	0.73	276	5.55
2	5440	0.58	869	0.84	282	7.63
3	2776	0.69	974	0.85	396	7.63
4	2007	0.7	1096	0.76	296	3.73
5	3145	0.66	1511	0.86	131	3.76
6	4421	0.64	1827	0.81	462	7.16
Mean	3517±1227	0.68±0.07	1276±363	0.81±0.05	307±114	5.91±1.84

N – number of episodes as scored in 24 h EEG recordings

Temporal dynamics of the investigated oscillatory patterns were examined based on statistical analysis of time intervals between consequent EEG events. These intervals, L, corresponded to the off-phase of intermittent behavior. This analysis was performed separately for SWD, sleep spindles and 5–9 Hz oscillations. The dependence of the number of off-phases $N(L)$ on their duration L was tested for power-law

$$N(L) = \beta L^{\alpha}$$

where α is an exponent, and β is a normalization factor. The value of α in power-law distribution is very important, since $\alpha = -3/2$ was proven to hold for a system with on–off intermittency (*Hramov et al., 2006*). In each individual rat the 'α' was defined by minimizing the root-mean square error ε of empirically calculated distributions with different bind widths ΔL.

Distributions of both between-SWD and between-spindle intervals were close to the straight line in log–log scale in all experimental animals (Fig. 3, A, B), corresponding to the power-law with the exponent −3/2

$$N(L) = L^{-3/2}$$

This type of distribution is known to be a key feature of on–off intermittency (*Hramov et al., 2006*). The same analysis of 5–9 Hz oscillations showed that distributions of between-oscillation intervals displayed a good approximation to the power law with the exponent −1 and were close to the straight line in log–log scale (Fig. 3C)

$$N(L) = L^{-1}$$

This kind of dynamics was rather uncertain, and it obviously differed from the on–off intermittent behavior of sleep spindles and SWD.

Although the number of SWD and sleep spindles varied from rat to rat, these EEG events were distributed in time in accordance to the power law with the exponent −3/2. It is important that on–off intermittent behavior was found in both SWD and sleep spindles, despite the fact that these EEG events were also differed in respect to their time–frequency profiles (Fig. 1).
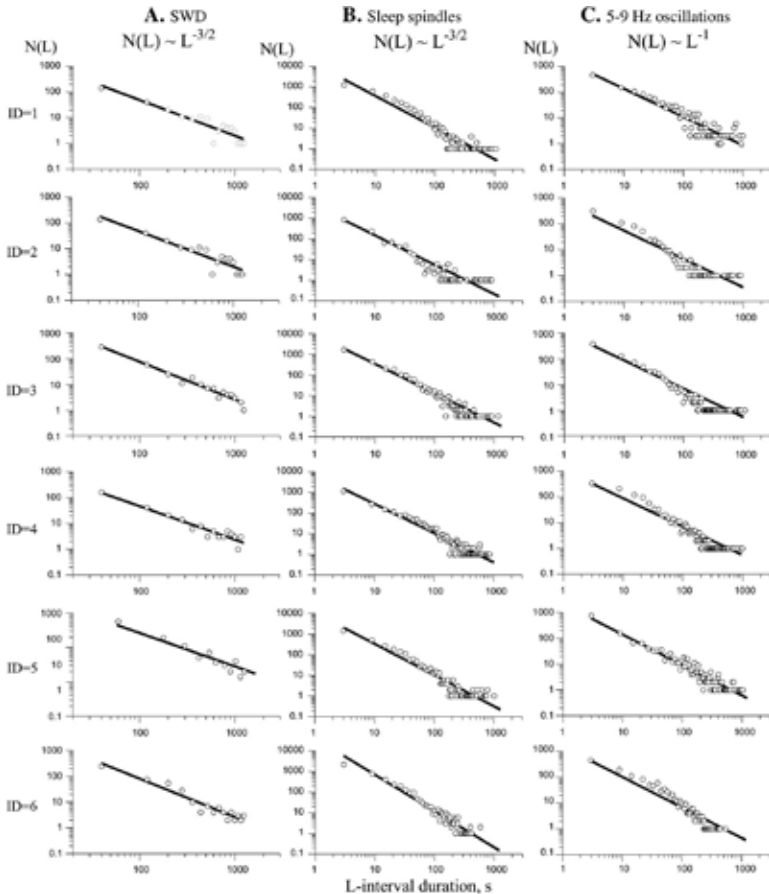

Fig. 5. Statistical distribution of time periods between the investigated EEG events (*L* intervals) plotted in log–log scale. *A, B.* In sleep spindles and in SWD, distributions of *L*-intervals are best approximated to the power law with the exponent −3/2 in all individuals (ID = 1–6). This is typical for on–off intermittency. *C.* In 5–9 Hz oscillations, distribution of between-spindle intervals fits the power law with the exponent −1.

Conclusion

The present paper demonstrates that (1) distribution of spindles, 5–9 Hz oscillations and spike-wave paroxysms in EEG are not random, and that (2) temporal dynamics sleep spindles and SWD, but not 5–9 Hz oscillations, can be defined as on–off intermittency. The term intermittency refers to a wide variety of alternations in behavior, in which almost periodic (oscillatory) behavior is interrupted by sudden chaotic bursts.

REFERENCES

1. *De Gennaro L., Ferrara M.* Sleep spindles : an overview / Sleep Med. 2003. Rev. 7, P. 423–440.
2. *Hramov A. E., Koronovskii A. A., Kurovskaya M. K., Boccaletti S.* Ring intermittency in coupled chaotic oscillators at the boundary of phase synchronization / Phys. Rev. 2006. Lett. 15 (97(11)), P. 114101.
3. *Kostopoulos G. K.* Spike-and-wave discharges of absence seizures as a transformation of sleep spindles : the continuing development of a hypothesis / Clin. Neurophysiol. 2000. Suppl. 2, S27–S38.
4. *Pinault D., Vergnes M., Marescaux C.* Medium-voltage 5–9 Hz oscillations give rise to spike-and-wave discharges in a genetic model of absence epilepsy : in vivo dual extracellular recording of thalamic relay and reticular neurons / Neurosci. 2001. 105, P. 181–201.
5. *Pinault D., O'Brien T. J.* Cellular and network mechanisms of genetically-determined absence seizures / Thalamus Relat Syst. 2005. 3 (3), 181–203.
6. *Ovchinnikov A. A., Luttjohann A., Hramov A. E., Van Luijtelaar G.* An algorithm for real-time detection of spike-wave discharges in rodents / J. Neurosci. Methods. 2010. 194, P. 172–178.
7. *Sitnikova E., Hramov A. E., Koronovskii A. A., Van Luijtelaar G.* Sleep spindles and spike-wave discharges in EEG : their generic features, similarities and distinctions disclosed with Fourier transform and continuous wavelet analysis / J. Neurosci. Methods. 2009. 180, P. 304–316.
8. *Steriade M., McCormick D. A., Sejnowski T. J.* Thalamocortical oscillation in the sleeping and aroused brain / Science. 1993. 262, P. 679–685.

POROUS STRUCTURE OF SEPARATION MATERIAL INVESTIGATION WITH POROMETRIC METHODS

T. S. Denisova, A. I. Pantyuhina

Saratov State University

Separator (system fixation electrolyte) is a key component in the sealed lead-acid battery, as it provides its adjustable valve operation. The properties of the separator depends on efficient transfer of gas through the interelectrode gap and, consequently, its ionization at the opposite electrode. Management of gas-liquid

flow through the separator must be provided with coincidence of porous structure of the separator and electrode pores which enables the process of ionization (1).

The aim of the investigation is to determine porous structure separation materials produced by BERNARD DUMAS (France) and Hollingswoth Vose (USA).

Structural characteristics of the investigated separation material were studied by the contact standard porosimetry (CSP) in the evaporation and adsorption isotherms removal. We used CSP removal method to build the structural curve. This method applies the standards with known structural integral curve. Adsorption isotherms were obtained on high-speed analyzer, gas sorption Quantachrome NOVA, combined with a personal computer with special software. As absorbate used nitrogen. To determine the pore size distribution Barrett-Joyner-Halenda (BJH) method was used. The surface morphology of separation materials was investigated using a scanning electron microscopy MIRA 2 LMU, equipped with energy dispersive microanalysis system INCA Energy.

From the adsorption isotherms obtained by the method of BJH, the samples were constructed for the differential and integral distribution curves of pore depending on their radii, which are presented in Fig. 1 (a) and 2 (a). A differential and integral distribution curves of pore radii for the same separators are shown in Fig. 1 (b) and 2 (b). These results were obtained by CSP method.

The values of specific surface area, porosity, calculated by CSP method, are presented in Table 1.

Table 1

The values of specific surface area, porosity, calculated by CSP method

Sample	Average pore radius, μm	Porosity over weight, cm³·g-1	Porosity over volume, cm³·cm³	Meso- and macro-pore surface, m²·g⁻¹	Total pore surface, m²·g⁻¹
BERNARD DUMAS	9.74	6.36	0.94	5.72	5.78
Hollingswoth and Vose	6.25	6.28	0.94	5.26	5.26

From these results it is evidant that the samples are highly porous separator systems. Their total porosity is 95%.

CSP method and BJH method can determine pore distribution radii. The data are presented in Table 2.

Table 2

Pore volume distribution by pore radius, %

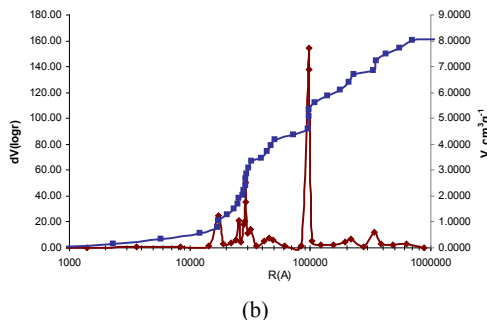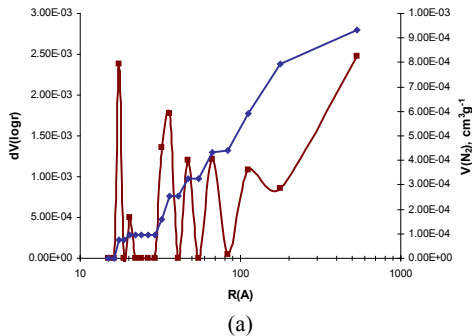| Sample	Pore radius, μm				
	0.001-1	1-5	5-10	10-50	50-100
	Относительный объем пор, %				
BERNARD DUMAS	4.38	44.67	17.38	26.53	7.02
Hollingswoth and Vose	5.88	61.75	13.07	16.37	2.95

(a)

(b)

Fig. 1. Differential and Integral curves distribution of pore volumes to radii obtained by BJH method (a) and CSP method (b) for the separator produced by BER-NARD DUMAS France.

Table 2 shows that the proportion of pores with a radius of less than 1 μm in the test sites is small. The bulk of pores are placed within the range of 1-5 μm. The relative volume of pores which falls on this range is 61.75% for a separator produced by Hollingswoth and Vose, and 44.67% for the separation material produced by BERNARD DUMAS. Hollingswoth and Vose separation material is a finely porous. Reducing the size of pores leads to an increase in specific surface area of the separation of the material. Brunauera - Emmett - Teller (BET) has determined that the specific surface area of separators produced by Hollingswoth and Vose company is 2.0 $m^2·g^{-1}$, and for the separation material produced by company BERNARD DUMAS, this value is 0.61 $m^2·g^{-1}$. In the study of separation materials there is also a sufficient number of pores with a radius ranging from 5 to 10 microns and from 10 to 50 microns. The porous structure of the investigated separation material is consistent with a pore size of the negative electrode of lead-acid batteries (LAB) (2). This allows to expect effective absorption of oxygen and hydrogen on the working electrode at a charge of LAB.

Fig. 3 shows the micrographs of the samples. Materials are characterized by a combination of fibers with different diameters ranging from 0.3 to 2.5μm that enables creation of a porous structure.
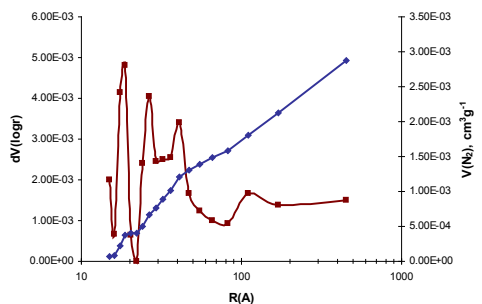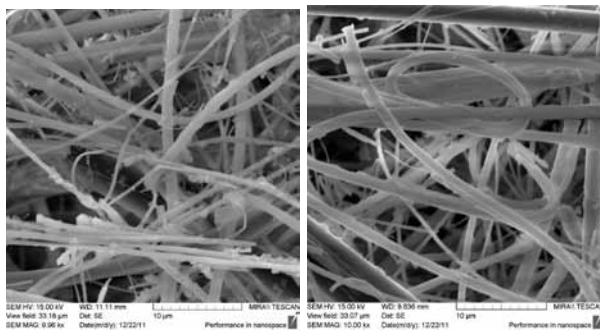

(a)
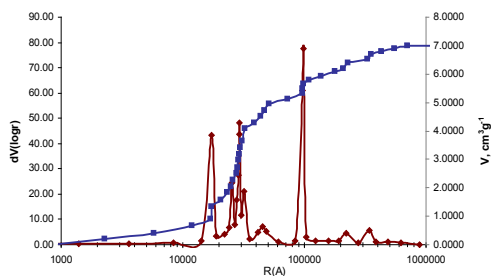
(b)

Fig. 2. Differential and Integral curves distribution of pore volumes to radii obtained by BJH method (a) and CSP method (b) for the separator produced by Hollingswoth and Vose USA.

(a) (b)

Fig. 3. Electron microscopy of the surface of the separation of materials: BERNARD DUMAS (a), Hollingswoth and Vose (b)

REFERENCES

1. *Хомская Е. А., Казаринов И. А., Семыкин А. В., Горбачева Н. Ф.*, 2008.
2. *Кадникова Н. В., Бурашникова М. М., Зотова И. В., Шишова М. А., Луцкова Т. А., Казаринов И. А.*, 2009.

GEOINFORMATION MODELING IN SOLVING PROBLEMS
OF SUSTAINABLE DEVELOPMENT OF MUNICIPAL DISTRICTS

D. P. Khvorostukhin, A. V. Molochko

Saratov State University

In the modern world, great attention is paid to problems of rational land utilization and environmental care. These issues are common to the whole mankind – even the local adverse effects will certainly give a response in other parts of the world.

Realizing this, in 1972 in Stockholm, The United Nations held a conference on the Human Environment. Continuing and developing its position in many ways after 20 years in Rio de Janeiro the UN Conference on Environment and Development was held. Its result was two well-known documents:

• Rio de Janeiro Declaration on Environment and Development;

• An Agenda into the 21st Century (Доклад конференции ООН, 1992).

The main message of these documents is the idea of necessity of human civilization development by such means to avoid harm to future generations. This development has been called «sustainable development».

At the present moment, most countries have adopted concepts of sustainable development of their territories. The Russian Federation is no exception. In 1996 the Presidential Decree 440 of April 1, 1996 «About the Concept of Russian Federation`s transition to sustainable development» was signed.

Since then, a variety of documents, governed developments of proper areas were developed in our country. Urban Development Code, adopted in 2004, relates to these documents.

According the Urban Development Code, sustainable development of territories ensure the implementation of urban planning security and favorable conditions of human life, limiting the negative impact of economic and other activities on the environment and ensure the protection and rational use of natural resources for present and future generations (Градостроительный кодекс РФ, 2009). The basis for ensuring such development is territorial planning.

Nowadays, the country system of territorial planning at all levels continues to be created, from the whole country (Russian Federation Development Strategy) to municipalities and settlements (general plans).

It should be noted that in most modern publications devoted to the issue of sustainable development a vast territory is considered – up to the whole planet. Considering the global character of the problem and interrelatedness of the processes occurring on the Earth, it is clear. At the same time, even global problems often occur at a local level. Global models are not almost able to consider quality of life in a specific locality or pollution from specific industrial enterprises. But these facts are accounted in general plans of cities and settlements and in territorial planning schemes of municipalities.

In our opinion, exactly those documents could be the source for solving problems of sustainable development of territories. The main advantages of the situation analysis at this level are:

• a large scale for natural component research, ability to localize a specific planned facilities as well and analysis of their possible impact on the environment and human;

• possibility of territorial differentiation, identification of spatial patterns.

All this allow to evaluate properly various territory potentials (agricultural, industrial, demographical, recreational, etc.), as well as restrictions on the territory using, in violations of which will reduce these potentials, territory regression.

There is a need of a complex analysis of the situation, a systematic approach to the territorial planning to meet the required balance of the territory, which will maximize profit of mankind without causing damage to environment (Белоусов, Трухачев, 2007).

The modern paradigm of sustainable development implies a triune concept (Константинова, Вараскин, 2010). There are economic, social and environment components. The first is capacities, buildings, infrastructure, etc. The second is the human capital; it means public health, intellectual potentials, life quality, etc. The third component of sustainable development is environment. Some authors, in addition to natural resources and conditions, refer to it urban environment.

Sustainable development of the territory occurs when all this components develop balanced, not to the detriment of each other. In our opinion, analyzing of the situation, it is advisable to explore each subsystem of territory by an analytical way, and then synthesize obtained results to represent a unified picture.

Nowadays, such scheme of complex analysis to define stability of the territory and making forecast estimations could be realized most successfully with the help of geographic information systems (GIS). Functionality and presentation data by layers allow to analyze the interaction of various factors of territory development and identify patterns of manifestation of some natural or socio-economic phenomena.

It is necessary to rely on the triune concept in the designing of GIS models to ensure sustainable development of territories. However, it should be noted, that structure of models' blocks can differ from structure of sustainable development components. So, in our view, it is necessary to divide models of natural conditions and ecological models, because the first ones reflect natural

factors of territory development, and the second ones reflect anthropogenic impact on the environment. Also it is advisable to allocate the infrastructure block from economic component. Transport networks, energy networks, gas and communication supply today actually determine territory of the socio-economical development stage. But it should be noted, that the proper planning of infrastructure, as they mostly affect the level of anthropogenic impact and pollution, especially in very large areas of municipal districts, is very important.

Consider each block in more detail.

Natural conditions.

This block is largely fundamental in territory analysis, because a natural component is the base for development of both society and industry and infrastructure. Analyzing this block it is advisable to create cartographic models for each landscape component, such as soil, soil-forming rocks, vegetation, climate, etc.

Thus each of the elements was evaluated in terms of favorability of certain conditions for living and human activities. For example, it is difficult to talk about sustainable development of desert areas, where it is virtually impossible to provide the required level of human life.

Ecological block.

The most important aim in ensuring sustainable development of the territory is to minimize the negative impact of human activities on the environment. Accordingly, GIS models have to reflect human impact on environment. Maps of the soil cover pollution, surface water and groundwater pollution, noise pollution, etc. could be submitted as a model of such effects. It is also possible to organize predictions of environmental pollution during emergency situations in industrial plants and infrastructure facilities.

On the other hand, there is a possibility of negative impacts of natural processes on infrastructure, agricultural lands, buildings and human. In this context, it is important to create models of dangerous natural processes that could damage technogenic objects, which may lead to serious consequences for the whole ecosystem. Detection of these adverse zones during the construction facilities, transport routes and other technogenic objects can significantly reduce the risk of emergency situations, and therefore pollution.

Economical block.

In economic block of models such factors as industrial enterprises, companies of service sector, agricultural enterprises, number of jobs, wages levels, etc. should be considered

Geographic information systems can easily handle with large amount of statistical data that have spatial reference, that allow to obtain new information from existing data set, monitoring the dynamics of various parameters, produce a multivariate analysis.

All this allow to identify depressive areas, as well as points of growth, which could become a competitive advantage for a given area in the future.

Social block.

An important component of sustainable development of the territory is the quality of life. Social and demographic characteristics are largely dependent of the economic situation, but are not completely determined by them. The above features of geographic information systems also contribute to process demographic information. With the help of overlay operations, or the graphic overlay dissimilar layers, it may reveal patterns of social development and identify positive and negative factors that affect on this development.

Infrastructure block.

In our opinion, it is expedient to consider the infrastructure of municipal districts as a separate major component of the sustainable development of the territory, because evaluation issues of integrated area development is closely linked with the analysis of energy, communications, computer, transportation of hydrocarbons, transport, social, etc. infrastructure facilities placement (Варгина, Мякиенков, 2008).

The important parameters in assessing of infrastructure are, firstly, its accessibility to the local population (distance from roads, telephone services, the availability of broadcast television, etc.), and secondly, its impact on the environment. So, it is necessary to consider risks of emergencies in pipelines, railways and roads, etc.

Synthetic models.

After a set of analytical models for each block have been created, it is necessary to make them to a united system of measurement. First, a synthetic model in each block should be created, which shows the overall situation, identifying territory that most and least satisfy sustainable development conditions. For example, for social block an assessment of human development index could be such a model. For natural block it is stability of the territory to impact of anthropogenic factors. For the ecological block it is territory pollution overall assessment. For the infrastructure block it is overall supply of infrastructure facilities, taking into account the density of road network and availability of other infrastructure facilities. All integrated models for each of blocks should have a point scale assessment of the situation, which should be comparable with each other. Such models are needed to identify problem areas in terms of one or another factor of sustainable development.

Then a common synthetic model for all factors will be needed to create. It will allow to identify as least wealthy areas as areas that could become the points of growth.

Thus, the wide range of models, both analytical and synthetic, that allow properly to estimate the current situation in the territory of a municipal district

can be created by means of geographic information systems. This assessment can greatly simplify making planning decisions that contribute to competent management and implementation of measures aimed at sustainable development of the territory.

REFERENCES:

1. *Белоусов В. Н., Трухачев Ю. Н.* Системный подход в территориальном планировании // Управление развитием территории. 2007. № 2. С. 50–51.
2. *Варгина Т. В., Мякиенков В. М.* Вопросы реализации положений в области территориального планирования // Управление развитием территории. 2008. № 1. С. 34–38.
3. *Константинова Е. Д., Вараскин А. Н.* Методология системного анализа взаимосвязей между факторами риска и здоровьем населения в задаче устойчивого развития // Устойчивое развитие : наука и практика. 2010. № 2. С. 68–85.
4. Градостроительный кодекс Российской Федерации. М. : Проспект, КНОРУС, 2009. 128 с.
5. Доклад Конференции Организации Объединенных Наций по окружающей среде и развитию. Т. I. Резолюции, принятые на конференции / Нью-Йорк: Организация объединенных наций, 1993. 528 с.

SOIL MAPPING AND MONITORING BASED ON REMOTE SENSING DATA

E. Y. Kiryanova

Russian State Agrarian University – Moscow Agricultural Academy named after K. A. Timiryazev

Information about soil cover is considered to be of great importance to agricultural production. Soil properties determine cultivated crop range, farming techniques, as well as farm produce quality. Taking into account soil characteristics one enables to perform both economically- and ecologically-wise agricultural production.

Currently soil maps are known to be the main source of soil data. It should be pointed out that the existing soil maps in the Russian Federation have become obsolete as they have not been updated during the last 30 years. Consequently there is a lack of information about soil cover changes which have occurred recently. Meanwhile the issue of soil monitoring, especially concerning arable lands, is very urgent nowadays due to the negative tendencies in the soil formation processes (water and wind erosion, dehumification, salinization, acidation).

It is widely known that the soil cover of every natural zone is characterized by heterogeneity. Frequently accompanying contrast components influ-

ence soil usage and resource potential greater than the dominant ones. Therefore soil cover heterogeneity is given so much attention in any soil-mapping and land evaluation activities (Фридланд, 1972; Белобров, 1973; Кирюшин, 2000). However the issue of soil heterogeneity mapping and monitoring is still urgent. Recently developed remote sensing techniques and increased satellite data availability (including archive information) provide new promising possibilities for dealing with the problems of both digital soil mapping and soil monitoring.

Relying on the modern possibilities of the remote sensing the following approach to the digital soil mapping of arable lands has been developed. The first step includes the analyzing of satellite data and performing of image classification in the GIS-environment. At the second step such a classification should be supported with the relief information presented in the form of digital elevation models or digitized topographic maps. The final step is to interpret the obtained image segments taking into account the results of the soil mapping survey, which means the filling-in of the database with attributive soil information. It should be mentioned that various satellite data can be used in digital soil mapping.

To map soil cover heterogeneity, the soil line concept has been proposed (Richardson and Wiegand, 1977). Soil line is a relationship between the reflectance of bare soil in the near-infrared (NIR) and red (R) spectral bands:

$$NIR = \beta_1 R + \beta_0,$$

where β_1 – slope and β_0 – intercept.

Changes in the soil line parameters are considered to be the indicators of changes in soil properties. Satellite data acquired with Landsat TM-5 has been used to design the maps of soil cover heterogeneity (Figure 1).
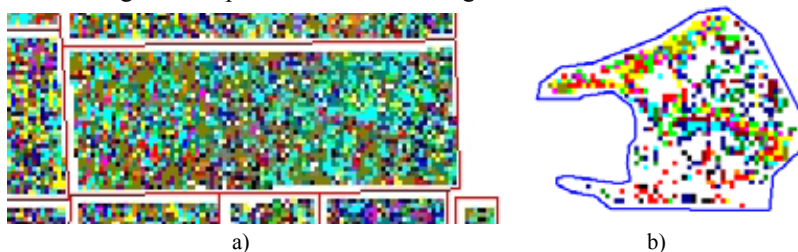

a)   b)

Figure 1. Examples of soil heterogeneity maps for arable lands of two plots located in the Saratov Oblast: a) "Kruchi"; b) "Tatischevo" (pixels belonging to one soil line class are shown in similar color)

It should be pointed out that to turn from the evaluation of bare soil surface color to the direct interpretation of soil cover properties it is necessary to carry out an additional investigation of relationships between the soil classification position and the color of soil surface layer.

Therefore at the current research stage it is proposed to use joint analysis of three spectral bands of Landsat TM-5 (scene from 18.08.2011): 7, 5, 3 as the basis for digital soil mapping with optical satellite data (Figure 2).

Figure 2. The example of digital soil map for test plot in the Saratov Povolzhye

Other types of satellite data such as radar information can also be used as the input data for the soil cover heterogeneity analysis alongside with spectral information.

It should be mentioned that due to radar data properties digital soil maps obtained on the basis of radar information are characterized by greater generalization in comparison with the maps based on optical satellite data.

It is necessary to draw attention to the fact that satellite data can be used not only for soil mapping as a whole, but for the mapping of certain soil properties such as *stoniness*.

A number of field points with known stoniness and coordinates is used as input data, as well as radar data of high resolution (September 2011) and optical satellite data of moderate resolution (Landsat TM-5, scene from 18.08.2011).

Models of multiple regression are developed using STATISTICA 7 program, then the stoniness maps in the GIS-environment are designed on the basis of the developed models.

It is essential that statistically significant regression relationships between stoniness and surface reflectance have been revealed when both radar and optical data (Landsat TM-5) were used in the modeling process. The highest statistically significant coefficients of correlation (**0,758640**) and determination (**0,575534**) have been acquired when the model relies on the radar data from 14.09.2011 (vh-polarization) and 2, 4, 6 Landsat TM-5 bands:

Wpov%=-446,786−0,004rad14vh-1,876LT2+2,104LT4+2,532 LT6±0,638698,

where Wpov% – surface stoniness of certain point (%), rad14vh – spectral properties of the point obtained from radar data of vh-polarization from 14.09.2011, LT2 – spectral properties of point in 2 Landsat TM-5 band, LT4 –

spectral properties of point in 4 Landsat TM-5 band, LT6 –spectral properties of point in 6 Landsat TM-5 band.

The example of the stoniness map for the test site in the Saratov Pov-olzhye is shown in Figire 3.
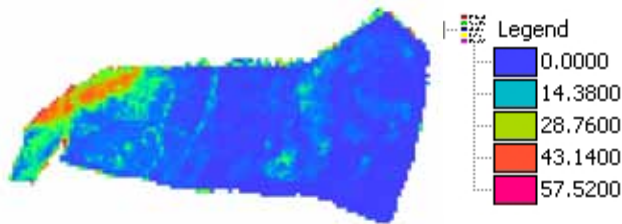

Figure 3. The example of the stoniness map (percent of stoniness) for the test site in the Saratov Povolzhye

Satellite data can also provide the basis for soil monitoring. The soil line concept can be applied to evaluate the dynamics of soil properties as well. Time changes in the soil line parameters are considered to be the indicators of changes in soil characteristics.

Such an approach provides a possibility to mark out the plots where sharp or gradual changes in the soil properties have taken place and to assess the general course of the undergoing changes (trend estimation using Foster- Stuart method). As a result of the practical application of the described method one can consider the map of soil cover dynamics of the test plot for the recent 30 years which was developed after the analysis of 17 Landsat TM-5 scenes from 1984 up to 2011.

As soil reflectance depends on the complex of properties, it is necessary to carry out further research to determine the relationships between changes in certain soil characteristics or groups of characteristics and changes in slope of the soil line. It will enable to turn from an assessment of general dynamics to the dynamics of specific soil properties.

The above mentioned approaches to digital soil mapping can be applied mainly to analyze bare soil surface. However, most of the time the soil surface of arable lands is covered with vegetation. Moreover satellite data, obtained for bare soil surface, cannot potentially reflect the heterogeneity as a whole. Therefore additional data on soil characteristics can be obtained by analyzing crop development. Such an evaluation is based on graphs of changes in vegetation index (NDVI) relying on MODIS satellite data which is available at the satellite service "VEGA" from 2001 up to date (http://vega.smislab.ru/) (Лупян и др., 2011).

Thus, remote sensing data provide a wide range of opportunities for investigating and mapping of both the soil cover and specific soil properties.

It has been demonstrated that digital soil mapping can be carried out by applying both optical and radar data. At the same time the soil line concept or the classification of multispectral satellite data can provide the basis for map-

ping. Moreover satellite data analysis alongside with the application of the soil line concept provides valuable information for soil monitoring.

In case of arable lands, data on crop development, evaluated by the graphs of changes in vegetation index NDVI, are considered to be an important additional source of information relating to the soil cover characteristics.

In conclusion, at the current stage of research the verification of the approaches based on satellite data should be carried out with regard to data obtained from the field soil survey. The approaches are sure to be of great potential and information value and require further development and improvement.

REFERENCES

1. *Белобров В. П.* Об определении контрастности почв и почвенного покрова. D кн.: Структура почвенного покрова и методы ее изучения. М., 1973. С. 89–95.
2. *Кирюшин В. И.* Экологизация земледелия и технологическая политика. М. : МСХА, 2000. 473 с.
3. *Лупян Е. А., Савин И. Ю., Барталев С. А., Толпин В. А., Балашов И. В., Плотников Д. Е.* Спутниковый сервис мониторинга состояния растительности («Вега») // Современные проблемы дистанционного зондирования Земли из космоса, 2011. Т. 8. № 1. С. 190–198.
4. *Фридланд В. М.* Структура почвенного покрова. М. : Мысль, 1972. 423 с.
5. *Richardson A. J., Wiegand C. L.* Distinguishing vegetation from soil background information // Photogramm. Eng. Remote Sens. 1977. № 43. P. 1541–1552.
6. URL: http://vega.smislab.ru/.

A UNIQUENESS THEOREM FOR SOLUTIONS TO THE INVERSE STURM-LIOUVILLE PROBLEM

A. E. Kvashchuk

Saratov State University

Introduction

One of the most crucial aspects of the spectral theory of differential operators is the inverse spectral problem which is aimed at recovering operators from its spectral characteristics. One of these spectral characteristics for the differential Sturm-Liouville operator is the Weyl function. Such problems play a significant role in various areas of mathematics and have a number of applications in mechanics, physics, electronics, meteorology and other fields of science and technology. Inverse problems have also had a major impact on mathematical physics, especially on solving nonlinear evolution equations.

The aim of this paper is to prove the uniqueness of the solution to the inverse spectral problem for the Sturm-Liouville operator on a finite interval

$$-y'' + q(x)y = \lambda y, \ U(y) = y'(0) - hy(0) = 0, \ y(\pi) = 0.$$

The operator is recovered from the Weyl function.

To pursue this aim we should do the following:

- to explore the theoretical and historical aspects of the problem;

- to introduce the Weyl function and the corresponding Weyl solution to the boundary value problem;

- to prove the corresponding uniqueness theorem.

Historical aspect

The first works on the spectral theory of the Sturm-Liouville operators belong to Bernoulli, J.-L. D'Alembert and Euler, and were written more than two hundred years ago (Марченко, 1977). These works were aimed mainly at solving the equation which describes the vibration of a string.

The spectral theory was developed considerably in the XX century. It was due to scholarly contributions of D. Hilbert, H. Weyl, G. Birkhoff, J. von Neumann, V. A. Steklov and other mathematicians. The spectral theory acquired especial importance after the birth of quantum mechanics. It became not only a method of solving problems but also the language of quantum mechanics (Марченко, 1977).

As for the theory of inverse spectral problems, the first outstanding achievement was Ambarzumian's proof of the uniqueness theorem. Later G. Borg showed that the Ambarzumian's result was just a special case of inverse spectral problem. He also solved the problem of determination of the potential from two eigenvalue sequences corresponding to two boundary value problems with the common differential equation and one common boundary condition. The most comprehensive research on inverse problem solutions of spectral analysis for the Sturm-Liouville operators was carried out by B. Levitan, I. Gelfand, V. Marchenko, M. Krein. At present inverse problems are the most critical aspect of the spectral theory.

The main definitions, **theorems** and lemmas

Consider the boundary value problem $L = L(q(x), h)$:

$$\ell y := -y'' + q(x)y = \lambda y, \ 0 < x < \pi \tag{1}$$

$$U(y) = y'(0) - hy(0) = 0, \ y(\pi) = 0 \tag{2}$$

Here λ is the spectral parameter, $h \in R$, $q(x)$ is real function, $q(x) \in L_2(0, \pi)$, which is called potential. The operator ℓ is called the Sturm-Liouville operator.

Let $\varphi(x, \lambda)$ and $S_1(x, \lambda)$ be solutions of (1) under the following initial conditions:

$$\varphi(0,\lambda)=1, \ \varphi'(0,\lambda)=h;$$

$$S_1(\pi,\lambda)=0, \ S_1'(\pi,\lambda)=-1.$$

For each fixed x these functions are entire in λ.
Denote

$$\Delta(\lambda)=\langle S_1(x,\lambda),\varphi(x,\lambda)\rangle,$$

where

$$\langle y(x),z(x)\rangle := y(x)z'(x)-y'(x)z(x)$$

is the Wronskian of y and z (Freiling, Yurko, 2001). The function $\Delta(\lambda)$ is entire in λ and has at most countable set of zeros $\{\lambda_n\}_{n=1}^{\infty}$.

Clearly, the representation

$$\Delta(\lambda)=\varphi(\pi,\lambda)=-U(S_1) \tag{3}$$

is true.

Theorem 1

The zeros $\{\lambda_n\}_{n=1}^{\infty}$ of the characteristic functions $\Delta(\lambda)$ coincide with the eigenvalues of boundary value problem L. The functions $\varphi(x,\lambda)$ and $S_1(x,\lambda)$ are eigenfunctions, and there exists a sequence $\{\beta_n\}_{n=1}^{\infty}$ such that

$$S_1(x,\lambda)=\beta_n\varphi(x,\lambda),\beta_n\neq 0 \tag{4}$$

Proof. 1) Let λ_0 be a zero of $\Delta(\lambda)$, that is

$$S_1(x,\lambda_0)\varphi'(x,\lambda_0)-S_1'(x,\lambda_0)\varphi(x,\lambda_0)=0.$$

Substituting in this equation $x=0$, $x=\pi$ and taking into account the initial conditions, we obtain $U(S_1(0,\lambda_0))=0$ и $\varphi(\pi,\lambda_0)=0$. Thereby $\varphi(x,\lambda)$ and $S_1(x,\lambda)$ satisfy (2) and hence they are eigenfunctions.

2) Let λ_0 be an eigenvalue of L, and let y_0 be a corresponding eigenfunction. That is $U(y_0)=0$. It means $y_0'(0)\neq 0$ (otherwise if $y_0'(0)=0$, then $y_0(0)=0$ and by the uniqueness theorem for the Cauchy problem $y_0\equiv 0$). Without loss of generality, we put $y_0'(0)=h$, this yields $y_0(0)=1$ and $y_0(x)\equiv\varphi(x,\lambda)$. Then

$$\Delta(\lambda_0)=S_1(\pi,\lambda_0)\varphi'(\pi,\lambda_0)-S_1'(\pi,\lambda_0)\varphi(\pi,\lambda_0)=\varphi(\pi,\lambda_0)=y_0(\pi)=0.$$

Thereby λ_0 is a zero of function $\Delta(\lambda)$. We also proved that each eigenvalue corresponds to only one (up to a multiplicative constant) eigenfunction.

Denote

$$\alpha_n := \int_0^\pi \varphi^2(x,\lambda_n)dx \tag{5}$$

and call them *the weight numbers*. The numbers $\{\lambda_n,\alpha_n\}_{n=1}^\infty$ are called *spectral data* of the boundary value problem L.

Lemma 1. *The following relation holds*

$$\beta_n\alpha_n = -\dot{\Delta}(\lambda_n), \tag{6}$$

where the numbers β_n are defined by (4), and $\dot{\Delta}(\lambda) = \dfrac{d}{d\lambda}\Delta(\lambda)$.

Proof.

Since

$$-S_1''(x,\lambda) + q(x)S_1(x,\lambda) = \lambda S_1(x,\lambda), \quad -\varphi''(x,\lambda_n) + q(x)\varphi(x,\lambda_n) = \lambda_n\varphi(x,\lambda_n),$$

then

$$\frac{d}{dx}\langle S_1(x,\lambda),\varphi(x,\lambda_n)\rangle = S_1(x,\lambda)\varphi''(x,\lambda_n) - S_1''(x,\lambda)\varphi(x,\lambda_n) = (\lambda-\lambda_n)S_1(x,\lambda)\varphi(x,\lambda_n),$$

and as a consequence, we get

$$(\lambda-\lambda_n)\int_0^\pi S_1(x,\lambda)\varphi(x,\lambda_n)dx = \langle S_1(x,\lambda),\varphi(x,\lambda_n)\rangle\Big|_0^\pi = \varphi(\pi,\lambda_n) + U(S_1(0,\lambda)) = -\Delta(\lambda).$$

For $\lambda \to \lambda_n$, this yields

$$\int_0^\pi S_1(x,\lambda_n)\varphi(x,\lambda_n)dx = -\dot{\Delta}(\lambda_n).$$

Using (4), (5) we arrive at (6).

Lemma 2. *For $|\rho| \to \infty$ the following asymptotic formulas are valid*

$$\varphi(x,\lambda) = \cos\rho x + O(\frac{1}{|\rho|}\exp(|\tau|x)) = O(\exp(|\tau|x)), \tag{7}$$

$$\varphi'(x,\lambda) = -\rho\sin\rho x + O(\exp(|\tau|x)) = O(|\rho|\exp(|\tau|x)), \tag{8}$$

$$S_1(x,\lambda) = \frac{\sin\rho(\pi-x)}{\rho} + O(\frac{1}{|\rho|^2}\exp(|\tau|(\pi-x))) = O(\frac{1}{|\rho|}\exp(|\tau|(\pi-x))), \tag{9}$$

$$S_1'(x,\lambda) = -\cos\rho(\pi-x) + (\frac{1}{|\rho|}\exp(|\tau|(\pi-x))) = O(\exp(|\tau|(\pi-x))) \tag{10}$$

$$|\Delta(\lambda)| \geq C_\delta \exp(|\tau|\pi), \rho \in D_\delta = \left\{ \rho : \left| \rho - k - \frac{1}{2} \right| \geq \delta, k = 0, \pm 1, \pm 2, \ldots \right\}, \delta > 0 \quad (11)$$

uniformly with respect to $x \in [0, \pi]$.

Here and in the sequel $\lambda = \rho^2, \tau = \operatorname{Im}\rho$.

Proof. The proof of (7) and (8) is given in (Freiling, Yurko, 2001).

Consider the Volterra integral equation

$$y(x, \lambda) = \frac{\sin \rho x}{\rho} + \int_0^x \frac{\sin \rho(x - t)}{\rho} q(t) y(t, \lambda) dt \cdot \quad (12)$$

Clearly it has a unique solution. On the other hand, if $y(x, \lambda)$ satisfies this equation then a double differentiation gives

$$y''(x, \lambda) + \rho^2 y(x, \lambda) = q(x) y(x, \lambda), \quad y(0, \lambda) = 0, \quad y'(0, \lambda) = 1.$$

Differentiating (12), we get

$$y'(x, \lambda) = \cos \rho x + \int_0^x \cos \rho(x - t) q(t) y(t, \lambda) dt. \quad (13)$$

Denote $\mu(\lambda) = \max_{0 \leq x \leq \pi}(|y(x, \lambda)| \exp(-|\tau|x))$. Since $|\cos \rho x| \leq \exp(|\tau|x)$ and $|\sin \rho x| \leq \exp(|\tau|x)$ then from (12) we get that for $|\rho| \geq 1, x \in [0, \pi]$ the following estimate takes place

$$|y(x, \lambda)| \exp(-|\tau|x \leq \frac{1}{\rho}(C_1 + \mu(\lambda)C_2),$$

and consequently (for sufficiently large ρ) $y(x, \lambda) = O(\frac{1}{|\rho|} \exp(|\tau|x))$.

Substituting this into the right-hand side of (12) and (13), we arrive at

$$y(x, \lambda) = \frac{\sin \rho x}{\rho} + O(\frac{1}{|\rho|^2} \exp(|\tau|x)) = O(\frac{1}{|\rho|} \exp(|\tau|x)),$$

$$y'(x, \lambda) = -\cos \rho x + (\frac{1}{|\rho|} \exp(|\tau|x)) = O(\exp(|\tau|x)).$$

Then, since

$$S_1''(x, \lambda) + \rho^2 S_1(x, \lambda) = q(x) S_1(x, \lambda), \quad S_1(\pi, \lambda) = 0, \quad S_1'(\pi, \lambda) = -1,$$

the function $\tilde{y}(x, \lambda) := S_1(\pi - x, \lambda)$ satisfies the following equations and initial conditions

$$\tilde{y}''(x, \lambda) + \rho^2 \tilde{y}(x, \lambda) = q(\pi - x) \tilde{y}(x, \lambda), \quad \tilde{y}(0, \lambda) = 0, \quad \tilde{y}'(0, \lambda) = 1.$$

Thus, obtained asymptotic estimates are valid for the function $\tilde{y}(x,\lambda)$. It now follows that

$$S_1(x,\lambda) = O(\frac{1}{|\rho|}\exp(|\tau|(\pi - x)))\,.$$

Therefore, taking into consideration estimates for $y(x,\lambda)$ and the last formulae, we arrive at (9) and (10).

Let's obtain (11). According to (3) $\Delta(\lambda) = -U(S_1) = S_1'(0,\lambda) - hS_1(0,\lambda)$, then taking into account (12) and (13) we get

$$\Delta(\lambda) = -\cos\rho\pi - h\frac{\sin\rho\pi}{\rho} + O(\frac{1}{|\rho|}\exp|\tau|\pi)\,.$$

Denote

$$G_\delta = \left\{\rho : |\rho - k| \geq \delta, k = 0, \pm 1, \pm 2, \ldots\right\}, \delta > 0,$$

$$D_\delta = \left\{\rho : \left|\rho - k - \frac{1}{2}\right| \geq \delta, k = 0, \pm 1, \pm 2, \ldots\right\}, \delta > 0\,.$$

It known that $|\sin\rho\pi| \geq C_\delta \exp(|\tau|\pi), \rho \in G_\delta, |\cos\rho\pi| \geq C_\delta \exp(|\tau|\pi), \rho \in D_\delta$. Consequently $|\Delta(\lambda)| \geq C_\delta \exp(|\tau|\pi)$, $|\lambda| \geq \lambda^*$ for sufficiently large λ^*.

Main results: the proof of the uniqueness theorem with the help of the Weyl function

Let $\Phi(x,\lambda)$ be solutions of (1) under the following initial conditions $U(\Phi) = 1$, $\Phi(\pi,\lambda) = 0$. We set $M(\lambda) := \Phi(0,\lambda)$. The functions $\Phi(x,\lambda)$ and $M(\lambda)$ are called the Weyl solution and the Weyl function for the boundary value problem L, respectively.

One can easily check that

$$\Phi(x,\lambda) = -\frac{S_1(x,\lambda)}{\Delta(\lambda)}\,, \quad M(\lambda) = -\frac{S_1(0,\lambda)}{\Delta(\lambda)}\,. \tag{14}$$

The following representation is also equally true:

$$\Phi(x,\lambda) = S_1(x,\lambda) + M(\lambda)\varphi(x,\lambda)\,. \tag{15}$$

It is easy to show that

$$\langle \varphi(x,\lambda), \Phi(x,\lambda) \rangle = 1\,. \tag{16}$$

Theorem 2. *The following representation holds:*

$$M(\lambda) = \sum_{n=1}^{\infty} \frac{1}{\alpha_n(\lambda - \lambda_n)}\,. \tag{17}$$

Proof. From (9), (11), (14) we get the following estimate

$$|M(\lambda)| \le \frac{C_\delta}{|\rho|}, \ |\rho| \ge \rho^*, \tag{18}$$

for sufficiently large $\rho^* > 0$.

Let us count residues of $M(\lambda)$ using representation (14), definition $M(\lambda)$ and lemma 1

$$\operatorname*{Res}_{\lambda=\lambda_n} M(\lambda) = -\frac{S_1(0,\lambda_n)}{\dot\Delta(\lambda_n)} = -\frac{\beta_n \varphi(0,\lambda_n)}{\dot\Delta(\lambda_n)} = \frac{1}{\alpha_n}.$$

Consider the contour integral

$$J_N(\lambda) = \frac{1}{2\pi i} \int_{\Gamma_N} \frac{M(\mu)}{\lambda - \mu} d\mu, \lambda \in \operatorname{int} \Gamma_N,$$

where $\Gamma_N = \left\{ \lambda : |\lambda| = (N+1/2)^2 \right\}$ (with counter clockwise circuit).

Using (1) we get $\lim\limits_{N\to\infty} J_N(\lambda) = 0$. On the other hand, by the residue theorem $J_N(\lambda) = -M(\lambda) + \sum\limits_{n=0}^{N} \frac{1}{\alpha_n(\lambda - \lambda_n)}$.

Thus, the theorem is proved.

Inverse problem: given the Weyl function $M(\lambda)$, construct $L = L(q(x), h)$.

Theorem 3. *If* $M(\lambda) = \tilde M(\lambda)$, *then* $L = \tilde L$. *Thus, the specification of the Weyl function uniquely determines the potential* $q(x)$ *and the coefficient of the boundary condition.*

Proof. Let us define the matrix $P(x,\lambda) = \left[P_{jk}(x,\lambda) \right]_{j,k=1,2}$ by the formula

$$P(x,\lambda)\begin{bmatrix} \tilde\varphi(x,\lambda) & \tilde\Phi(x,\lambda) \\ \tilde\varphi'(x,\lambda) & \tilde\Phi'(x,\lambda) \end{bmatrix} = \begin{bmatrix} \varphi(x,\lambda) & \Phi(x,\lambda) \\ \varphi'(x,\lambda) & \Phi'(x,\lambda) \end{bmatrix}. \tag{19}$$

Using (19) we get

$$P_{11}(x,\lambda)\tilde\varphi(x,\lambda) + P_{12}(x,\lambda)\tilde\varphi'(x,\lambda) = \varphi(x,\lambda),$$

$$P_{11}(x,\lambda)\tilde\Phi(x,\lambda) + P_{12}(x,\lambda)\tilde\Phi'(x,\lambda) = \Phi(x,\lambda).$$

If we combine this with (16) we get

$$P_{11}(x,\lambda) = -\Phi(x,\lambda)\tilde\varphi'(x,\lambda) + \varphi(x,\lambda)\tilde\Phi'(x,\lambda),$$

$$P_{12}(x,\lambda) = -\varphi(x,\lambda)\tilde\Phi(x,\lambda) + \tilde\varphi(x,\lambda)\Phi(x,\lambda).$$

Then

$$P_{11} = \frac{S_1(x,\lambda)\tilde{\varphi}'(x,\lambda)}{\Delta(\lambda)} - \frac{\varphi(x,\lambda)\tilde{S}_1'(x,\lambda)}{\Delta(\lambda)} + 1 - \frac{S_1(x,\lambda)\varphi'(x,\lambda)}{\Delta(\lambda)} + \frac{S_1'(x,\lambda)\varphi(x,\lambda)}{\Delta(\lambda)} =$$

$$= 1 + \frac{1}{\Delta(\lambda)}(S_1(x,\lambda)(\tilde{\varphi}'(x,\lambda) - \varphi'(x,\lambda)) - \varphi(x,\lambda)(\tilde{S}_1'(x,\lambda) - S_1'(x,\lambda))) \quad .$$

$$P_{12} = \frac{\varphi(x,\lambda)\tilde{S}_1(x,\lambda)}{\Delta(\lambda)} - \frac{S_1(x,\lambda)\tilde{\varphi}(x,\lambda)}{\Delta(\lambda)} =$$

$$= \frac{1}{\Delta(\lambda)}(-\tilde{\varphi}(x,\lambda)S_1(x,\lambda) + \tilde{S}_1(x,\lambda)\varphi(x,\lambda)) \quad .$$

This gives the following estimates

$$\left|P_{11}(x,\lambda) - 1\right| \le \frac{C_\delta}{|\rho|}, \ \left|P_{12}(x,\lambda)\right| \le \frac{C_\delta}{|\rho|}, \ |\rho| \ge \rho^* .$$

According to (15) this yields

$$P_{11}(x,\lambda) = \varphi(x,\lambda)\tilde{S}_1'(x,\lambda) - S_1(x,\lambda)\tilde{\varphi}'(x,\lambda) + (\tilde{M}(\lambda) - M(\lambda))\varphi(x,\lambda)\tilde{\varphi}'(x,\lambda) ,$$

$$P_{12}(x,\lambda) = \tilde{\varphi}(x,\lambda)S_1(x,\lambda) - \varphi(x,\lambda)\tilde{S}_1(x,\lambda) - (\tilde{M}(\lambda) - M(\lambda))\varphi(x,\lambda)\tilde{\varphi}(x,\lambda) .$$

Finally, we obtain if $M(\lambda) \equiv \tilde{M}(\lambda)$, then for each fixed x, the functions $P_{11}(x,\lambda)$ and $P_{12}(x,\lambda)$ are entire in λ. It gives $P_{11}(x,\lambda) \equiv 1$, $P_{12}(x,\lambda) \equiv 0$, this entails $\varphi(x,\lambda) \equiv \tilde{\varphi}(x,\lambda)$, $\Phi(x,\lambda) \equiv \tilde{\Phi}(x,\lambda)$ for all x and λ, and consequently $q(x) \equiv \tilde{q}(x)$ a.e. on $(0,\pi)$, $h \equiv \tilde{h}$.

Conclusion

The Weyl function is a very convenient and effective tool for investigating the inverse boundary problem. Using this spectral characteristic we can study inverse problems for a large number of operator classes. In particular, the Weyl function can be used with the Sturm-Liouville operator on the half-line.

The main result of this paper is the proof that the Weyl function uniquely determines the Sturm-Liouville operator on a finite interval. We have also shown the Weyl function decomposition in series. It yields the equivalence of specification of the Weyl function and spectral data. This leads to the fact that the specification of the Weyl function is equivalent to the specification of two spectra.

References

1. *Марченко В. А.* Спектральная теория операторов Штурма-Лиувилля. Киев, 1927.
2. *Freiling G., Yurko V.* Inverse Sturm-Liouville problems and their applications // Nova Science Publishers, Inc. Huntington ; N. Y., 2001.

BUGS FOR A BAYESIAN ANALYSIS
OF STOCHASTIC VOLATILITY MODELS

N. A. Kucher

Saratov State University

INTRODUCTION

This paper reviews the analysis of stochastic volatility models using the software package BUGS (Bayesian Inference Using Gibbs Sampling).

BUGS is an ideal software tool for the exploratory phase of model building as any modifications of a model including changes of priors and sampling error distributions are readily realized with only minor changes of the code. BUGS automate the calculation of the full conditional posterior distributions using a model representation by directed acyclic graphs. It contains an expert system for choosing an efficient sampling method for each full conditional. Furthermore, software for convergence diagnostics and statistical summaries is available for the BUGS output.

Scientific interest in the mathematical modeling in the theory of finance due to the revolutionary transformation of the financial market, changes in its structure, increases volatility in prices, the emergence of new financial instruments, the use of modern information technology for the analysis of prices, which presents to financial theory, respectively, new requirements and sets new problem, the solution of which is necessary to conduct deep research in the field of mathematical modeling of financial processes. Being a large and complex system with lots of variables and relations of various factors, the financial markets require rather complex mathematical methods for their analysis, methods of statistical data processing, numerical methods and computer tools.

The main purpose of this research is to illustrate the ease with which the Bayesian stochastic volatility model can now be studied using BUGS.

MATERIALS AND METHODS

The stochastic volatility (SV) model introduced by Tauchen and Pitts (1983) and Taylor (1982) is used to describe financial time series. It offers an alternative to the ARCH-type models of Engle (1982) and Bollerslev (1986) for the well documented time varying volatility exhibited in many financial time series. The SV model provides a more realistic and flexible modeling of financial time series than the ARCH-type models, since it essentially involves two noise processes, one for the observations, and one for the latent volatilities. The so called observation errors account for the variability due to measurement and sampling errors whereas the process errors assess variation in the

underlying volatility dynamics (see, for example, Danielsson (1994), Geweke (1994), and Kim et al. (1998) for the comparative advantages of the SV model over the ARCH-type models).

Unfortunately, classical parameter estimation for SV models is difficult due to the intractable form of the likelihood function. Recently, a variety of frequentist estimation methods have been proposed for the SV model, including Generalized Method of Moments (Melino and Turnbull, 1990), Quasi-Maximum Likelihood (Harvey et al., 1994), Efficient Method of Moments (Gallant et al., 1997), Simulated Maximum Likelihood (Danielsson, 1994), (Sandmann and Koopman, 1996), and approximate Maximum Likelihood (Fridman and Harris, 1998). A Bayesian analysis of the SV model is complicated due to multidimensional integration problems involved in posterior calculations. These difficulties with posterior computations have been overcome, though, with the development of Markov Chain Monte Carlo (MCMC) techniques (Gilks et al. 1996) over the last two decades and the ready availability of computing power. MCMC procedures for the SV model have been suggested by Jacquier et al. (1994), Shephard and Pitt (1997), and Kim et al. (1998).

We estimate a stochastic volatility using the software package BUGS.

For illustrative and comparative purposes, we use the data that consists of a time series of the stock company «Gazprom» $\{x_t\}$ from 09/01/07 to 15/11/11. The series of interest are the daily mean-corrected returns, $\{y_t\}$, given by the

transformation $y_t = \log x_t - \log x_{t-1} - \dfrac{1}{n}\sum_{i=1}^{n}\left(\log x_t - \log x_{t-1}\right)$, $t = 1, ..., n$.

The SV model used for analyzing these data can be written in the form of a nonlinear state-space model. A state-space model species the conditional distributions of the observations given unknown states, here the underlying latent volatilities, $\{\theta_t\}$, and given the unknown observation error variance σ^2, in the observation equations:

$$y_t|\theta_t = \exp\left(\frac{1}{2}\theta_t\right)u_t, \; u_t \sim N(0,1), \, t = 1, ..., n \qquad (1)$$

The unknown states are assumed to follow a Markovian transition over time (therefore the state-space models are often referred to as «hidden Markov models») given by the state equations:

$$\theta_t|\theta_{t-1},\mu,\phi,\tau^2 = \mu + \varphi\left(\theta_{t-1} - \mu\right) + v_t, \; v_t \sim N(0,\tau^2), \, t = 1, ..., n \qquad (2)$$

with $\theta_0 \sim N(\mu,\tau^2)$

The state θ_t determines the amount of volatility on day t and the value of φ, $-1 < \varphi < 1$ measures the autocorrelation present in the logged squared data. Thus φ can be interpreted as the persistence in the volatility, the constant

scaling factor $\beta = \exp\left(\dfrac{1}{2}\mu\right)$ as the modal volatility, and τ as the volatility of log-volatilities.

A full Bayesian model consists of the joint prior distribution of all unobservable, here the three parameters, μ, φ, τ^2 and the unknown states, $\theta_0, \theta_1, ..., \theta_n$ and the joint distribution of the observables, here the daily returns $y_1, y_2, ..., y_n$. Bayesian inference is then based on the posterior distribution of the unobservables given the data.

We estimated a basic model for a time series of daily the stock company «Gazprom» (Appendix 1). Table 1 shows the results. Based on the results, we can conclude that effect of the volatility is denoting on the level of 1%. (Table 1).

Table 1

bugs.log:
Bugs>stats (phi)

mean	sd	2.5%	97.5% CI	median	sample
9.797E-1	1.144E-2	9.524E-1	9.963E-1	9.815E-1	5000

Bugs>stats (tau)

mean	sd	2.5%	97.5% CI	median	sample
1.562E-1	3.184E-2	1.011E-1	2.282E-1	1.537E-1	5000

Bugs>stats (beta)

mean	sd	2.5%	97.5% CI	median	sample
7.209E-1	1.198E-1	5.596E-1	1.018E+0	6.955E-1	5000

To obtain opinions OpenBUGS uses simulation algorithms MKML. These algorithms require significant computation, but they are resistant to some of the details of the tasks for which they apply. This stability is an important characteristic of such systems as BUGS, which will automatically choose an algorithm to obtain the findings. BUGS provides a wide range of algorithms MKML. OpenBUGS implemented in the programming language Component Pascal (CP) among the BlackBox Component Builder, developed by Oberon Microsystems. CP is a fairly modern language, which combines the principles of procedural and object-based programming. Compiled modules contain information, which enables the user to check the modules loaded modular services.

To estimate the parameters of the model of stochastic volatility in a time series of daily the stock company «Gazprom» for the period from 09/01/07 to 15/11/11 applied software package OpenBUGS, which is an effective tool for Bayesian analysis of MSW. For the application environment created OpenBUGS specification model of stochastic volatility in the medium OpenBUGS. As a result, the simulation found that the estimates are quite satisfactory in

terms of accuracy with acceptable computational costs, all estimates are characterized by the convergence at a given time interval; proposed algorithm can be applied to estimate the values of the volatility of the stochastic process and the parameters of stochastic volatility models for various financial processes provided by the statistical data to exchange rates of various currencies.

REFERENCES

1. *Andersen T., Chung H., Sorensen B.* Efficient method of moments estimation of a stochastic volatility model : A Monte Carlo study / J. of Econometrics. 1999. 91, P. 61–87.
2. *Durbin J., Koopman S. J.* Time series analysis of non-Gaussian observations based on state space models from both classical and Bayesian perspectives (with discussion) / J. of the Royal Statistical Society Series. 2000. B 62, P. 3–56.
3. *Ghysels E., Harvey A. C., Renault E.* Stochastic volatility / in Rao, C.R. and G. S. Maddala, ed. / Statistical Models in Finance. North-Holland, Amsterdam, 1996. P. 119–191.

Appendix 1

returns.dat

–0,0281569308

0,9001123324

-0,2559866104

-0,5171401221

0,4429346728

2,2509176191

-1,2334879896

-1,0680573374

1,5774824448

-0,8121288515

-1,1829182822

1,7148863365

1,1531665626

-1,3592540731

-0,9082436822

-0,4148324871

-1,2977120189

0,2477805275

0,5554300111

1,9086190759

1,5702201733

-2,8113991014

-0,1190220046

1,2499608074

1,9141905867

-1,1140871337

……

0,7952505972

0,7223234956

-0,6911207844

-0,1023442277

0,0193853952

-1,8430613953

-0,6886958377

sv.bug:

```
model volatility;
const n=945;
var y [n], yisigma2[n], theta0, theta [n], thmean [n],
mu, beta, phi, phistar, tau, itau2;
data y in «returns.dat»;
inits phistar, mu, itau2 in «sv.in»;
{
# likelihood: joint distribution of ys
for (t in 1:n) {yisigma2[t] <- 1/exp (theta [t]);
y [t] ~ dnorm (0,yisigma2[t]);
}
# prior distributions
mu ~ dnorm (0,0.1);
phistar ~ dbeta (20,1.5);
itau2 ~ dgamma (2.5,0.025);
beta <- exp (mu/2);
phi <- 2*phistar-1;
tau <- sqrt (1/itau2);
theta0 ~ dnorm (mu,itau2);
thmean [1] <- mu + phi*(theta0-mu);
theta [1] ~ dnorm (thmean [1],itau2);
for (t in 2:n) {thmean [t] <- mu + phi*(theta [t-1]-mu);
theta [t] ~ dnorm (thmean [t],itau2);
}}
```

HETEROSKEDASTICITY IN STOCK RETURN DATA: VOLUME VERSUS GARCH EFFECTS

A. I. Malinskiy, A. S. Revutskiy

Saratov State University

The Autoregressive Conditional Heteroskedasticity (ARCH) procedure has been shown to provide a positive fit for many financial data time series. ARCH imposes an autoregressive structure on conditional variance, allowing volatility shocks to survive over time. This persistence captures the propensity of returns of like magnitude to grow in time and can explain the well confirmed nonnormality and nonstability of empirical asset return distributions.

An attractive explanation for the presence of ARCH is based on the hypothesis that daily returns are generated by a mixture of distributions, in which the rate of daily information arrival is the stochastic mixing variable. As suggested, ARCH might catch the time series properties of this mixing variable. However, this linkage has not been widely documented with the data.

The goal of this study is to investigate the validity of this explanation for daily stock returns. The empirical strategy exploits the involvment of the mixture model that the variance of daily price increments is heteroskedastic–specifically, positively related to the rate of daily information arrival. Using daily trading volume as a proxy for the mixing variable, we show that, for a sample of 10 common stocks, ARCH effects disappear when volume is included as an elucidative variable in the conditional variance equation.

The Heteroskedastic Mixture Model and ARCH

The Generalized ARCH (GARCH) model of Bollerslev (1986) restricts the conditional variance of a time series to depend upon past squared residuals of the process. Such a model for daily stock returns is given below:

$$r_t = \mu_{t-1} + \varepsilon_t \tag{1}$$

$$\varepsilon_t \big| (\varepsilon_{t-1}, \varepsilon_{t-2}, \ldots) \sim N(0, h_t) \tag{2}$$

$$h_t = \alpha_0 + \alpha_1(L)\varepsilon_{t-1}^2 + \alpha_2(L)h_{t-1} \tag{3}$$

where r_t represents the rate of return (cum-dividend), μ_{t-1} is the mean r_t conditional on past information, L is the lag operator, and $\alpha_0 > 0$. If the parameters of the lag polynomials $\alpha_1(L)$ and $\alpha_2(L)$ are positive, then shocks to volatility persist over time. The degree of persistence is determined by the magnitude of these parameters.

To motivate the empirical tests of this paper, let δ_{it} denote the ith intraday equilibrium price increment in day t, which implies

$$\varepsilon_t = \sum_{i=1}^{n_t} \delta_{it} \tag{4}$$

The random variable n_t is the mixing variable, representing the stochastic rate at which data flows into the market. Note that ε_t is drawn from a combination of distributions, where the variance of each distribution depends on information arrival time. Equation (4) implies that daily returns are generated by a subordinated stochastic process, in which ε_t is subordinate to δ_{it} and n_t is the directing process.

If δ_i is i.i.d. with mean zero and variance σ^2, and n_t is sufficiently large, then $\varepsilon_t | n_t \sim N(0, \sigma^2 n_t)$. The normal law follows from the Central Limit Theorem (CLT). As Osborne (1959) notes, variation in n_t over time will lead to rejection of normality in the unconditional distribution even if the CLT applies.

GARCH may be explained as an embodiment of time dependence in the rate of evolution of intraday equilibrium returns. To make the argument clear, assume that the daily number of information arrivals is serially correlated, which can be reflected as follows:

$$n_t = k + b(L)n_{t-1} + u_t, \tag{5}$$

where k is a constant, $b(L)$ is a lag polynomial of order q, and u_t is white noise. Innovations to the mixing variable persist according to the autoregressive structure of $b(L)$. Define $\Omega_t = E(\varepsilon_t^2 | n_t)$. As noted above, if the mixture model is valid, then $\Omega_t = \sigma^2 n_t$. Substituting the moving average representation of (5) into this expression for variance yields

$$\Omega_t = k\sigma^2 b(L)\Omega_{t-1} + u_t \tag{6}$$

Equation (6) captures the type of persistence in conditional variance that can be picked up by estimating a GARCH model. In particular, innovations to the information process lead to momentum in the squared residuals of daily returns.

The focus of our empirical tests is on the variance of returns conditional on knowledge of the mixing variable. Because n_t is generally not observed, a proxy is required. We choose daily trading volume as a measure of the amount of daily information that flows into the market. Tauchen and Pitts model volume and price change as being a joint (random) function of information flow. If this specification is correct, our estimation is subject to an unquantified specification bias. Nevertheless, using volume as the mixing variable is consistent with the sequential information models of Copeland and others and the mixture of Epps and Epps. In general, despite the imprecise role of volume in financial research, volume is likely to contain information about the disequilibrium dynamics of asset markets.

The model to be estimated for each stock in the sample is given by equation (1) and the following generalized variance specification:

$$\varepsilon_t | (V_t, \varepsilon_{t-1}, \varepsilon_{t-2}, \ldots) \sim N(0, h_t) \quad (2')$$

$$h_t = \alpha_0 + \alpha_1 \varepsilon_{t-1} + \alpha_3 V_t \quad (3')$$

Under the assumption that volume (V_t) is the mixing variable, volume is weakly exogenous in the sense of Engle, Hendry, and Richard (1983). We

restrict our attention to a GARCH (1, 1) specification since it has been shown to be a parsimonious representation of conditional variance that adequately fits many economic time series. A succinct measure of the persistence of variance as measured by GARCH is the sum $(a_1 + a_2)$: as this sum approaches unity, the greater is the persistence of shocks to volatility.

The mixture model of the previous section predicts that $a_3 > 0$. Furthermore, in the presence of volume with $a_3 > 0$, a_1 and a_2 will be small and statistically insignificant if daily volume is serially correlated. In particular, the persistence of variance as measured by $(a_1 + a_2)$ should become negligible if accounting for the uneven flow of information explains the presence of GARCH in the data.

Data and Empirical Results

The data set comprises daily return and volume data for 10 actively traded stocks. Actively traded stocks are most likely to have a sufficiently large number of information arrivals per day to satisfy the conditions for the CLT. Our sample is chosen from a population of stocks for which trade on the MICEX.

Tables 1 and 2 represent coefficients for GARCH (1, 1) Model without Volume and for GARCH (1, 1) Model with Volume (t).

Table 1

Company	α	β	α + β
Gazprom	0,08991	0,88971	0,97962
Lukoil	0,066064	0,64617	0,712234
VTB	0,061955	0,89519	0,957145
NLMK	0,10014	0,85605	0,95619
Rostelekom	0,34188	0,55871	0,90059
Sberbank	0,079193	0,89255	0,971743
Nornikel	0,084061	0,88537	0,969431
Rosneft	0,091575	0,87338	0,964955
Poluszoloto	0,10406	0,83694	0,941
Aeroflot	0,061075	0,89811	0,959185

Table 2

Company	α	β	γ	α + β
Gazprom	0,037838	6,39E-08	0,00092865	0,037838064
Lukoil	0,12089	6,22E-06	0,00062099	0,120896221
VTB	0,075044	0,00546	0,0010676	0,080504

Company	α	β	γ	α + β
NLMK	0,094293	2,89E-06	0,0033571	0,09429589
Rostelekom	0,063108	0,00042375	0,026773	0,06353175
Sberbank	1,62E-05	2,31E-07	0,0013021	1,64105E-05
Nornikel	0,14795	1,73E-06	0,0011734	0,147951731
Rosneft	0,084349	9,75E-10	0,0012924	0,084349001
Poluszoloto	0,53592	0,094409	0,0009272	0,630329
Aeroflot	0,20997	0,079139	0,0023538	0,289109

The parameters are estimated jointly using numerical techniques to maximize the likelihood function. The parameter space of the variance equation is constrained to be nonnegative. Experimentation with various starting values for the parameters shows that global maxima are obtained in all models estimated. The table provides strong evidence that daily stock returns can be characterized by the GARCH model when volume is excluded from the variance equation. Coupled with the noted serial correlation in volume, this evidence provides prima facie support for the hypothesis that ARCH reflects an uneven but persistent flow of information to stock markets.

Our primary hypothesis is given strong support by the results from the unrestricted model: a_1 and a_2 generally become small and statistically insignificant when a_3 is unconstrained.

Conclusions

This item provides empirical support for the hypothesis that ARCH is a manifestation of the daily time dependence in the rate of data arrival to the market for individual stocks. Thereby, this form of heteroskedasticity is an artifact of the arbitrary, albeit natural, choice of observation rate. While this conclusion is strictly valid only for our sample of actively traded stocks, it is plausible to surmise that similar results would be found for other asset return series that can be explained by ARCH (e.g., foreign exchange rates), where in many instances more appropriate measures of information arrival time are not available. The results properly motivate the use of ARCH models to study the behavior of asset prices.

REFERENCES

1. *Baillie R. T., Bollerslev T.* The message in daily exchange rates : A conditional variance tale / J. of Business and Economic Statistics. 1989. Forthcoming.

2. *Bollerslev T.* Generalized autoregressive conditional heteroskedasticity / J. of Econometrics. 1986. 31, P. 307–327.
3. *Clark P. K.* A subordinated stochastic process model with finite variance for speculative prices / Econometrica. 1973. 41, P. 135–56.
4. *Copeland T. E.* A model of asset trading under the assumption of sequential information arrival / J. of Finance. 1976. 31, P. 1149–1168.

DYNAMICAL REGIMES IN SEMICONDUCTOR SUPERLATTICE

V. A. Maximenko

Saratov State University

INTRODUCTION

Superlattices (SLs), comprising alternating layers of different semiconductor materials, provide a flexible environment for studying quantum transport in periodic potentials and for generating, detecting, mixing and amplifying high-frequency electromagnetic radiation (Esaki, Tsu, 1970; Tsu, 2005; Wacker, 2002; Shik, 1975). It has been shown that a titled magnetic field applied to a SL can strongly affect and hence control the electrical properties of the structure. Recently, we have revealed that a tilted magnetic field applied to a SL in parallel with the external signal results in the complex dynamical regimes including ones being similar to dynamical chaos that makes possible the new applications requiring microwave GHz-THz chaotic signals. To confirm the presence of the dynamical chaos in SLs as well as to classify the observed regimes and estimate the stability of them the special methods must be used. The most appropriate method is the Lyapunov exponents calculation which is the powerful and useful tool for the complex system dynamics analysis. Unfortunately, the direct application of the Lyapunov exponent calculation technique developed for the system with the small number of degrees of freedom to the semiconductor superlattice, being the spatially extended system, is problematic. The main causes of this problem are the following: (i) the phase space of the system is infinite; (ii) the number of the Lyapunov exponents is also infinite; (iii) the system state must be used instead of the finite-dimensional vector; (iv) the orthogonalizaiton and normalization procedures must be modified to be applicable for the states. Although the scientists try to use the Lyapunov exponents for the spatially extended systems, all attempts are reduced generally to the application of the modifications of the standard methods developed for the finite-dimensional systems (e.g., the estimation of the highest Lyapunov exponent from time series or the representation of the spatially extended system as the finite-dimensional one with the high dimension by means of the discretization). Unfortunately, these approaches do not take into account the distinguishing characteristics of the spatially extended systems

and have serious limitations connected with the high dimension of the phase space of the discretized system.

Recently, the successful attempt to compute the highest Lyapunov exponent, taking into account the core features of the spatially extended systems, has been made (Filatov et al., 2006; Hramov et al., 2008). In the present work we develop the technique to calculate the spectrum of the Lyapunov exponents (Filatov et al., 2006; Hramov et al., 2008; Kusnetsov, Trubetskov, 2004) for the semiconductor superlattice. The structure of the article is the following. The general formalism concerning both the SL dynamics modeling and the spectrum of Lyapunov exponent calculation is given in Sec. I. in Sec. II the application of the proposed approach is considered as for the case of autonomous system as for the system driven by the external signal. The stability characteristics of the different dynamical regimes (synchronous, asynchronous and chaotic) of SL being under the external harmonic signal are also discussed in Sec. II. The final remarks are given in Conclusion.

I. GENERAL FORMALISM

The collective dynamics of electrons in the semiconductor superlattice (Greenaway et. al., 2009) is described by the dimensionless current continuity equation

$$\frac{\partial n}{\partial t} = -\beta \frac{\partial J}{\partial x} \tag{1}$$

and Poisson equation

$$\frac{\partial F}{\partial x} = v(n-1), \tag{2}$$

which should be solved selfconsistently. Here $n(x, t)$, $F(x, t)$, $J(x, t)$ are the dimensionless volume electron density, electric field and current density, x and t – the dimensionless coordinate and time, $v = 15.769$ – the dimensionless control parameter. The dimensionless variables are connected with the dimension [primed] ones as

$$x = x'/L', t = t'/\tau', n = n'/n'_D,$$

$$J = J'/(e\, n'_D \upsilon'_0), F = F'/F'_c, F'_c = \hbar/(e\, d'\tau'),\tag{3}$$

$$\beta = \upsilon'_0 \tau'/L', v = L'e\, n'_D/(F'_c \varepsilon_0 \varepsilon_r),$$

$$\upsilon'_0 = \delta\Delta' d'/(2\hbar).$$

where d' =8.3 nm and L' = 115.2 nm are the period and the length of the superlattice, Δ' = 19.1 meV is the miniband width, n'_D = 3×10^{22} m^{-3} – the n-type doping density in the SL layers, $e > 0$ – the electron charge,

63

F_c' = 3.1725×10⁵ V/m – normalization value of the electric field, ε_0 and ε_r = 12.5 are the absolute and relative permittivities, respectively. Parameters $\delta = \left[\tau_e'/\left(\tau_e' + \tau_i'\right)\right]^{1/2}$ and $\tau' = \delta\tau_i'$ characterize the scattering and depend on the elastic τ_e' and inelastic τ_i' scattering times. In our study we have used τ' = 250 fs, δ_i = 1/8.5. Here and hereafter the values of the dimension quantities are taken from the recent experiments (Fromhold et. al., 2004) have been used.

Within the drift-diffusion approximation the current density is

$$J = n\upsilon_d(F) + D(F)\frac{\partial n}{\partial x}, \qquad (4)$$

where $\upsilon_d(F)$ is the dimensionless electron drift velocity $\left(\upsilon_d = \upsilon_d'/\upsilon_0'\right)$ and $D(F)$ is the diffusion coefficient (Wacker, 2002).

$$D(F) = \upsilon_d(F)d\frac{\exp(-kF)}{1 - \exp(-kF)}, \qquad (5)$$

$$\kappa = \hbar/\left(k_B'T'\tau'\right), \; d = d'/L'$$

which may be neglected for the low temperatures T'. If there is no titled magnetic field applied to the superlattice, the drift velocity $\upsilon_d(F)$ is

$$\upsilon_d(F) = \frac{I_1(\Theta)}{I_0(\Theta)}\frac{F}{1 + F^2}, \qquad (6)$$

where $\Theta = \Delta'/\left(2k_B'T'\right)$, $I_{0,1}(x)$ are the modified Bessel functions of the first kind. In the case of the titled magnetic field the drift velocity $\upsilon_d(F)$ can be obtained numerically by using the approach described in (Greenaway et. al., 2009).

The dimensionless voltage $V = V'/\left(F_c'L'\right)$ applied to the superlattice is a global constraint given by

$$V = U + \int_0^1 Fdx, \qquad (7)$$

where the dimensionless voltage $V = V'/\left(F_c'L'\right)$ dropped across the contacts includes the effect of charge accumulation and depletion in the emitter and collector regions and a contact resistance. To determine the dimensionless current density in the heavily doped emitter contact with the electrical conductivity σ' = 3788 Sm⁻¹ we have used Ohmic boundary conditions

$$J(0,t) = sF(0,t), \qquad (8)$$

where $s = \sigma'F_c'/\left(en_D'\upsilon_0'\right)$ = 17.6511 is the dimensionless control parameter corresponding to the electrical conductivity of the emitter contact. The external

harmonic influence with the frequency $\omega_e = 2\pi f_e' \tau'$ has been introduced as $V = V_0 + \Delta V_0 \cos(\omega_e t)$.

In the numerical simulations we have used the discretized dimensionless current continuity

$$\Delta x \frac{\partial n}{\partial t} = \beta \left(J_{m-1} - J_m \right), \, m = 1, \ldots, N \tag{9}$$

and Poisson

$$F_{m+1} = v \left(n_m - 1 \right) + F_m, \, m = 1, \ldots, N \tag{10}$$

equations instead of Eqs. (1) and (2). The miniband transport region has been split into $N_L = 480$ layers, each of width $\Delta x = 1/N_L = 2.08 \times 10^{-3}$, which is small enough to approximate a continuum (Greenaway et. al., 2009, Greenaway et. al., 2010), time step value has been selected as $\Delta t = 5 \times 10^{-4}$. In the oscillating regimes, finding the drift velocity, we have used averaging the electric field F over the nearest neighborhood (i.e., $\upsilon_d = \upsilon_d(\bar{F})$) to avoid the nonphysical behavior (Greenaway et. al., 2009). All calculations have been made on the assumptions that the temperature is equal to zero (i.e., $T_0 = 0$ K).

The main idea of the computation of the spectrum of the Lyapunov exponents for the semiconductor superlattice is the following. The dimensionless volume electron density $n(x, t)$ determines identically the system state. The dimensionless electric field $F(x, t)$ and current density $J(x, t)$ are not sufficient for the state of SL, since for the fixed moment of time they could be explicitly defined through the volume electron density $n(x, t)$ by Poisson (2) equation, current density equation (4), drift velocity dependence (6) and boundary conditions (7), (8).

In other words, to explicitly define the superlattice system state it is sufficient to know only the volume electron density $n(x, t)$ of SL. It allows us to calculate the analogues states for the other moments of time.

The dimensionless volume electron density $n(x, t)$ plays the role of the reference state to study the evolution of the small perturbations. To compute N largest spatial Lyapunov exponents we consider the set of perturbations $\tilde{n}_i(x, t)$, $i = 1, \ldots, N$ which are initially orthogonal

$$\left(\tilde{n}_i(x, 0), \tilde{n}_j(x, 0) \right) = \begin{cases} 1, \, i = j \\ 0, \, i = j \end{cases} \tag{11}$$

where $\left(\tilde{n}_i, \tilde{n}_j \right)$ is the scalar product

$$\left(\tilde{n}_i, \tilde{n}_j \right) = \int_0^L n_i n_j \, dx. \tag{12}$$

Additionally to the orthogonality requirement (11) all perturbations $\tilde{n}_i(x, t)$ must also satisfy the normalization condition

$$\left\| \tilde{n}_i(x,0) \right\| = 1, \tag{13}$$

where $\left\| \tilde{n}_i \right\| = \sqrt{\left(\tilde{n}_i, \tilde{n}_j \right)}$.

The set of the perturbations $\tilde{n}_i(x,t)$ fulfilling requirements (11) and (13) may be obtained with the help of the Gramm-Schmidt method

$$\begin{cases} \tilde{n}_i(x,0) = \dfrac{\tilde{n}_i(x,0)}{\left\| \tilde{n}_i(x,0) \right\|} \\ \tilde{n}_1(x,0) = \varphi_1(x) \\ \tilde{n}_{i+1}(x,0) = \varphi_{i+1}(x) - \sum_{k=1}^{i} \left(\tilde{n}_k(x,0), \varphi_{i+1} \right) \tilde{n}_{i+1}(x,0) \end{cases}, \tag{14}$$

$i = 1, 2, \ldots, N - 1$, where $\varphi_1(x), \varphi_2(x), \varphi_N(x)$ is the set of the linearly independent arbitrary functions defined for the system under study.

To compute the spectrum of the Lyapunov exponents of the superlattice, the behavior both of the volume electron density $n(x, t)$ and all perturbations $\tilde{n}_i(x,t)$ ($i = 1, 2, \ldots, N - 1$) has to be considered. The evolution of $n(x, t)$ is defined by Eqs. (1), (2), (4), (6) and boundary conditions (7), (8), whereas the development of the perturbations $\tilde{n}_i(x,t)$ of the reference state is determined by the linearization

$$\frac{\partial \tilde{n}_i}{\partial t} = -\beta \frac{\partial \tilde{J}_i}{\partial x},$$

$$\frac{\partial \tilde{F}_i}{\partial x} = v(\tilde{n}_i),$$

$$\tilde{J}_i = \tilde{n}_i \upsilon_d(F) + n \frac{d\upsilon_d(F)}{dF} F_i' \tag{15}$$

$$\tilde{U}_i + \int_0^1 \tilde{F}_i dx = 0,$$

$$\tilde{J}_i(0,t) = s\tilde{F}_i(0,t)$$

of these equations applied in the vicinity of the reference state. After the time interval with the length T, the obtained set of the perturbations $\tilde{n}_i(x,t)$, must be orthogonalized and normalized with the help of Gramm-Shmidt method again, with the set of the functions $\varphi_i(x)$, represented by the perturbations $\tilde{n}_i(x,t)$. In other words,

$$\varphi_i(x) = \tilde{n}_i(x,T). \tag{16}$$

The described algorithm must be repeated many times. After *M* iterations the Lyapunov sums are calculated

$$S_i = \sum_{j=1}^{M} \ln \left\| \tilde{n}_i \left(x, \, jT \right) \right\|, \tag{17}$$

where the perturbations before renormalization but after orthogonalizaiton are used. Finally, the Lyapunov exponents may be found as

$$\Lambda_i = \frac{S_i}{MT}. \tag{18}$$

II. DIFFERENT DYNAMICAL REGIMES AND THEIR STABILITY

Having applied the proposed approach, we start discussing the results obtained by the numerical simulation. First of all, we consider the autonomous dynamics of SL without the titled magnetic field to give the direct correspondence between numerical values of Lyapunov exponents and the system behavior. The dependencies of the five highest Lyapunov exponents Λ_i obtained numerically for the autonomous superlattice without the titled magnetic field are shown in Fig. 1 both in the dimension $\left(\Lambda' = \Lambda / \tau' \right)$ and dimensionless scales.

One can see that the largest Lyapunov exponent grows to zero at $V_{th} \approx 9.5768$ ($V'_{th} \approx 360$ mV) where the stationary state becomes unstable and for $V > V_{th}$ the superlattice demonstrates the periodic oscillations. Correspondingly, for $V > V_{th}$, the largest Lyapunov exponent Λ_1 is equal to zero (it corresponds to the perturbation along the time axis $\tilde{n}_i \left(x, t \right) \sim dn \left(x, t \right) / dt$, whereas all other exponents Λ_i, $i \geq 2$ are negative. Below the threshold value V_{th}, in turn, all Lyapunov exponents are negative. In the frame in Fig. 1 the neighborhood of the bifurcation point is shown in detail.
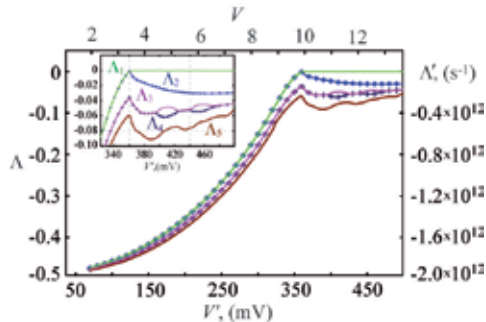
Fig. 1. (Color online) The dependencies of the five highest Lyapunov exponents on the applied voltage for the autonomous dynamics of SL without the titled magnetic field. The axes are shown both in the dimension and dimensionless scales

So, the calculation of LEs is proven to be effective and powerful tool for the analysis of the behavior of the semiconductor superlattice that gives correct and accurate results. Therefore, we can apply it to detect and distinguish the complex regimes observed in the semiconductor superlattice driven by the external harmonic signal in a tilted magnetic field. The time series for two different regimes observed in the superlattice are shown in Fig. 2, a, b. The parameters of the external titled magnetic field B = $(B \cos \theta, 0, B \sin \theta)^T$ have been selected as $B = 12$ T, $\theta = 40^\circ$. For the convenience, the values of time and current are shown in the dimension units. In our numerical simulations we calculate the current as

$$I'(t') = \frac{A' e n'_D \upsilon'_0}{N+1} \sum_{m=0}^{N} J_m \ , (19)$$

where $A' = 5 \times 10^{-10}$ m^2 is the cross-sectional area of the superlattice (Wacker, 2002; Greenaway et. al., 2009; Fromhold et. al., 2004), $t' = t\tau'$. The projects of the attractors (Fig. 2, c, d) corresponding to these regimes are shown in the phase space reconstructed with the help of the delay-coordinate embedding method (Tackens, 1981). One can see that the current oscillations are irregular in both regimes, but, as it follows from analysis of the Lyapunov exponents, these regimes are qualitatively different. For the case of the system under external force, the spectrum of conditional Les (CLEs) has been calculated using the proposed technique.

In Fig. 2, e the dependencies of the highest conditional LE Λ_1 on the time of calculation are shown for the regimes illustrated in Fig. 2, a, c and Fig. 2, b, d. According to this dependencies, the first regime (Fig. 2, a, c) obtained for $V_0 = 16.691$, $\Delta V_0 = 2.736$, $\omega_e = 3.691 \times 10^{-2}$ ($V'_0 = 610$ mV, $\Delta V'_0 = 100$ mV, $f''_e = 23.5$ GHz) should be considered as the quasiperiodic oscillations, since the largest conditional exponent corresponding to it is equal to zero. In comparison, in the same Fig. 2, e the largest conditional Lyapunov exponent corresponding to the synchronous periodic regime is shown ($V_0 = 16.691$, $\Delta V_0 = 2.736$, $\omega_e = 3.299 \times 10^{-2}$ ($V'_0 = 610$ mV, $\Delta V'_0 = 100$ mV, $f''_e = 21.0$ GHz)) where this CLE is negative. Alternatively, the second regime (Fig. 2, b, d) observed for $V_0 = 16.691$, $\Delta V_0 = 2.736$, $\omega_e = 2.906 \times 10^{-2}$ ($V'_0 = 610$ mV, $\Delta V'_0 = 100$ mV, $f''_e = 18.5$ GHz) corresponds to the dynamical chaos, due to the positive value of the largest CLE Λ_1.

III. CONCLUSIONS

In the present work the method for the calculation of the spectrum of the Lyapunov exponents for the semiconductor superlattices being spatially extended system has been proposed. We have found an excellent agreement between the SL dynamics and the behavior of the spectrum of LEs in the case
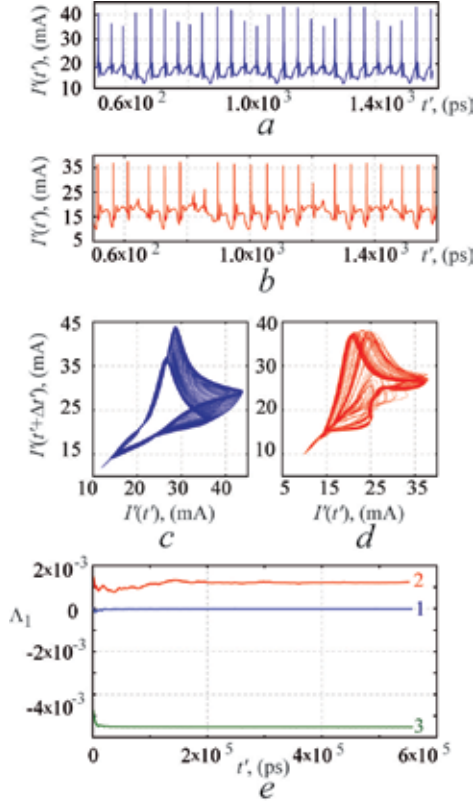
Fig. 2. (Color online) The time series corresponding to the (*a*) quasi-periodic and (*b*) chaotic oscillations; (*c*, *d*) corresponding to these time series projects of the attractors in the reconstructed phase space; (*e*) the dependencies of the highest conditional LE Λ_1 on the time of calculation obtained for quasi-periodic (curve 1), chaotic (curve 2) and synchronous periodic (curve 3) regimes

of autonomous system. Having applied the developed technique to the complex regime observed in SL driven by the external harmonic signal in the titled magnetic field, we have conclusively proven the presence of the dynamical chaos in such a kind of the semiconductor systems that gives the strong potential for new applications requiring microwave GHz-THz chaotic signals. So, the Lyapunov exponents could be effectively applied for the detection and classification of the dynamical regimes being realized in the semiconductor superlattices. However, the field of the possible applications of the spectrum of the Lyapunov exponents is not restricted to the consideration of autonomous SLs. In particular, Lyapunov exponents are an effective tool for the analysis of

the different types of chaotic synchronization, observed both in the finite- and infinite-dimensional systems (Pyragas, 1997; Hramov et. al., 2005; Hramov et. al., 2008) that, together with the revealed possibility of the existence of the chaotic regimes in the semiconductor superlattices, gives the strong potential of the use of the LE technique in further studies.

Acknowledgments

REFERENCES:

Esaki L., Tsu R. Superlattice and Negative Differential Conductivity in Semiconductors // IBM J. of Research and Development. 1970. Vol. 14, № 1. P. 61–65.

Filatov R. A. Hramov A. E. and Koronovskii A. A. Chaotic synchronization in coupled spatially extended beam-plasma systems // Phys. Lett A. 2006. Vol. 358. № 4. P. 301–308.

Fromhold T. M., Patane A., Bujkiewicz S., Wilkinson P. B., Fowler D., Sherwood D., Stapleton S. P., Krokhin A. A., Eaves L., Henini M. et al. Chaotic electron diffusion through stochastic webs enhances current flow in superlattices // Nature. 2004. Vol. 428. P. 726–730.

Greenaway M. T., Balanov A. G., SchÄoll E., Fromhold T. M. Controlling and enhancing terahertz collective electron dynamics in superlattices by chaos-assisted miniband transport // Phys. Rev. B. 2009. Vol. 80, № 20. P. 205318.

Greenaway M. T., Balanov A. G., Fowler D., Kent A. J., Fromhold T. M. Using. acoustic waves to induce high-frequency current oscillations in superlattices // Phys. Rev. B. 2010. Vol. 81. № 23. P. 235313.

Hramov A. E., Koronovskii A. A., Moskalenko O. I. Generalized synchronization onset // Europhysics Letters. 2005. Vol. 72. № 6. P. 901–907.

Hramov A. E., Koronovskii A. A., Popov P. V. Incomplete noise-induced synchronization of spatially extended systems // Phys. Rev. E 2008.Vol. 77. № 3. P. 036215.

Hramov A. E., Koronovskii A. A., Kurovskaya M. K. Zero Lyapunov exponent in the vicinity of the saddle-node bifurcation point in the presence of noise // Phys. Rev. E. 2008. Vol. 78. № 3. P. 036212.

Kuznetsov S. P., Trubetskov D. I. Chaos and hyperchaos in a backward-wave oscillator // Radiophysics and Quantum Electronics. 2004. Vol. 47. P. 341–355.

Pyragas K. Conditional Lyapunov Exponents From Time Series // Phys. Rev. E. 1997. Vol. 56. № 5. P. 5183–5188.

Shik A. Y. Superlattices-periodic semiconductor structures // Sov. Phys. Semicond. 1975. № 8. P. 1195–1209.

Takens F. in Lectures Notes in Mathematics. N. Y. : SpringlerVerlag, 1981. P. 366.

Tsu R. Superlattices to Nanoelectronics. Elsevier, 2005. P. 300.

Wacker A. Semiconductor Superlattices : A model system for nonlinear transport // Physics Reports. 2002. Vol. 357. P. 1–111.

LOCAL MODIFICATIONS OF OPTICAL GLASS BY HIGH-INTENSITY ULTRASHORT LASER PULSES

A. V. Melnikov, E. A. Romanova

Saratov State University

1. INTRODUCTION

Nonlinear coefficients of refraction and absorption are, in general, functions of electromagnetic wavelength, as well as their linear analogs. Dispersion properties of the nonlinear coefficients are important in operation of all nonlinear devices. In glasses, nonlinear coefficients are totally dominated by nonlinear electronic excitations. Dispersion of nonlinear coefficients in dielectrics was considered within two theoretical approaches: model of anharmonic oscillator [1] and Kramers-Kronig transformation [2]. The latter approach has been developed for crystal semiconductors and was justified experimentally, but measurements performed recently for amorphous semiconductors (optical glasses) [3, 4] demonstrated significant near the bandgap frequencies.

The part of nonlinear coefficients in the process of energy deposition into a glass sample was studied in [5] within a numerical model. These results demonstrated that the droplet-like volume heated by a focused femtosecond (fs) pulse above the glass transition temperature had a long length in glasses having large Kerr coreefficient, but this length became shorter in the presence of strong multi-photon absorption. A focusing lens with large focal distance provided longer structures in glasses with large Kerr coefficients. It was also found that the lens with short focal distance gave very low-width droplets if the nonlinear absorption was strong enough. Finally, it was demonstrated that a significant decrease of the droplet dimensions could be achieved with focusing by a long focal distance lens when the Kerr coefficient was small but multi-photon absorption was very strong.

In this paper, we propose an analytical approach based on approximate methods to analyze the process of the ultra-short pulse energy deposition into a glass sample with account of dispersion of nonlinear coefficients. The approach is similar to the one described in [6], but in addition to nonlinear absorption of a non-stationary converging Gaussian beam we take into account effect of the beam self-focusing in a glass medium. Nonlinear absorption of a non-stationary quasi-plane Gaussian beam focused into a medium with large Kerr coefficient is also studied at different peak wavelengths. Material parameters of chalcogenide glass (As_2Se_3) are used in numerical modeling.

2. ENERGY DEPOSITION

2.1. Non-linear absorption accompanied by self-focusing effect

An approximate analytical solution of the equation for the slowly varying amplitude of the scalar electrical field $E(r, z) = \bar{F}(r, z) \exp(i\beta z)$:

$$\left(2ik\frac{\partial}{\partial z}+\nabla_\perp^2+\chi\right)F(r,z)=0,\tag{1}$$

where $\chi=2k^2n_0n_2I$ (k is the wavenumber, n_0 is the linear refractive index, n_2 is Kerr coefficient, I is light intensity) can be obtained by using the modified generalized method of moments [7]. For $F(r,z)=A(z)\exp(-p(z)r^2/2)$ with $p(z)=\eta(z)+i\xi(z)$, Equation (1) can be transformed into the system of differential equations:

$$\dot\eta=2\eta\xi$$
$$\dot\xi=\xi^2-\eta^2(1-q)\tag{2}$$
$$2\dot A/A=\dot\eta/\eta$$

where the nonlinear parameter $q=k^2n_2P/2$ depends on the beam power $P=|A|^2/2\eta=$ const. Parameters η and ξ are related to the beam radius $w(z)$ and the beam curvature radius $R(z)$ as follows: $\eta(z)=1/w^2(z)$, $\xi(z)=\pi/\lambda R(z)$. Initial conditions $\xi(-R)=\xi_0$, $\eta(-R)=\eta_0$ corresponding to a converging light beam (as depicted in Fig. 1, a) are applied. Intensity dependence of a highly non-linear absorption is approximated by a step function with the threshold I_h. The total absorbed energy is evaluated under an assumption (similar to [6]) that the pulse reaches its waist plane unabsorbed and is finally absorbed there.

Under this approximation, the total energy absorbed

$$E_A=E_0\left\{erf\left(\sqrt{\ln\frac{I_{bw}}{I_h}}\right)-\frac{2I_h}{\sqrt\pi I_{bw}}\left(1+\frac{2}{3}\ln\frac{I_{bw}}{I_h}\right)\sqrt{\ln\frac{I_{bw}}{I_h}}\right\}\tag{3}$$

depends on the initial pulse energy $E_0=\pi^{3/2}\omega_0^2\tau_0I_0$ (τ_0 is the pulse duration, w_0 is the initial beam radius, I_0 is the initial peak intensity) and on the ratio of the peak intensity at the beam waist I_{bw} to the threshold value I_h.

a　　　　　　　b
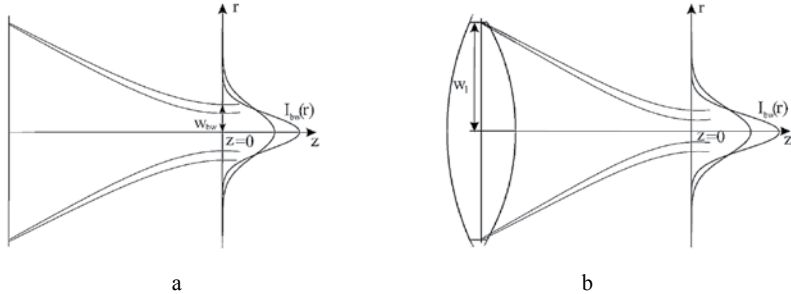
Figure 1

First, we consider the Gaussian beam is converging from infinity ($R\to\infty$) to its waist plane ($w_{bw}=w_{bw}{}^0$, $I=I_{bw}{}^0$) in a uniform medium when $n_2=0$. Solution of equations (2) gives that in presence of the Kerr nonlinearity, the beam

waist radius decreases due to self-focusing so that $w_{bw} = w_{bw}{}^0(1-q)^{1/2}$. The peak intensity increases, correspondingly, $I_{bw} = I_{bw}{}^0/(1-q)$. The total absorbed energy can be plotted (Fig. 2) depending on the n_2 and $\beta^{(2)}$ values, where $\beta^{(2)}$ is the two-photon absorption coefficient defined as follows: $\beta^{(2)} = \text{const} / I_h$. Here const corresponds to some threshold level of absorption.

Second, the quasi-plane Gaussian beam with the initial radius w_1 is focused by a lens with focal distance f into a glass sample (Fig. 1, b). Solution of equations (2) with the initial conditions $\xi(0) = -\pi/\lambda f$, $\eta(0) = \eta_1$ gives the beam waist radius equal to

$$w_{bw}^{f} = w_1 \sqrt{\frac{f^2}{z_{0q}^2}} \Big/ \sqrt{1 + \frac{f^2}{z_{0q}^2}}, \tag{4}$$

where $z_{0q} = w_1^2\pi/\lambda/(1-q)^{1/2}$. Absorbed energy can be evaluated from equation (3).
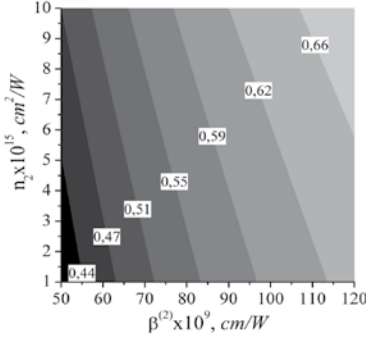
Figure 2. Absorbed energy (nJ) depending on the nonlinear coefficients. $E_0 = 1nJ$, $\lambda = 1\mu$, $\tau = 40fs$, $w_{bw}{}^0 = 6\mu$
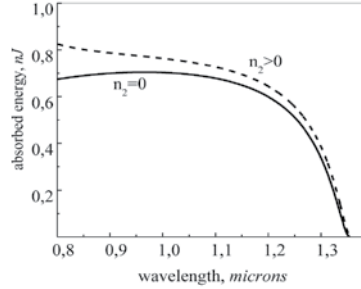
Figure 3. Absorbed energy depending on the peak pulse wavelength. $E_0 = 1nJ$, $\tau = 40fs$, $w_{bw}{}^0 = 6\,\mu$

As a theoretical approach to describe dispersion in optical glasses near the bandgap frequency is not available now, in estimates of the n_2 dispersion:

$$n_2(\lambda) = n_2 \Big/ \left(1 - \left(\hbar^2 4\pi^2 c^2 / \left(\lambda^2 E_s^2\right)\right)\right)^{3.5} \tag{5}$$

we use the model of anharmonic oscillator [1] that is valid far from the glass bandgap frequency. For the two-photon absorption coefficient, we have used the following approximate expression:

$$\beta^{(2)}(\lambda) = \frac{2^9 \pi}{5} \frac{e^4}{\sqrt{m_0} c^2} \frac{\sqrt{E_p}}{n_0^2 E_g} \frac{\left(4\pi c/\lambda - 1\right)^{3/2}}{\left(4\pi c/\lambda\right)^5}. \tag{6}$$

In equations (5), (6) E_g is optical bandgap energy ($E_g = 2eV$ for As_2Se_3 glass composition), $E_S = 2.5 \cdot E_g$, $E_p = 21eV$. In Fig. 3, the total absorbed energy depending on the pulse peak wavelength is shown.

2.2. Spatial distribution of the absorbed energy

In accordance with the results of p.2.1 we assume (similar to [6]) that the topped Gaussian pulse has the following intensity distribution:

$$I(z,r,t) = \frac{I_{bw}}{1 + z^2/z_{0q}^2} \exp\left(-\frac{r^2}{\omega_{bw}^2(1+z^2/z_{0q}^2)}\right) \exp\left(-\frac{t^2}{\tau_0^2}\right) \quad (7)$$

In the first case of converging Gaussian beam $z_{0q} = (1-q)^{1/2} w_{bw}^2 \pi/\lambda$. If the beam is focused by the lens, $w_{bw} = w_{bw}^f$, $z_{0q} = (w_{bw}^f)^2 \pi/\lambda$. The coordinate system is used with $z = 0$ at the beam waist, as shown in Fig. 1.

Finally, the spatial distribution of the absorbed energy density can be calculated as follows:

$$N(z,r) = \frac{-4 I_{b} \tau_0 z}{z_{0q}^2 + z^2} \sqrt{\ln\left(\frac{I_{0q}}{I_{b}\left(1+\frac{z^2}{z_{0q}^2}\right)}\right) - \frac{r^2}{\omega_{bw}^2\left(1+\frac{z^2}{z_{0q}^2}\right)}} \quad (8)$$

Absorbed energy density is shown in Fig.4 and Fig.5.

(a)   (b)
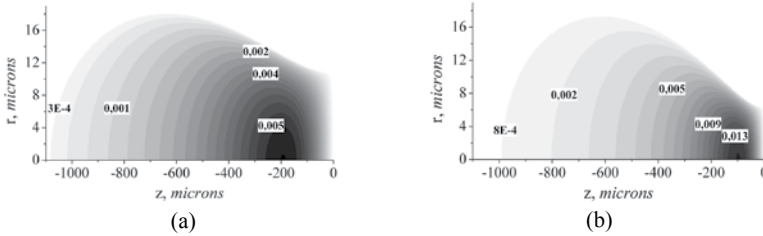
Figure 4. Spatial distribution of the absorbed energy density (J/cm^3). Converging Gaussian beam (Fig.1a) *(a)* $n_2 = 0$, *(b)* $n_2 = 10^{-14}$W/cm^2. $\beta^{(2)} = 100$ cm/GW

(a)   (b)
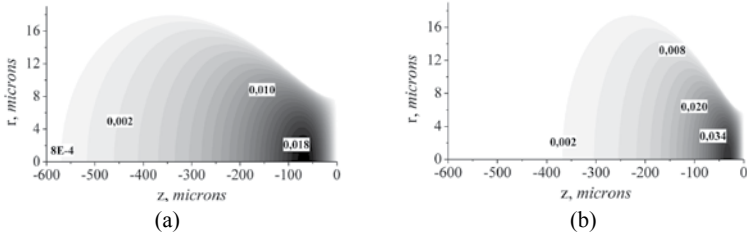
Figure 5. Spatial distribution of the absorbed energy density (J/cm^3). Focused Gaussian beam (Fig.1b) *(a)* $n_2 = 0$, *(b)* $n_2 = 10^{-14}$W/cm^2. $\beta^{(2)} = 100$ cm/GW

3. CONCLUSIONS

Approximate expressions that can be used for analysis of the process of the ultrashort pulse energy deposition into a glass sample have been derived. The developed analytical model provides a simple way to understand the part of nonlinear coefficient of refraction and absorption, as well as irradiation conditions (non-stationary beam focusing by a lens) in the glass sample heating.

As permanent change of refractive index is associated with heating of the glass sample up to the glass transition temperature T_g due to the energy deposition by a high intensity pulse [5], the results of this paper give a simple way to evaluate dimensions of the regions heated above T_g versus values of the nonlinear coefficients and finally depending on the peak wavelength of the irradiating pulse.

The results are directly related to optimisation of the technology of optical glass processing by ultrashort pulses, in particular identification of the spectral range of irradiating laser.

REFERENCES

1. *Lines M. E.* Oxide glasses for fast photonic switching: a comparative study / J. of Applied Phys. 1991. Vol. 69, P. 6876–6884.
2. *Sheik-Bahae M., Stryland van E. W., Hagan D. J., Hutchings D. C.* Dispersion of Bound Electronic Nonlinear Refraction in Solids, IEEE / J. of Quantum Electron. 1991. Vol. 27, № 6.
3. *Romanova E., Afanasiev A., Shiryaev V., Snopatin G., Furniss D., Seddon A., Benson T., Derkowska B., Guizard S., Fedorov N.* Experimental Studies of Non-Linear Properties of Chalcogenide Glasses, in Proc.of : 11-th International Conference on Transparent Optical Networks (ICTON), Azores, Portugal, June 28–July 2, 2009.
4. *Tanaka K.* Nonlinear optics in glasses : How can we analyze? / J. of Physics and Chemistry of Solids. 2007. Vol. 68, P. 896–900.
5. *Romanova E. A. et al.* Propagation of optical pulses through nonlinear planar waveguides with junctions, in Frontiers in Planar Lightwave Circuit Technology / S. Janz et al., ed., Amsterdam : Springer, 2006.
6. *Rayner D. M. et al.* Ultrashort pulse non-linear optical absorption in transparent media / Opt. Express. May. 2005.Vol. 13, P. 3208–3217.
7. *Derbov V. L., Melnikov L. A., Novikov A. D.* New method for the solution of the problems of self-action of light beams and its application to the analysis of saturated absorption resonances shift / Kvantovaya Electron. (Moscow). 1971. 14, 2529.

STUDY OF CORRELATIONS BETWEEN MUSICAL PREFERENCES AND THE INDIVIDUAL PSYCHOLOGICAL FEATURES OF A PERSON

L. I. Mihnyuk

Saratov State University

Individual psychological features of a listener, the subject of a particular musical preferences, were individually emphasized in this paper as the subject of research among the reasons for certain musical preferences (fashion, Immediate social surroundings, education, upbringing, etc.).

Music perception is highly specific in comparison with some other objects. B. M. Teplov emphasized the role of emotions in this process. Moreover,

he believed that music perception occurs trough emotions [3]. U. B. Hyper-nreiter has established the role of internal singing in the process of music perception.

It can be assumed that on the cognitive level the appearance of prefer-ences as a consequences of a music evaluation as pleasant or unpleasant occurs trough the coincidence of several themes expressed by means of music with those contained in the musical composition, which turn the music from in-comprehensible into comprehensible. It is well known unconceivable to cause negative feelings in an individual rather than positive ones as compared to something he or can understand. According to J. Harris, the emotion expressed through music always connected with certain idea, and that the emotion itself brings certain state of mind. Based on natural internal resemblance, certain ideas give rise to particular emotional states which in turn provide the way for respective ideas to appear. It has to be noted that the idea of similarity as the basis for preferences to appear is not complain. The phrase belongs to Aristotle «like tends to like». [4]

Setting the goal of empirical research to establish correlation between musical preferences and the psychological features of an individual dictates certain limits in identifying the independed variable.

There exists a certain musical piece and genre to which it can be attrib-uted. It is known that each music genre has it fans attracted by this particular rhythm, tune, content, emotional and meaning characteristic of this particular kind of music, and not any other kind. At the same time, not all the pieces within the same genre preferable, although they demonstrate characteristics typical of this genre. Music genre as it is, accumulates certain meaningful fea-tures particular to it, which determines its choice as an independent variable subject to research.

The following served as the basic assumption for the research conducted within the framework of the problem under consideration: musical preferences are determined by the mutual correspondence between the character (model) of a genre and a the specific psychological features of a person.

During the initial stages of the research, a hypothesis of correlation be-tween musical preferences and overall specific personal psychological motor features was formulated.

It should also be emphasized that when obtaining positive results and confirming this hypothesis, one figures he/she has the opportunity to use the obtained data as diagnostic criteria as well as for professional recruitment pro-cess for a variety of technical occupations where precise motor coordination is required.

Certain correlation between motor skills make up and personality served as the foundation for this hypothesis. Thus, according to A. N. Rose, «motor skills make up of person, his/her speech and behavior, as well as his or her activities reflect his or her overall individual pattern as a personality taking into consideration the whole unequalled uniqueness of the human being».[1]

The target of this research is to identify the correlation between a person's particular features, the level of his/her psycho-motor development and his or her musical preferences.

72 subjects took part in this research. All of were students and young people with either complete or incomplete university education. According to the results of the interview, subjects of the research were broken up into 3 big groups. 1) pop 2) rock 3) New Age, jazz, classical and folk music, mantra. The subdivision is dictated by the extent of musical balance, tunefulness, level of professional performance and characteristics of sounds that make it up (see K. Korotkov, A. Tomatis). Ninety percent of the interviewed subjects pointed out that their musical preferences were formed before their teenage years were over, which testifys to the in-depth character o their attitude.

All the interviewed subjects to the research, upon obtaining their consent, passed the tests using SMIL (L. N. Sobchik) as well as psycho-motor tests developed by A. F. Panteleev «rods». Psycho-motor test are made up of ten increasingly complicated tasks of complicated tasks and the amount of time to complete then serve as the criteria for their performance. As a result of the research, it was found that the respondents from the first group were characterized with low anxiety levels and friendliness, they are emotional and when under stress may show hidden activity, but stand their ground fairly firmly throughout their lives. For the respondents from the second group, especially young males, introversion is far more typical, especially as compared to the members of the first group. They tend to be more inclined for reflections and irritability, have fairly high self esteem, but lack in express motivation for success. More frequently, motivation to avoid failure is present in such individuals. They are more feminine in character. On the whole, they are characterized with high emotions which, however, are not spontaneous in character. Young females from this group have high self esteem, frequently in excess of their actual abilities, light-mindedness when taking certain decisions and confidence of their future happiness. This combines with certain aggressive attitude towards the surrounding world, which may be spontaneous in character. The anxiety level is higher than in the females from the previous group. The respondents from the third group more frequently have a positive view of life and are more rational at assessing their potential. They are better motivated and express their concerns and ideas more openly. On the whole, фthey tend to be extravert, but are also inclined to get deep into their inner world. They are well aware of their problems, and they have a high level of perception of their surroundings. They may neglect their own interests in favor of social values.[1]

According to the data provided by the psycho-motor test, the last group was the best at coping with the task of psycho-motor test. The first group holds the second place, and the second group holds the third place. General correlations between personality balance and success in resolving psycho-motor tasks have been found. It takes shorter time for well balanced persons to complete the test. The overall schedule of test results is characterized by stability. Per-

sonal misbalance is frequently connected with fairly abrupt express fluctuations in timing of performance on the psycho-motor tasks, whereas resolving the most difficult task of the test rarely occurs in such respondents. As a result of the conducted research, the obtained data supported the initial suggestion of the research as to the existence of certain correlation between musical preferences, particular individual features and psycho-motor characteristics.

The obtained results have already served as a starting point for further research and opened the opportunity for the use of the new methods when conducting recruitment for certain occupations.

REFERENCES

1. *Розе Н. А. Психомоторика взрослого* человека. СПб. : Изд-во Ленингр. ун-та, 1970.
2. *Собчик Л. Н. СМИЛ Стандартизированный* многофакторный метод исследования личности. СПб. : Речь, 2009. 224 с.
3. *Теплов Б. М. Психология музыкальных* способностей. М., 1965. С. 254.
4. *Шестаков В. П. От этоса* к аффекту. М., 1975. С. 243.

FORMATION OF SILICON STRUCTURES WITH RECTIFYING PROPERTIES BY MAGNETRON SPUTTERING

D. M. Mitin, A. A. Serdobintsev

Saratov State University

Now scientific and technical progress is inconceivable without electronics. Intensive development of electronics is connected with the appearance of new various semiconductor devices and integrated microcircuits which find wide application in IT equipment, cosmonautics, automatics, radio engineering and television, measuring techniques, medicine, biology etc.

It is impossible to present modern science and technique without semiconductor devices. Computers and mobile phones, cameras and camcorders, lasers and solar batteries are only a 100-th part of possible applications of semiconductor devices.

It is commonly known that the basis of many semiconductor devices is p-n-junction around which an electric field arises preventing the electrons from passing from n- to p-area, and the holes – backwards that provides it with rectifying properties [1]. The property of p-n-junction to rectify a signal is used in various semiconductor devices such as diodes, transistors, variable capacitance diodes, photodiodes etc. This property is used for rectifying and conversion of electric signals of high frequency for amplification, detection and generation of electromagnetic waves etc. Thus, examination of properties and principles of p-n-junction's operation is the important task and develop-

ment of new methods of obtaining of p-n-junctions is actual and perspective direction of modern science.

The structures considered in given paper are obtained by magnetron sputtering on a DC. This method differs from a widely applied method of synthesis in high-frequency magnetron discharge in such a way that it allows us to obtain dense films with good adhesion and controlled properties [2]. Besides the method of magnetron sputtering is much cheaper and technological than the epitaxial method of film obtaining.

The possibility of creation of the structure with rectifying properties by magnetron sputtering on a DC was studied in this paper. A silicon film was deposited on a substrate from single-crystal silicon of n-type (doped by phosphorus) with a resistivity 0,008–0,012 Ohm·cm, 200 microns thick and 30 mm in diameter. The parameters of the process of film synthesis are current of magnetron system – 100 mA, pressure in a vacuum chamber – $4 \cdot 10^{-4}$ Torr, time of sputtering of a film – 15 minutes. The sputtering of ohmic contacts to investigated structure for determination of its electrophysical properties was the next stage of the work. Contacts were also received using the method of magnetron sputtering. Nickel was used as a material for contacts. The choice of nickel as a material for contacts is caused by good nickel to silicon adhesion. In turn, high adhesion allows us to make the soldering of wires to the obtained contacts with the help of an ordinary soldering iron without using difficult processing methods (for example a thermal-compression bonding).

Contacts were deposited on a surface of a magnetron sputtered silicon film and on a single-crystal substrate. At such a configuration of contacts current flow was provided across the silicon film.

Obtaining of i-v curve of the structure under consideration became the further stage of work. The voltage to the structure was applied by soldering of wires to nickel contacts. The i-v curve of the obtained structure is demonstrated in fig. 1. As one can see from the picture, the graph of received i-v curve is similar to the classical graph for p-n-junction (diode). Thus it is possible to make a conclusion that during the performed operation we received the rectifying junction due to the presence of a film on a surface of a single-crystal substrate.

Differential resistance of rectifying junction was calculated by means of obtained i-v curve. Differential resistance on a forward branch of i-v curve made about 200 Ohm.

Also the built-in potential φ_c was defined. The built-in potential was defined in this way – it is a straight line prolonging the almost linear section of the positive branch of i-v curve which intersects a voltage axis in a point $V = \varphi_c$. In our case the built-in potential φ_c is equal 1,56 V.

Investigation of structure sensitivity to visible light became the following stage of this work. Reverse branches of the i-v curve in the dark and under illumination by the incandescent lamp by capacity of 75 W are presented in fig. 2. As we can see from the picture, the structure possesses the pronounced

sensitivity to illumination that testifies the availability of these structures for creation of detectors and converters of visible light, including solar batteries on their basis.
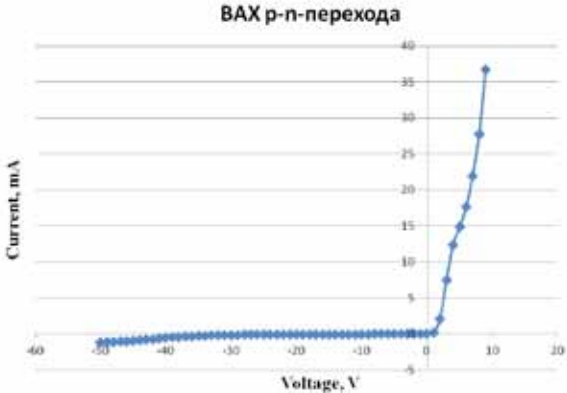

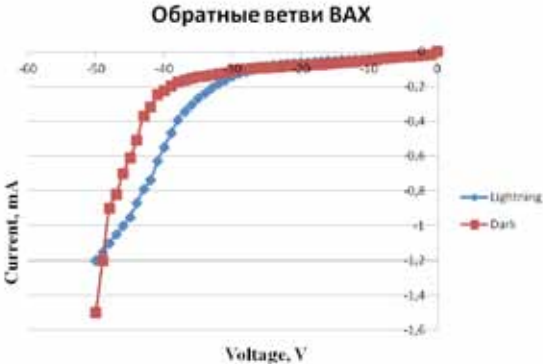Fig. 1. i-v curve of structure film-substrate

Fig. 2. Reverse branches of i-v curve at lighting and absence of lighting

Also the obtained structure was explored in a mode of the junction field effect transistor. The conducted measurements showed that the conductivity of the channel changes with the application of various voltages on gate electrode. This fact gives the opportunities for application of the obtained structure as the field effect transistor and a CCD matrix element.

Thus, in the course of this work rectifying junction based on structure of a single-crystal silicon substrate – silicon film was obtained. A feature of this structure is that the silicon was deposited by magnetron sputtering on a DC. The i-v curve was measured and investigated, such characteristics as dif-

ferential resistance and a built-in potential are defined, sensitivity of the received structure to illumination is shown. The important result is received by operation of researched structure in a mode of the field effect transistor is that conductivity of the channel changes with the application of various voltages on gate electrode. This fact gives new opportunities for application of obtained structure.

The important fact is that the used technology of obtaining of films allows us to create not only rectifying junctions, but also laboratory models of various devices. In the long term – diodes, photo cells, CCD matrixes etc. The direction of development of technology – is a rejection of a single-crystal substrate and formation of rectifying junction entirely by a method of magnetron sputtering. It is especially necessary to mark that the method of formation of the rectifying junction described in this paper differs from classical methods. The given method is actual due to the economic profitability and small energy consumption.

REFERENCES

1. *Пасынков В. В., Чиркин Л. К.* Полупроводниковые приборы. СПб. : Изд-во «Лань», 2001. 480 с.
2. *Cheng-Chung Leea, Der-Jun Jana.* DC magnetron sputtering of Si to form SiO_2 in low-energy ion beam // Vacuum 80 .2006. C. 693–697.

THE CLASTERIZATION OF PLAGUE MICROBE STRAINS BY MULTILOCUS VNTR-ANALYSIS.

N. Y. Nosov

Saratov State University

Plague is a zoonotic, natural focal, particularly dangerous, bacterial infectious disease with predominantly vector-borne mechanism of transmission [1, 2].

The natural foci of plague are located in the areas of most of the continents – Asia, Africa, Europe, North and South America. There are 45 natural foci of plague in Russian Federation and near abroad, 11 from which are located in Russia [3, 4].

Such wide distribution of the plague microbe around the world, its high pathogenicity and ability of using in bioterrorism acts shows that plague is a very important social-significant problem of international meaning. Solution of this problem needs a creation of new highly-effective tools of diagnostics and prevention of plague.

For estimating a strain source which caused the localized outbreak or epidemic of plague we need an effective system of molecular typing of *Yersinia*

pestis, which allows us to determine belonging of the selected isolates to specific subspecies, biovar and natural focus.

Modern molecular-genetic systems such as PCR, sequencing and multilocus analysis of variable tandem repeats – VNTR – analysis shows high differentiating capabilities relating to different bacterial species.

VNTR (Variable number of tandem repeats) – is a site of genome in which short nucleotide sequence repeated in multiple tandem copies. Variable tandem repeats have been found in many bacterial genomes and have differences in the nucleotide sequence and in the length of repeat. Such differences allow us to provide the individual identification of organism [5].

The two first methods – PCR and sequencing are perfectly suits for species-specific and intraspecific (subspecies, biovars) detection of microbes, while the method of VNTR-analysis because of the greater variability of DNA's target used is required for providing the clustering of strains according to their geographical origin and for determining the specific genotypes of isolates from different natural foci of plague.

The method of VNTR-analysis is widely used abroad, but little used for the analysis of strains from natural foci of *Y.pestis* in Russian Federation and near abroad.

Purpose of the work: to examine the effectiveness of three VNTR loci – ms01, ms04 and ms46 for clusterization of *Y.pestis* strains on natural focal origin.

Objectives:

1. To analyze the variability of VNTR loci – ms01, ms04 and ms46 *Y.pestis* strains by PCR and sequencing.

2. To assess the possibility of VNTR loci discriminating for each clustering strains of plague on the geographical origin.

3. To analyze the effectiveness of the integrated use ms01, ms04 and ms46 to establish the natural focal origin of strains *Y.pestis*.

We used 70 *Y.pestis* strains of different origin. Their study was carried out using the methods of PCR and sequencing. For the amplification of VNTR loci we used primers and reaction conditions as had been proposed in the work [6].

According to the results of the electrophoresis the least variable was locus ms01. The sizes of fragments generated by PCR with primers for this locus differed slightly, suggesting that the variability in the number of tandem repeats of this locus in strains of the plague is low. Ms04 and ms46 were the most variable, ms46 was much superior to ms04 by the differences produced in the PCR fragments.

According to «The microorganism Tandem Repeats Database» the locus ms01 has repeat with length of 18 bp and the multiplicity of repeat usually ranges from 6 to 10. The length of repeat of the locus ms04 is equal to 17, and the multiplicity ranges from 5 to 9 repeats. The locus ms46 repeat length is variable, and the multiplicity ranges from 5 to 15 repeats [7].

Were sequenced the resulting PCR fragments of the three VNTR loci, which allowed us to determine the number of repeats within each of the loci in the studied strains of the plague. In this analysis of data we used VNTR sequencing computer database «The Microorganism Tandem Repeats Database».

Construction of dendrograms has been performed by a computer program Mega 4.0 and with using distance-matrix method of UPGMA (Unweighted Pair Group Method with Arithmetic Mean).

In case of using data about sequencing of the first VNTR locus – ms01, studied strains has been divided into 10 genotypes. Strains of medieval biovar from different natural plague foci have a single genotype and, therefore, the use of this VNTR locus allowed us to allocate the medieval biovar strains, but it did not provide their differentiation of focal origin. The use of locus ms01 allocated to a separate group strains of the altaica and hissar subspecies (which is justified due to the closely connections of these strains), but also not divided them among themselves, as well as strains of the ancient and eastern biovars and ulegeica subspecies, they combined into one cluster. Locus ms01 showed highest resolution according to the strains of the caucasian subspecies, which he divided into several VNTR-types.

Use of Locus ms04 allowed us to identify eight genotypes among the strains we studied, including strains of east biovar, as well as strains of ulegeica and hissar subspecies. However, the application of ms04 cannot differentiate between strains of altaica and caucasian subspecies, and is not differentiate between the strains of the medieval biovar.

The most variable was the locus ms46, which allowed us to identify 15 genotypes among the studied strains. This locus is not clearly differentiate strains of ancient and oriental biovars, and the altaica and hissar subspecies, but singled out one group of caucasian subspecies as well as the strains of ulegeica subspecies.

The advantage of this locus lay in the fact that he perfectly shared the strains of medieval biovar by natural-focal origin, which was important because their centers that are located in the Russian Federation are predominantly refer to the foci of the steppe, plains and desert types, where the strains of medieval biovar are circulate.

Differentiating ability of VNTR analysis is significantly increased with integrated use of multiple sites of variable tandem repeats. The combined use of ms01, ms04 and ms46 allowed us to differentiate strains of the ancient, medieval, oriental biovars, and hissar, ulegeica, the caucasian and altaica subspecies with the definition of the focal origin of strains.

The combination of these loci is optimal, since each has its advantages: ms04 well divides ulegeica strains and strains of hissar subspecies, ms01 differentiate between strains of caucasian subspecies, as well ms46 divides the strains within a genetically homogeneous medieval biovar. The use of three VNTR loci – ms01, ms04 and ms46 allows us to differentiate strains *Y.pestis* by natural-focal origin.

So, as a result of performed analysis of variability of the three VNTR loci – ms01, ms04 and ms46 by PCR and sequencing we could assess the discriminating features of each of these loci for intraspecific differentiation of strains of plague. It was shown that in the case of an unknown isolate *Y.pestis* allocation by the number of copies of VNTR loci in the ms01, ms04 and ms46 can determine membership of the strain and relation to specific geographical natural focus.

Conclusions

1. The comprehensive study of the effectiveness of uses of the three VNTR loci – ms01, ms04 and ms46 for establishing the nature focus origin of *Y.pestis* strains, circulating in the Russian Federation and CIS countries have been conducted for the first time.

2. Their high discriminating ability for clustering of strains *Y.pestis* geography have been shown.

3. Was developed the algorithm of VNTR typing of strains of *Y.pestis* natural focal origin on the basis of the three loci – ms01, ms04 and ms46, which allows one to identify and strains of unknown origin.

REFERENCES:

1. *Черкасский Б. Л.* Инфекционные и паразитарные болезни человека / Медицинская газета. 1994. 617 с.
2. *Кутырев В. В., Коннов Н. П., Волков Ю. П.* Возбудитель чумы; ультраструктура и локализация в переносчике. М. : Медицина, 2007. 211 с.
3. *Онищенко Г. Г., Кутырев В. В., Попов Н. В. и др.* Природные очаги чумы Кавказа, Прикаспия, Средней Азии и Сибири. М. : Медицина, 2004. 191 с.
4. *Сучков И. Ю., Водопьянов А. С., Водопьянов С. О., Шишияну М. В., Мишанькин Б. Н.* Мультилокусный VNTR – анализ в изучении популяционной структуры Yersinia pestis в природных очагах // Молекул. генет., микробиол. и вирусол. М. : Медицина, 2004. Т. 4. С. 20.
5. Genomes, Polymorphism and Minisatellites with a focus on Molecular Epidemiology using Tandem Repeats, available at : http://minisatellites.u-psud.fr.
6. *Le Flèche P., Hauck Y., Onteniente L. et al*. A tandem repeats database for bacterial genomes : application to the genotyping of Yersinia pestis and Bacillus anthracis. BMC Microbiol., 2001. P. 8.
7. Plague. Fact sheets № 267. World Health Organization, Available at : http//www.who.int/mediacentre/factsheets/fs267/en/index.htm.

INFLUENCE OF THE LIVE ENVIRONMENT ON NANOPARTICLES

A. Osokina

Saratov State University

1. Introduction

Many substances in a nanocondition get new properties: for example, they can get inside biological structures, or pass through membranes of cages. Also they become more catalystically active.

There is a lot of research work devoted to the influence of nanoparticles on biological objects [1, 2, 3], however the way nanoparticles change under the influence of the live environment is not studied. Therefore the purpose of the paper is to study the influence of the live environment on nanoparticles.

To achieve the purpose it is necessary to solve the following problems:

1. To consider changes of the morphology of nanoparticles before and after their interaction with the live environment;

2. To find the software for illustration of the distribution of sizes of nanoparticles;

3. To consider changes of element structure of nanoparticles;

4. To calculate change of a thickness of nanoparticle shells.

2. Research of changes of structure of nanoparticles before and after influence of the live environment

The ultradisperse powder of silicon was chosen as investigated particles (the specific area = 67 m^2/g). This choice is based on the fact that silicon not only possesses enough high luminescence, but also shows bioactivity (it gradually reacts with bioliquids in organism, forming silicon acids). Also, silicon is biocompatible and has biodegidratational properties.

Two kinds of colloidal solutions were prepared:

1. A solution from ethyl spirit (2,5 ml), the distilled water (2,5 ml) and silicon nanoparticles (0,01 g);

2. A solution from the distilled water (5 ml), yeast (0,05 g), sugar (0,05 g) and silicon nanoparticles (0,01 g).

The first solution was prepared for studying of morphology, the sizes and a chemical compound of silicon before interaction with biological objects. The components of the second solution, such as yeast and sugar, will ferment, thereby creating the conditions similar to the live environment. Thus, the second solution will show influence on the particles of silicon placed in this environment. Level pH of soluions is sour that is similar to conditions in a human body.

These colloidal solutions were stored at room temperature. Further samples were placed in an ultrasonic bath for prevention of pasting of nanoparticles.

After that ultrasound solutions were put onto organic glass and dried up. Five nm-thick gold was sprayed for better conductivity. Further they were investigated on a scanning electronic microscope (SEM) MIRA//LMU.

2.1. Changes in morphology

At research of the first solution it was possible to define nanodimensional particles and to calculate their sizes (fig. 1). It is visible that nanoparticles have the roundish form and many of them are divided with the help of ultrasound. It facilitates the further analysis of the sizes by means of the software.
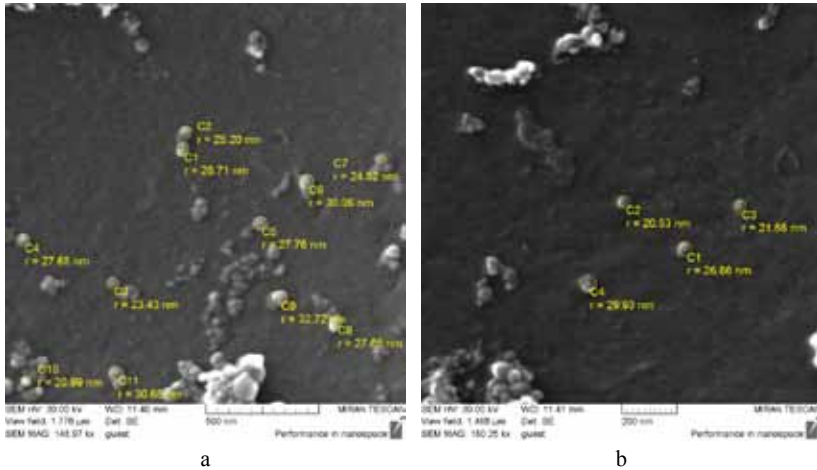
Fig. 1 – SEM images of particles of silicon before interaction with the live environment
(*a*, *b*)

Samples of the second solution have been investigated in a day and in three days for supervision of process of change of particles. The data presented on fig. 2 shows morphology of particles after interaction with the live environment.

It is visible that particles are not divided. Also it is visually visible that the size of particles has decreased. On fig. 2 (*d*) there is a general view of the sample with increase 8 kx which shows that yeast has surrounded particles of silicon.

Thus, comparing with the morphology before influence of the live environment, it is possible to make the assumption that yeast influences on arrangement, division and the size of particles.

2.2. Changes in sizes

To find the distribution of sizes of nanoparticles it is necessary to use the software. Program ImageJ (Image Processing and Data Analysis in Java) has been chosen for that. This program was specially developed for the analysis of medical and biological images. This program has an open code and freely extends [4]. Program ImageJ has an unlimited potential for solving problems of the analysis of images. For example, with the help of this program you can

measure endocellular structures and analyse histologic samples. This program is used in medicine, biology, materials technology and astronomy.
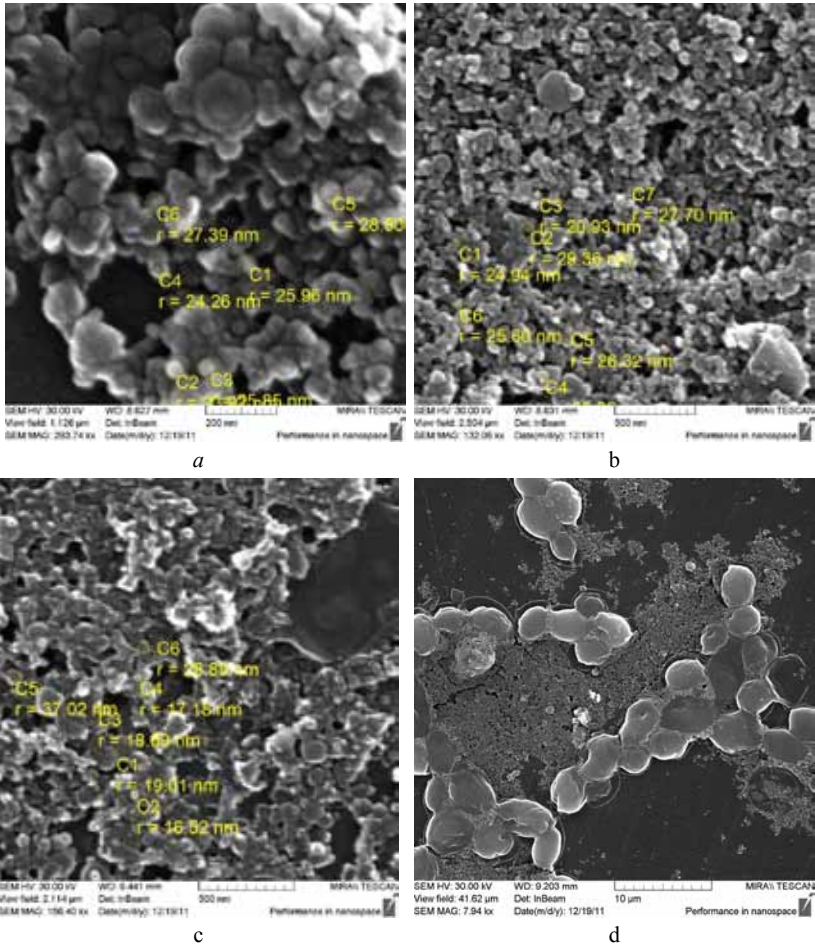
Fig. 2 . SEM images of nanoparticles of silicon after interaction with the live environment in a day (*a*, *b*), in three days (*c*) and a general view of the sample (*d*)

With the help of this software, distributions of sizes of nanoparticles before and after interaction with yeast were illustrated. Comparing the known scale on the image with quantity of pixels, the areas of nanoparticles were counted. Assuming that particles have the round form, values of diameters were counted. On fig. 3,4,5 the received results are presented.
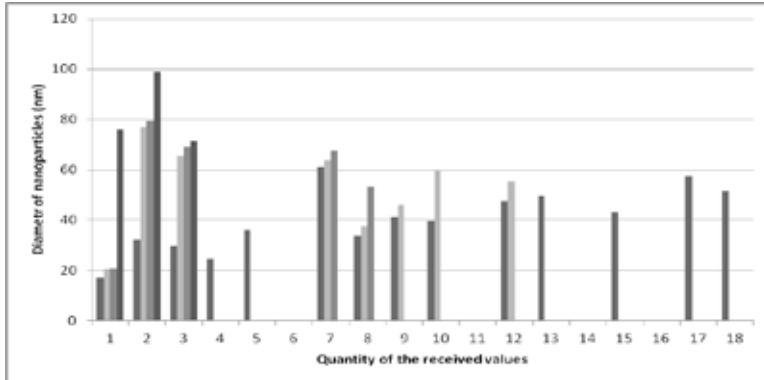
Fig. 3. Visualization of distribution of particles in the sizes before interaction with the live environment
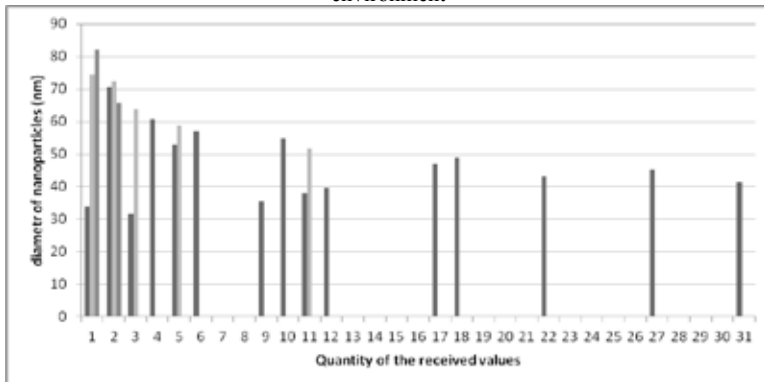
Fig. 4. Visualization of distribution of particles in the sizes after interaction with the live environment in a day

Data show that the disorder in values of diameter nanoparticles has decreased. This means hat particles became more average. Average diameter also changed as you can see in table 1.

Table 1

Change of average diameter nanoartcles under the influence of the live environment

Time of influence of the live environment	Average diameter of nanoparticles (nm)
Before interaction	58,9
Interaction in a day	47,8
Interaction in three days	30,2

88
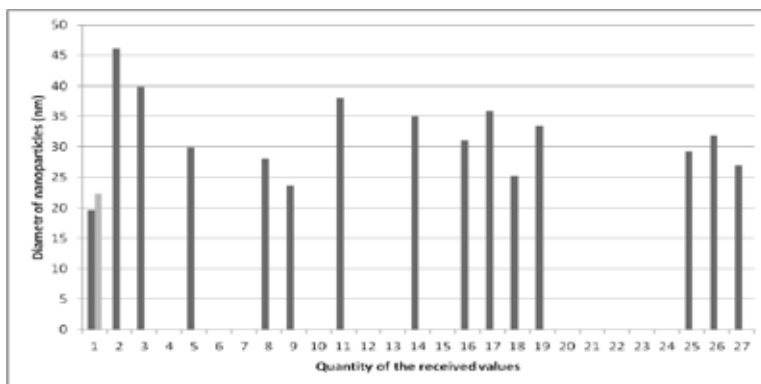
Fig. 5. Visualization of distribution of particles in the sizes after interaction with the live environment in three days

Data of the analysis of the sizes of particles confirm the assumption of reduction of the sizes of the particles, made after the morphology analysis. Thus, silicon passes in the live environment. And, if the disorder in values is decreased, it is possible to assume that yeast influenced on large particles of silicon at first.

2.3. Changes in element structure

The qualitative and quantitative analysis of element structure of structures was carried out by means of system of energy-dispersive microanalysis Inca Energy. The data of structure of samples is presented in tab. 2, 3, 4.

Table 2

**Element structure of the sample before interaction
with the live environment (the data is presented in nuclear %)**

Spectrum	C	O	Si
Spectrum 1	27.29	38.67	33.17
Spectrum 2	19.95	36.36	43.69
Spectrum 3	52.50	30.21	46.06
Spectrum 4	19.17	34.77	46.06
Spectrum 5	19.33	42.31	38.36
Spectrum 6	42.48	31.89	24.76
Spectrum 7	24.91	30.53	32.27
Spectrum 8	32.89	33.09	32.95
Spectrum 9	36.88	32.31	28.75
Spectrum 10	37.18	28.63	32.97

89

Spectrum	C	O	Si
Spectrum 11	48.62	33.69	17.12
Spectrum 12	51.90	35.12	12.53
Spectrum 13	57.54	29.10	13.37
Spectrum 14	55.75	31.24	13.00
Spectrum 15	47.24	31.82	20.94
Spectrum 16	30.58	40.03	29.38
Spectrum 17	30.03	33.61	36.36
Average	37.31	33.73	27.82

Table 3

Element structure of the sample after interaction with the live environment in one day (the data is presented in nuclear %)

Spectrum	C	O	Si
Spectrum 1	82.89	13.87	3.23
Spectrum 2	86.08	10.43	3.49
Spectrum 3	80.64	16.07	3.29
Spectrum 4	77.90	18.62	3.48
Spectrum 5	65.96	28.21	5.82
Spectrum 6	68.65	25.49	5.86
Spectrum 7	66.60	28.04	5.36
Average	75.53	20.10	4.36

Table 4

Element structure of the sample after interaction with the live environment in three days (the data is presented in nuclear %)

Spectrum	C	O	Si
Spectrum 1	80.55	15.91	3.54
Spectrum 2	81.32	15.32	3.36
Spectrum 3	76.85	20.17	2.98
Spectrum 4	79.68	16.90	3.41
Spectrum 5	81.09	16.94	1.98
Spectrum 6	82.74	15.38	1.88
Spectrum 7	81.09	16.68	2.22
Average	80.47	16.76	2.77

Data show that the quantity of carbon increases, and the quantity of oxygen decreases. This may be explained in terms of yeast's ability of living. Yeast

is the monocelled microorganisms which belong to the class of mushrooms. The enzymes which are in yeast, promote development of their all vital signs, including processes of breath, reproduction, construction of bodies of a cage. In yeast a number of complexes of enzymes operate. The main of them is zymase. Zymase is an enzyme complex («mixture») that catalyzes the fermentation of sugar into ethanol and carbon dioxide. Thus barmy cages receive the energy necessary for the ability to live [5].

3. Definition of a thickness of a cover of nanoparticles before and after interaction with the live environment

The thickness of a cover on element structure was calculated with the help of specially received formulas (1, 2, 3, 4):

$$d = D \left[A \frac{N_{Si}}{N_0} \right]^{1/3} \cdot \left[A \frac{N_{Si}}{N_0} + B - C \right]^{1/3}, \tag{1}$$

$$A = \frac{\rho_{SiO_2} \cdot M_0}{\left(M_{SiO_2} \right)^2}, \tag{2}$$

$$B = \frac{\rho_{SiO_2} M_{Si}}{\left(M_{Si} \right)^2} \tag{3}$$

$$C = \frac{\rho_{SiO_2} \cdot M_{Si}}{\left(M_{Si} \right)^2} \tag{4}$$

N_{Si} – quantity of silicon in nuclear %,

N_0 – quantity of oxygen in nuclear %,

ρ_{SiO_2} – density of silicon oxide,

ρ_{Si} – density of silicon (tabular value),

M_{Si} – molecular weight of silicon (data of element structure),

M_{SiO_2} – molecular weight of silicon oxide (data of element structure).

If you know D (diameter of nanoparticles, which you can get from results of research of morphology of nanoparticles on a microscope) and if you calculate d (diameter of a kernel of nanoparticles), it is possible to define value of a thickness of a cover.

The obtained data is presented in table 5.

Table 5

Change of a thickness of a cover of nanoparticles under the influence of the live environment

Time of influence of the live environment	*Thickness of a cover of nanoparticles (nm)*
Before interaction	24
Interaction in a day	21
Interaction in three days	13,7

From the received data it is evident that the thickness of a cover of nanoparticles decreases with the increase of time of influence of the live environment. It is possible to consider the given calculations fair in the assumption that the cover structure has no changes.

4.Conclusion

In this paper the influence of the live environment on nanoparticles was studied.

As a result of researches the following data were obtained:

1. The morphology of nanopatricles was investigated. The conclusion was drawn that silicon particles decrease after influence of yeast.

2. The program ImageJ was found to illustrate the distribution of sizes of nanoparticles. The received data (fig. 3, 4, 5) show that the disorder in values of diameter of nanoparticles has decreased. Particles became more average. and average diameter decreased. Before interaction it was 58,9 nanometers, after one day of interaction – 47,8 nanometers and after three – 30,2 nanometers. Thus, it is possible to draw a conclusion that silicon passes in the live environment.

3. Changes of element structure were investigated. The quantity of carbon has increased, and the quantity of oxygen has decreased. The reason of it is processes of ability to live of yeast.

4. The thickness of a cover of nanoparticles also has decreased. Before the interaction with the live environment value of a thickness was 24 nanometers, after one day of interaction–21 nanometer and after three – 13,7 nanometers.

REFERENCES

1. *Сопова Е. А.* Влияние нанопорошков серебра и диоксида кремния на развитие герпес-вирусной инфекции in vitro // Гигиена и санитария. 2010. № 4. 204 с.
2. *Lewinski N., Colvin V.* Cytotoxicity of Nanoparticles // Small-journal. 2008. 4, № 1, P. 26–49.
3. *Lesniak W., Bielinska A.* Silver/Dendrimer nanocomposites as biomarkers : fabrication, characterization, in vitro toxicity and intracellular detection // Nanoletters. 2005. Vol. 5. Iss. 11. P. 2123–2130.
4. Программа ImageJ. URL: http://rsb.info.nih.gov/ij/.
5. *Абрамов Ш. А., Котенко С. Ц.* Морфологические и некоторые биотехнологические свойства нового штамма Saccharomyces oviformis МФ-1 // Хранение и переработка сельхозсырья. 2001. № 12. 151 с.

BOUNDARY OF GENERALIZED SYNCHRONIZATION IN TWO UNIDIRECTIONALLY COUPLED TUNNEL DIODE GENERATORS

A. S. Pavlov

Saratov State University

Synchronization of chaotic oscillations is one of the most interesting nonlinear phenomena actively studied recently (*Boccaletti, Kurths, Osipov, Valladares, Zhou, 2002*). It has an important both fundamental and applied significance, in particular, in biology, physiology, secure data transmission using chaotic signals, control of oscillations in microwave electronics systems, etc. (*Короновский, Москаленко, Храмов, 2009; Glass, 2001; Трубецков, Короновский, Храмов, 2004*). Several types of the synchronous chaotic system behavior are traditionally distinguished. They are phase, generalized, lag, complete synchronization and others (*Boccaletti, Kurths, Osipov, Valladares, Zhou, 2002*).

One of the most important questions connected with the chaotic synchronization regime studying is the behavior of the boundary of generalized synchronization (GS) regime (*Rulkov, Sushchik, Tsimring, Abarbanel, 1995*) and its relationship with the onset of phase synchronization (PS) (*Pikovsky, Rosenblum, Kurths, 2000*). In the case of two unidirectionally coupled chaotic oscillators the GS regime onset means that the drive $\mathbf{x}_d(t)$ and response $\mathbf{x}_r(t)$ system states obey a unique functional relation $\mathbf{x}_r(t) = \mathbf{F}[\mathbf{x}_d(t)]$ after the transient process is finished. Several methods of the GS regime detection, such as the nearest neighbor method (*Rulkov, Sushchik, Tsimring, Abarbanel, 1995; Parlitz, Junge, Lauterborn, Kocarev, 1996*), conditional Lyapunov exponent computation (*Pyragas, 1997*) and auxiliary system method (*Abarbanel, Rulkov, Sushchik, 1996*) are known at present. The PS regime onset implies the phase locking of chaotic signals whereas their amplitudes remain usually uncorrelated and look chaotic (*Pikovsky, Rosenblum, Kurths, 2000*).

Recently it has been shown that the behavior of the boundaries of the GS and PS regimes in two unidirectionally coupled Rössler systems depends strongly on the value of the control parameter mistuning (*Zheng, Hu, 2000*). In particular, in the case of relatively small values of parameter mismatch GS is appeared to be stronger than PS, whereas for sufficiently large values of parameter mistuning the threshold value of the coupling parameter corresponding to the PS regime onset is significantly greater than that for the GS one. At that, the critical value of the coupling parameter corresponding to the GS onset does not practically depend on the value of parameter mistuning (*Hramov, Koronovskii, Moskalenko, 2005; Короновский, Москаленко, Храмов, 2006*), and onset/destruction of PS is connected with the appearance/loss of the phase coherence of chaotic attractor of the response system (*Короновский, Куровская, Москаленко, Храмов, 2007; Hramov, Koronovskii, Kurovskaya, 2007*).

Later the reasons of such behavior of the boundaries of the GS and PS regimes have been explained and physical mechanisms resulting in the synchronous regime onset have been revealed (*Короновский, Москаленко, Храмов, 2007; Москаленко, 2010*). In particular, it has been shown that in the field of the relatively small values of the proper frequencies of interacted Rössler system detuning the GS arises due to synchronization of the main spectral component and its subharmonics (whereas PS obeys a scenario of main frequency locking). In the field of relatively large detunings of the proper frequencies the GS onset is accompanied by synchronization of two spectral components that correspond to the proper frequency of the drive system and the main frequency of the response one.

This paper presents the results of investigation of the behavior of the boundaries of GS and PS regimes in unidirectionally coupled tunnel diode generators (*Короновский, Куровская, Москаленко, Храмов, 2007*). In a dimensionless form this system can be described by the following differential equations:

$$\dot{x}_d = \omega_d^2 \cdot (h \cdot x_d + y_d - z_d),$$
$$\dot{y}_d = -x_d,$$
$$\dot{z}_d = (x_d - f(z_d))/\mu,$$

$$\dot{x}_r = \omega_r^2 \cdot (h \cdot (x_r - \varepsilon \cdot (y_d - y_r)) + y_r - z_r),$$
$$\dot{y}_r = -x_r + \varepsilon \cdot (y_d - y_r),$$
$$\dot{z}_r = (x_r - f(z_r))/\mu,$$

(1)

where $f(\xi) = -\xi + 0.002\sinh(5\xi - 7.5) + 2.9$ is the dimensionless characteristics of nonlinear element, $h = 0.2$ and $\mu = 0.1$ are control parameters, ε is the coupling parameter, $\omega_r = 1.02$ is the main frequency of the response system and ω_d is the analogous parameter of the drive system. It has been varied in the field [0.94; 1.12] providing the interacted system mistuning. For the indicated values of the control parameters the chaotic attractors of both systems in the absence of coupling are phase-coherent (*Короновский, Куровская, Москаленко, Храмов, 2007*).

Figure 1 shows the boundaries of the GS and PS regime onset and appearance/loss of the phase coherence for system (1) on (ω_d, ε)-plane. The threshold of GS onset has been determined by conditional Lyapunov exponent calculation for Eqs. (1) and then refined by the auxiliary system method. The moment of the appearance/loss of the phase coherence of the chaotic attractor of the response system has been determined by calculation of the coherence measure (*Hramov, Koronovskii, Kurovskaya, 2007*) as a function of the coupling parameter. The onset of PS has been determined by the condition of phase locking. The instantaneous phases of chaotic signals have been defined as rotation angles on the (x, y)-plane.
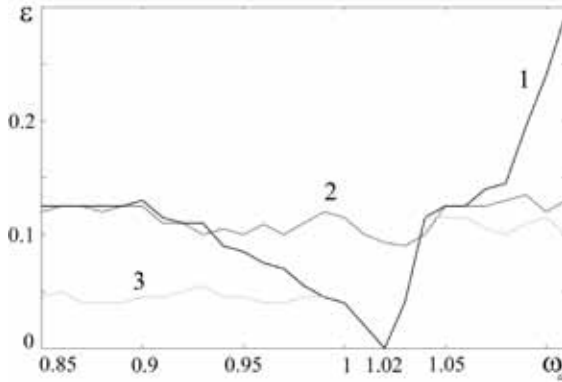
Fig. 1. Boundaries of the PS (curve *1*), GS (curve *2*) onsets and appearance/loss of the phase coherence of attractor of the response system (curve *3*) on the (ω_d, ε)-plane for system (1)

It is clearly seen from Fig. 1 that the boundaries of the synchronous regimes are asymmetric relative to the $\omega_d = \omega_r$ line, that can be connected with the strong influence of dissipation in the response system taking place with an increase of the coupling parameter value. On the other hand, the boundary value of the GS regime does not almost depend on the parameter ω_d, at that, relation of the boundary values of the GS and PS regime onset is different in the fields of the relatively large and relatively small values of the control parameter mistuning. If control parameters detuned slightly, the situation is the same as in the case mentioned above. If parameter mismatch is large enough both in the left and right sides from $\omega_d = \omega_r$ line the destruction of PS regime is accompanied by the loss of the phase coherence of the chaotic attractor of the response system (Fig. 1, curve *3*). In this case if $\omega_d > \omega_r$ the situation is similar to the last one in Rössler systems described above, i.e. PS is stronger GS and boundaries of GS and loss of phase coherence are close to each other. If $\omega_d < \omega_r$ the field of the relatively large values of parameter mismatch can be divided into two parts. In the first part ($\omega_d < 0.93$) the relation of GS and PS is the same as mentioned above whereas the second part ($0.93 < \omega_d < 0.99$) demands special attention. Despite of the fact that relation of GS and PS boundaries corresponds to the case of relatively small values of control parameter mismatch, the PS regime destruction is accompanied by the loss of the phase coherence of the response system attractor that is not typical for unidirectionally coupled chaotic systems.

Such behavior of the GS and PS boundaries on the (ω_d, ε)-plane can be explained as follows. Obviously, in the field of relatively small control parameter mistuning ($\omega_d \in [0.98, 1.04]$, where the PS destruction takes place without the loss of the phase coherence of chaotic attractor of the response system), the PS in the system under study (as well as in the case of coupled Rössler oscilla-

tors) arises due to the locking of the main spectral components of the drive and response systems. At the same time, the GS regime arises via synchronization of the main spectral component of the response system and its subharmonics (*Короновский, Москаленко, Храмов, 2007; Москаленко, 2010*). In the fields of $\omega_d > 1.04$ and $\omega_d < 0.93$, the behavior is analogous to the last one observed for two unidirectionally coupled Rössler systems with relatively large main frequency detuning, whereby the chaotic attractor of response system (1) below the PS boundary becomes phase-incoherent, which leads to the PS regime destruction. Moreover, Fig. 1 shows that the boundary of GS regime in the field of relatively large control parameter mismatch is close to the boundary of appearance/loss of the phase coherence in the chaotic attractor. It is clear that the GS in this case arises due to the synchronization of two pronounced spectral components (corresponding to the frequencies of the drive and response system), the intensities of which near the GS boundary are close to each other.

The most interesting situation takes place in the field of relatively large values of the control parameter mistuning where $0.93 < \omega_d < 0.99$. As it has been mentioned above, here the PS onset/destruction is still determined by the appearance/loss of the phase coherence in the chaotic attractor of the response system, whereas the relation between GS and PS regimes is analogous to the last one in the case of small detunings. Moreover, the GS threshold in this case does not practically depend on the value of ω_d in the region below 0.98. Apparently, the mechanism of GS onset in this case should be different.

Later we consider the relation between GS and PS regimes in the field $0.93 < \omega_d < 0.99$ in more detail. For the selected values of control parameters and $\omega_d = 0.96$ the increase of the coupling parameter ε in system (1) leads to the following changes. At $\varepsilon = \varepsilon_{CM} = 0.04$, the chaotic attractor of the response system loses its phase coherence; at $\varepsilon = \varepsilon_{PS} = 0.075$ the system begins to demonstrate the PS regime; and at $\varepsilon = \varepsilon_{GS} = 0.107$ the system exhibits GS.

Fig. 2 shows Fourier spectra of oscillations in the response system for different values of the coupling parameter. It is clearly seen that the increase of the coupling parameter ε leads to the decrease in the intensity of the spectral component at the main frequency of the response system and the increase in the component at the main frequency of the drive system. The main frequency of the response system shifts left with the coupling parameter value increasing and eventually (since $\omega_d < \omega_r$) this leads to the locking of the main frequencies of interacting systems and, hence, to the PS regime onset. This situation takes place at a certain value of the coupling parameter, for which the intensity of the spectral component on the frequency of the drive subsystem in Fourier spectrum of the response system becomes significant. Below the PS threshold, the spectrum of the response system contains two components and its attractor is phase-incoherent. However, the PS arises by scenario corresponding to the case of relatively small detunings of the main frequencies. Indeed, already for $\varepsilon = 0.1$, the Fourier spectrum of oscillations in the response system exhibits a single well-pronounced spectral component on the frequency of the drive

system. Obviously, the GS regime in this case will also arise by scenario corresponding to the case of a relatively small detunings of the main frequencies, i.e. by synchronization of the main spectral component of the drive system and its subharmonics.
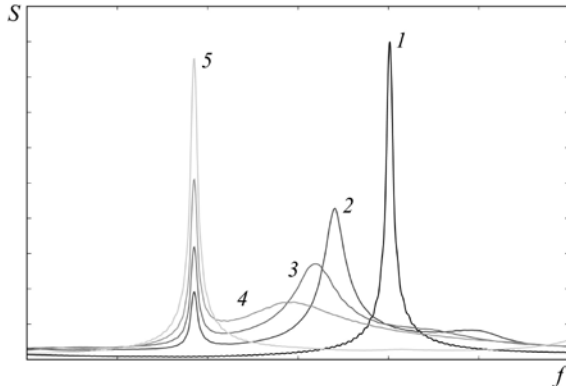

Fig. 2. Fourier spectra of oscillations in the response system of (1) for $\omega_d = 0.96$ and different values of the coupling parameter ε: $1 - \varepsilon = 0$; $2 - \varepsilon = 0.04$; $3 - \varepsilon = 0.05$; $4 - \varepsilon = 0.06$; $5 - \varepsilon = 0.1$

In conclusion, we have considered the GS onset in two unidirectionally coupled tunnel diode oscillators. It has been found that the GS regime in the case of the relative large values of the control parameter mistuning can arise by scenario corresponding to the relatively small detunings of the main frequencies of interacted systems. The behavior of the boundary of GS regime and its relation with the PS regime in the system under study is explained using the analysis of the transformation of the spectral compound of oscillations in the response system.

REFERENCES

1. *Короновский А. А., Куровская М. К., Москаленко О. И., Храмов А. Е.* // ЖТФ. 77. 1. 2007. С. 21–29.
2. *Короновский А. А., Москаленко О. И., Храмов А. Е.* // Письма в ЖТФ. 32. 3. 2006. С. 40–48.
3. *Короновский А. А., Москаленко О. И., Храмов А. Е.* // Радиотехника и электроника. 52. 8. 2007. С. 949–960.
4. *Короновский А. А., Москаленко О. И., Храмов А. Е.* // УФН. 179. 12. 2009. С. 1281–1310.
5. *Москаленко О. И.* // ЖТФ. 80, 8 (2010) 1–7.
6. *Трубецков Д. И., Короновский А. А., Храмов А. Е.* // Изв. вузов. Радиофизика. XLVII. 5–6. 2004. С. 305–331.

7. *Abarbanel H. D.I., Rulkov N. F., Sushchik M.* // Phys. Rev. E. 1996. Vol. 53. № 5. P. 4528–4535.
8. *Boccaletti S., Kurths J., Osipov G. V., Valladares D. L., Zhou C. S.* // Physics Reports. 366. 2002. P. 1–100.
9. *Glass L.* // Nature. 2001. Vol. 410, № 6825. P. 277–284.
10. *Hramov A. E., Koronovskii A. A., Kurovskaya M. K.* // Phys. Rev. E. 75. 2007. 036205.
11. *Hramov A. E., Koronovskii A. A., Moskalenko O. I.* // Europhysics Letters. 72. 6. 2005. P. 901–907.
12. *Parlitz U., Junge L., Lauterborn W., Kocarev L.* // Phys. Rev. E. **54**(2). 1996. P. 2115–2117.
13. *Pikovsky A. S., Rosenblum M. G., Kurths J.* // Int. J. Bifurcation and Chaos. **10.** 10. 2000. P. 2291–2305.
14. *Pyragas K.* // Phys. Rev. E. **56**(5). 1997. P. 5183–5188.
15. *Rulkov N. F., Sushchik M. M., Tsimring L. S., Abarbanel H. D.I.* // Phys. Rev. E. 1995. Vol. 51. № 2. P. 980–994.
16. *Zheng Z., Hu G.* // Phys. Rev. E. 62(6). 2000. P. 7882–7885.

SYNTHESIS OF 2-(2,7-DICHLORO-3-OXO-6-(PERFLUOROPHENYLSULFONYLOXY)–3H-XANTHEN-9-YL) BENZOIC ACID

O. A. Perfilova

Saratov State University

INTRODUCTION

Molecular probes and molecular sensors for hydrogen peroxide (H_2O_2) are important in the environmental and bioanalytical sciences for a number of reasons. H_2O_2 is present in small but significant concentrations in the atmosphere and the marine environment. It is widely used in industry for bleaching, cleaning, and disinfection, and released to the environment in large quantities. H_2O_2 is one of the products of the activity of almost all oxidases.

Finally, H_2O_2 is known to be the cause of various kinds of DNA damage in mammalian and plant cells; an area of particular current research activity. Obviously, molecular probes for H_2O_2 are of broad interest in environmental and biochemistry research, in clinical assay and screening.

Many diseases associated with human aging, including cancer, cardiovascular disorders, and neurodegenerative diseases, have a strong oxidative stress component, but the basic molecular mechanisms that connect aging, age-related diseases, and oxidative stress remain insufficiently understood.

Oxidative stress is the result of unregulated production of reactive oxygen species (ROS), and cellular mismanagement of oxidation reduction chemistry can trigger subsequent oxidative damage to tissue and organs.

In particular, hydrogen peroxide is a major ROS byproduct in living organisms and a common marker for oxidative stress. The chemical biology of H_2O_2 is much more complex, however, as mounting evidence also supports a role for H_2O_2 as a second messenger in normal cellular signal transduction. Peroxide bursts in response to cell receptor stimulation can affect several classes of essential signaling proteins that control cell proliferation and/or cell death.

Fluorescent probes are well suited to meet the need for tools to map the spatial and temporal distribution of H_2O_2 within living cells. Such reagents have revolutionized the study of biological systems and hold much promise for enhancing our understanding of H_2O_2 physiology and pathology. The major challenge for practical H_2O_2 sensing in biological environments is creating water-soluble systems that respond to H_2O_2 selectively over competing cellular ROS such as super-oxide (O_2), nitric oxide (NO), and lipid peroxides. Several types of small-molecule reporters have been described for H_2O_2 detection. Included are dihydro derivatives of common fluorescent dyes (e.g., 2′,7′-dichlorodihydrofluorescein, DCFH). Limitations of these and other currently available H_2O_2-responsive probes include interfering background fluorescence from competing ROS, potential side reactions with thiols that are present in high concentrations within cells, the need for external activating enzyme, lack of membrane permeability, and/or lack of water solubility or compatibility, requiring the use of organic cosolvents.

EXPERIMENTAL

Several methods have been investigated in literature to detect H_2O_2, including titrimetry, fluorometry, spectrophotometry, chemiluminescence, and electrochemistry. Various sensitive fluorometric methods have been developed for the H_2O_2 determination. The basis of this work was the method of synthesis pentafluorobenzenesulfonyl fluoresceins as selective fluorescent probes for H_2O_2 [2]. Although it is of high specificity and sensitivity, its instability and high cost restrict its application.

500 mg (1,25 mmol) 2,7-diclorofluorescein and 222 µL (1,50 mmol) pentafluorobenzenesulfonyl chloride were dissolved 15 mL dichloromethane and 5 mL 2,6-lutidine stirred for 18 hours at room temperature. The reaction mixture was diluted with 100 mL dichloromethane and washed two times with 1 M HCl (100mL each) and one time with brine (100mL). The organic phase was dried over anhydrous Na_2SO_4, filtered off and reduced to dryness.

These compounds were chosen for the following reasons: sulfonates are more stable to hydrolysis than are esters; fluoresceins have high fluorescence quantum yields in aqueous solution; and the pentafluorobenzene ring enhances the reactivity of the sulfonates toward H_2O_2.

The disadvantage of this method is the absence of functional groups, which would allow to carry out further covalent bonding and immobilization.

The parent compound of preparation (2,7-diclorofluorescein) was changed in order to reduce the cost of the experiment. The effect of various factors was investigated. The ratio of carboxyfluorescein to pentafluorobenzenesulfonyl chloride at which maximum yield was obtained was optimized.

All reagents were of analytical grade. Double distilled water was used in the present work.

RESULTS AND DISCUSSION

The effects of experimental conditions including reaction time, initial carboxyfluorescein concentration, and initial pentafluorobenzenesulfonyl chloride concentration were investigated in order to optimize the possible analytical method for the H_2O_2 determination. The maximum yield was obtained at 1 : 5 ratio.

CONCLUSIONS

We have described the synthesis, properties, and biological applications of fluorescent probes for imaging H_2O_2 in biological environments.

ACKNOWLEDGMENT

REFERENCES

1. *Maeda H.,Matsu-ura Sh., Nishida M., Senba T., Yamauchi Y,Ohmori H.* Hydrogen Peroxide-Induced Deacetylation of Acetyl Resorufin as a Novel Indicator Reaction for Fluorometric Detection of Glucose Using Only Glucose Oxidase // Chem. Pharm. Bull. 2001. Vol. 49, № 3. P. 294–298.
2. *Maeda H., Fukuyasu Y., Yoshida Sh., Fukuda M., Saeki K., Matsuno H., Yamauchi Y., Yoshida K., Hirata K., Miyamoto K.* Fluorescent Probes for Hydrogen Peroxide Based on a Non-Oxidative Mechanism // Angew. Chem. 2004. Vol. 116. P. 2443–2445.
3. *Maeda H., Yamamoto K., Nomura Y., Kohno I., Hafsi L., Ueda N., Yoshida Sh., Fukuda M., Fukuyasu Y., Yamauchi Y., Itoh N.* A Design of Fluorescent Probes for Superoxide Based on a Nonredox Mechanism // J. AM. Chem. Soc. 9. Vol. 127, № 1. 2005. P. 68–69.
4. *Maeda H., Yamamoto K., Kohno I., Hafsi L., Itoh N., Nakagawa Sh., Kanagawa N., Suzuki K., Uno T.* Design of a Practical Fluorescent Probe for Superoxide Based on Protection–Deprotection Chemistry of Fluoresceins with Benzenesulfonyl Protecting Groups // Chem. Eur. J. 2007. Vol. 13. P. 1946–1954.
5. *Wolfbeis O. S. , Dorkop A., Wu M., Lin Zh.* A Europium-Ion-Based Luminescent Sensing Probe for Hydrogen // Angew. Chem. Int. Ed. 2002. Vol. 41, № 23. P. 4495–4498.
6. *Yamaguchia Sh., Kishikawaa N., Ohyamaa K., Ohbab Y., Kohnoc M., Masudac T., Takadatec A., Nakashimaa K., Kurodaa N.* Evaluation of chemiluminescence reagents for selective detection of reactive oxygen species // Analytica Chimica Acta. 2010. Vol. 665. P. 74–78.

GENERATOR WITH ELECTRON FEEDBACK UNDER EXTERNAL INFLUENCE OF HARMONIC SIGNAL

N. S. Phrolov

Saratov State University

INTRODUCTION

High-power microwave radiation sources based on relativistic electron flows with virtual cathode (VC) called vicrators are intensively studied, both theoretically and experimentally at the present time (Диденко и др.,1979; Дубинов, Селемир, 2002; Трубецков, Храмов, 2004; Benford et al., 2007). The feature of these devices is electron flow reflected from VC back to emission area which creates distributed feedback. It makes possible to interpret these devices as generators with electron feedback (Короновский, Трубецков, Храмов, 2009; Hramov, Koronovskii, Kurkin, 2010). It is known that vircators are characterized by construction simplicity, high level of output power, possibility of operation without external magnetic field (Трубецков, Храмов, 2004, Benford et al., 2007) and easiness of controlling oscillation regime by different types of feedback (Гадецкий и др., 1993; Храмов, 1999) or by feeding external signal (Калинин и др, 2005; Sze et al., 1990; Woo et al., 1989).

One of the intensive studied generator with electron feedback modifications is the system called low voltage vircator which is considered to be a promising source of both narrowband and wideband chaotic signal in microwave range (Егоров и др., 2005; Калинин и др., 2005; Короновский, Трубецков, Храмов, 2009;Woo et al., 1989). In a low voltage vircator that is, in the simplest case, a diode gap pierced by an electron flow, a virtual cathode is formed via additional deceleration of the electron flow by applying voltage that is negative relative to the input grid to the output grid of the diode gap.

A set of experiments on controlling a low voltage vircator via an external signal has been performed (Калинин, Храмов, 2006). The possibility of amplifying the external signal by electron flow with VC has been shown but the theoretical explanation of this effect has not been given. This research is devoted to construction of simple theoretical model of generator with electron feedback under external influence and the possibility of non-autonomous vircator output power increasing has been shown. Also numerically calculated low voltage vircators output power characteristics which are in good qualitative agreement with the experimental data (Калинин, Храмов, 2006).

GENERAL FORMALISM

As a vircator prototype, we have used a one dimensional model containing an electron flow through a diode gap, decelerated by means of the negative potential difference formed between the input and output grids. As a result,

when a certain beam current depending on the decelerating potential is exceeded, a nonstationary virtual cathode (a potential barrier reflecting part of electrons back onto the injection plane and modulating the passing flow) is formed in the intergrid space. In such a vircator scheme with the additional deceleration of electrons, it is possible to lower the initial currents needed to form an oscillating virtual cathode. The modulated electron flow excites a spiral electrodynamic system segment (SESS) that extracts the microwave oscillation power. The feeding of external signal is implemented using a modulating SESS placed between the electron gun and the interaction space of the generator. Fed external signal realizes velocity modulation of electron flow entering intergrid space. Variation of external signal power leads to variation of electron flow modulation depth at the diode gap entrance.

It is known that VC partially reflects electron flow back to emission area and realizes density modulation of this flow. Therefore the electron flow dynamics can be described as charged particles flow motion in decelerating field with variable component. As a simple low-voltage vircator model, we have considered intergrid space pierced by electron flow decelerated by means of the negative potential difference U_r formed between the input and output grids. Also there is a variable electric field in the intergrid space, defined by variable potential difference $U_r \cos(\omega_{VC} t)$ modelling non-stationary VC decelerating field oscillations. External signal effect is determined as velocity modulation of electron flow entering intergrid space with external singal frequency . The simpliest case when $\omega_0 = \omega_{VC}$ has been consedered.

Equation of electron motion within the limits of this model is

$$\ddot{x} = \frac{\eta}{L}\left(U_m \cos(\omega_{VC} t) - U_r\right) \tag{1}$$

where L – is interaction space length, η – charge-to-mass ratio of electron. Equation (1) has been integrated, subject to initial conditions $t_0 = t_1,\ x_0 = 0,\ v(0, t_0) = v_0\left(1 + X \sin(\omega_m t_1)\right)$, where X – velocity modulation depth, defined by external force power.

Equation (1) integration gives charged particles trajectories in interaction space:

$$x = v_0\left(1 + X \sin(\omega_0 t_1)\right)(t - t_1) - \frac{\eta U_m}{\omega_0^2 L}\, e^{j\omega_0 t} - e^{j\omega_0 t_1} - j\omega_0\, e^{j\omega_0 t_1}(t - t_1) - \frac{\eta U_r}{2L}(t - t_1)^2, \tag{2}$$

The reversal point of charged particles reflected from VC has been considered as injection area ($x = 0$), and multiplication (2) by ω_0/v_0 gives electron transit angle φ in low-voltage vircator interaction space

$$\varphi\left(1 + X \sin(\omega_0 t_1)\right) = \mu\left(e^{j\varphi} - j\varphi - 1\right)e^{j\omega_0 t_1} + \beta\varphi^2 \tag{3}$$

Where $\mu = \eta U_m / \omega_0 L v_0$ and $\beta = \eta U_r / 2L v_0$. Equation for grouped current has been found using the law of conversation of charge, subject to equation (3):

$$I = I_0 \left(1 + \frac{1}{\omega_0} \frac{d\varphi}{dt_1} \right)^{-1}, \qquad (4)$$

where I_0 – unperterbed beam current entering interaction space. Output power of generator extracted by spiral segment and defined by field created by grouped electron flow is proportional to magnitude of accelerating voltage and grouped flow current $P = kIU_0$.

RESULTS AND DISCUSSION

Analytic model analysis shows that the output power of low-voltage vircator increases while increasing velocity modulation depth of electron flow entering intergrid space (increasing external force). Figure 1 illustrates analically obtained dependence of output power amplification from velocity modulation depth. Significant power amplifivation is defined by improvement of electron flow grouping in VC area.

These analytic results have been verified within the limits of one-dimentional numerical model of generator with electron feedback. Figure 2 shows numerically calculated dependence of output integrated power of generator from the magnitude of external force. It is obvious that the power of output radiation demonstrates the similar dynamics to analitacally obtained dependence at low amplitude of external signal.
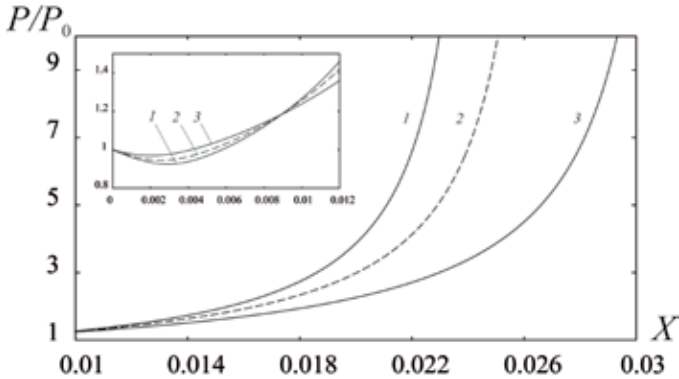
Fig. 1. The dependences of grouped current amplification from modulation depth for different decelerating potentials obtained analitically ($1 – U_r = 0.45$, $2 – U_r = 0.5$, $3 – U_r = 0.6$)

Numerical simulation, as oppesed to resultes of analytical model, showes that the output power experiences saturation and decreases while gaining external signal amplitude. The appearance of decrising area is defined by strong initial velocity modulation of electron flow entering interaction space that leads to destruction of dense electron group in VC area and increasing of cur-

rent passing through VC to the output grid at the expence of accelerated particles that can overcome VC potential barrier. Thereby the space-charge density in VC area decreases.
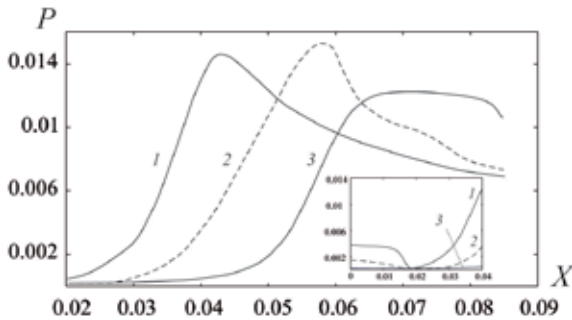
Fig.2. The dependences of output integrated power of generator from modulation depth for different decelerating potentials calculated numerically ($1 - U_r = 0.45$, $2 - U_r = 0.5$, $3 - U_r = 0.6$)

Simple analytical model can not describe effects connected with growth of current passing through the VC area because it has been supposed that all the electron current is reflected back to injection area.

CONCLUSIONS

The output power of generator with electron feedback (low-voltage vircator) under external force was analyzed both numerically and analytically. At a certain set of controlling parameters, the system exhibited sharp growth of the output power due to the dynamics of the electron flow in the intergrid space.

The obtained results are in a good qulitative agreement with experimantal data reported in (Калинин, Храмов, 2006), in which a low-voltage vircator under an external harmonic effect introduced in the system by SESS flow modulation was analyzed. It was shown that when the power of the external effect exceeds a certain critical value, rapid growth of the generator output power similar to that found in our study is observed qualitatively. This confirms that our theoretical analysis is correct.

ACKNOWLEDGMENTS

REFERENCES

Гадецкий Н. Н., Магда И. И., Найстетер С. И., Прокопенко Ю. В., Чумаков В. И. // Физика плазмы. 1993. Т. 19. № 4. С. 530.

Диденко А. Н., Красик Я. Е., Перелыгин С. Ф., Фоменко Г. П. // Письма в ЖТФ. 1979. Т. 5. № 6. С. 321.

Дубинов А. Е., Селемир В. Д. // РиЭ. 2002. Т. 47. № 6. С. 575.

Егоров Е. Н., Калинин Ю. А., Левин Ю. И. и др. // Изв. РАН, сер. физич. 2005. Т. 69. № 12. С. 1724.

Калинин Ю. А., Ремпен И. С., Храмов А. Е. // Изв. РАН, сер. физич. 2005. Т. 69. № 12. С. 1736–1740.

Калинин Ю. А., Короновский А. А., Храмов А. Е. и др. // Физика плазмы 2005. Т. 31. № 11. С. 1009–1025.

Калинин Ю. А., Храмов А. Е. // Письма в ЖТФ. 2006. Т. 32. № 13. С. 88–94.

Короновский А. А., Трубецков Д. И., Храмов А. Е. Методы нелинейной динамики и хаоса в задачах электроники сверхвысоких частот. Т. 2. Нестационарные и хаотические процессы. М. : Физматлит, 2009.

Трубецков Д. И., Храмов А. Е., Лекции по сверхвысокочастотной электронике для физиков. Т. 2. М. : Физматлит, 2004.

Храмов А. Е. // РиЭ. 1999. Т. 44. № 1. С. 116–117.

Benford J., Swegle J. A., Schamiloglu E. High Power Microwaves. CRC Press ; Taylor and Francis, 2007.

Hramov A. E., Koronovskii A. A., Kurkin S. A. // Phys. Lett. A. 2010. № 374. P. 3057–3066.

Sze H., Price D., Harteneck B. // J. Appl.Phys. 1990. Vol. 67. № 5. P. 2278–2282.

Woo W., Benford J., Fittinghoff D. et al. // J. Appl. Phys. 1989. Vol. 65. № 2. P. 861.

DETERMINATION OF ALKYLPIRIDINIUM HOMOLOGUES IN BINARY MIXTURES

E. S. Pogorelova, E. G. Kulapina, N. M. Makarova

Saratov State University

Introduction

Alkylpyridinium halides are cationic surfactants. They are part of many consumer and industrial chemical products. Usually, synthetical surfactants are not individual compounds but mixtures of polymer homologues, thus analysis of objects containing such surfactants is rather complex (Михалева и др., 2007). There are many methods for separate determination of cationic surfactants homologues in complex mixtures: spectrophotometric (Перевощикова и др., 2010; Patel, Patel 1999; Доленко и др. 2006), chemiluminescent (Safavi, Karimi 2002), chromatographic (Merino et al, 2003; Peng el al, 2011), electrophoretic (Heinig et al, 1997), but they are continuous and expensive. Potentiometric analysis with chemical sensors is a simple, express and inexpensive method for surfactant determination (Кулапина и др. 2008). However, it's impossible to use individual sensors for determination of surfactants homologues in multicomponent systems because of low selectivity

of sensor membranes. In this article, the «electronic tongue» type multisensor system is proposed for analysis of binary model mixture of alkylpyridinium homologues.

Materials and methods

All reagents used for the preparation of the membranes and solutions were analytically pure. The structural formulas of cationic surfactants are shown in Table 1.

<div align="right">Table 1</div>

Names, structural formulas and molecular masses of investigated substances.

№	Name of the substance	AN[*]	Formulas	M^{**}, mol L^{-1}
1	Decylpyridinium chloride	DP	$[CH_3 - (CH_2)_9 - C_5H_4N]\ Cl$	254,5
2	Dodecylpyridinium chloride	DDP	$[CH_3 - (CH_2)_{11} - C_5H_4N]\ Cl$	282,5
3	Cetylpyridinium chloride	CP	$[CH_3 - (CH_2)_{15} - C_5H_4N]\ Cl$	338,5
4	Octadecylpyridinium chloride	ODP	$[CH_3 - (CH_2)_{17} - C_5H_4N]\ Cl$	366,5

[*] Abbreviated name; [**] molecular mass

Initial solutions (with concentration being 1×10^{-2} mol L^{-1} and 1×10^{-3} mol L^{-1}) of cetylpyridinium chloride and sodium dodecylsulfate were prepared by dissolving corresponding amounts of substances in distilled water while slightly heating. Working solutions (with concentration being from 1×10^{-3} (1×10^{-4}) to 1×10^{-6} mol L^{-1}) were prepared by successive dilution.

All potentiometric measurements were carried out with an И-130 ionomer (analytical error ±1 mV). Standard silver chloride electrode was used as a reference electrode. Solid contact sensors with plasticized membranes based on electrode active compounds of alkylpyridinium tetraphenilborates and dodecylsulphates were used as indicator electrodes. The following transfer elements were investigated:

Ag, AgCl, KCl | analyte solution | membrane | graphite | AgCl, Ag

All experiments were performed at room temperature (20±3°C) and the analyte solutions were magnetically stirred during measurements.

Electrode-active components of membranes were prepared according to the following method: 50 ml of cetylpyridinium chloride (1×10^{-2} mol L^{-1} solution) and the same quantity of sodium tetraphenilborate or dodecylsulfate were added into 200 ml glass. White precipitate had formed and was settled for 8 hours, after that it was filtered on Schott filter (with pore diameter being 40 nm). The precipitate was flushed out with distilled water for several times until complete elimination of chloride ions. The absence of chloride ions was controlled by qualitative test with silver nitrate. The final products are white powders (Кулапина и др. 2008).

Optimal PVC (polyvinylchloride) membranes were obtained according to the following method: ion associate (1% w/w), dibuthylphtalate (74% w/w) and PVC (25% w/w) (PVC was added to the mixture in small portions) were dissolved in 3 ml of cyclohexanone at 50–60°C during constant stirring. The mixture was magnetically stirred until complete homogenization. The membrane composition was poured into a Petri dish and allowed to air until the complete removal of the solvent (appr. 30 h). The discs with diameter of 5–6 mm were cut from the resulting elastic film (with thickness of 0.5 mm) and glued onto solid graphite contacts of potentiometric sensors. Before analysis, the electrodes were kept at 1×10^{-3} mol L^{-1} solution of the main ion.

The solid contact sensors with graphite as an electronic conductor were chosen for this analysis. The ion exchange membrane was adjusted to the tip of an electrode with a PVC glue (10% w/w PVC in cyclohexanone). The molecular sieve was glued on the ion exchange membrane.

Results and discussion

According to the theory of membrane electrodes the potential at the boundary between membrane and solution (E_1) is a fundamental parameter, since the concentration dependence of the potential is caused by the processes occurring at this boundary. For example, the following reaction takes place in solutions of alkylpyridinium chlorides:

$$\left[C_m H_{2m+1} C_6 H_4 N\right]^+ \cdot \left[CH_3\text{-}(CH_2)_{11}\text{-}OSO_3\right]^- \Leftrightarrow$$
$$\Leftrightarrow \left[C_m H_{2m+1} C_6 H_4 N\right]^+ + \left[CH_3\text{-}(CH_2)_{11}\text{-}OSO_3\right]^-$$
$$\left[C_m H_{2m+1} C_6 H_4 N\right]^+_{membrane} \Leftrightarrow \left[C_m H_{2m+1} C_6 H_4 N\right]^+_{solution},$$
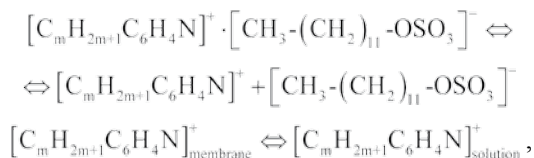
where m = 10 – 18.

Dependence of membrane potential on the concentration of alkylpyridinium cation in the solution is described by the Nernst equation (Кулапина и др., 2008):

$$E = E_0 + \frac{RT}{F} \lg\left[alk^+\right].$$

The electrode functions of solid contact electrodes are linear in the range of 5×10^{-3}–5×10^{-5} mol L^{-1} for DP, 1×10^{-3}–1×10^{-5} mol L^{-1} – for DDP and CP, 1×10^{-4}–1×10^{-6} mol L^{-1} – for ODP. The Fig. 1 shows (as an example) the electrode functions for sensor based on the DDP-SLS in alkylpyridinium salt solutions (DP, DDP, CP, ODP).

The ion selective electrodes exhibit Nernstian response (54–61 mV/pC), thus verifying the transfer of single charged ions.

One of the basic parameters of chemical sensors is selectivity, i.e. the ability of make a specific response to changes of concentration of any component of liquid and gas mixtures (Власов и др., 2000).
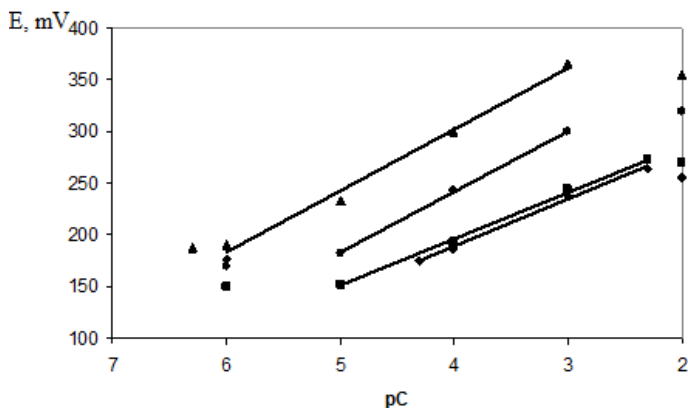
Fig. 1. Electrode functions for the surfactant-selective electrodes in the DP (1), DDP (2), CP (3) and ODP (4) solutions (electrode active component DDP-SLS).

In this article, the method of bi-ionic potentials was used for determination of selectivity coefficients of electrodes based on various ion associates. According to this method selective coefficients can be evaluated by measuring the potential of elements whose external solution contain only salt with main ion or outsider ion with variable concentration. The selectivity coefficient $K_{i/j}$ is calculated by the formula:

$$K_{i/j} = \frac{a_i}{a_j} \cdot 10^{\frac{(E_i - E_j)}{2,3RT}} ,$$

where a_i is activity of the main ion, mol L^{-1}; a_j is activity of the outsider ion, mol L^{-1}; E_i and E_j are voltages of galvanic cell in solutions containing only main and only outsider ions, respectively, mV (Кулапина, 2007; Легин и др., 1999).

Fig. 2 shows the potentiometric selectivity of the used sensors calculated by the method of bionic potentials.

Membranes with studied electrode active components are not selective to the main ion because they are sensitive to outsider ions as well. Values of selectivity coefficients are close to 1 ($lgK_{i/j} \rightarrow 0$), which means that sensors are equally selective to the main and outsider ions.

In addition to selectivity, cross-sensitivity of cationic surfactant sensors in solutions of alkylpyridinium homologues was evaluated as well. In order to make a quantitative evaluation of the said sensors' cross-sensitivity average slope of electrode function S, nonselectivity factor F and reproducibility factor K were calculated: $S = \frac{1}{n}\sum_{i=1}^{n} S_i$, $F = \frac{S}{s^2}$, $K = \frac{1}{n}\sum_{i=1}^{n} \frac{S}{s_i^2}$ (Легин и др., 1999),

where S_i is the slope of electrode function of the sensor in solution of ion No. i; n is the number of ions; s^2 is the mean square deviation of the average slop, which in this case will stand for range of values; s_i^2 is the mean square deviation of S_i. The higher values of these parameters are, the greater cross-sensitivity of the sensor is.
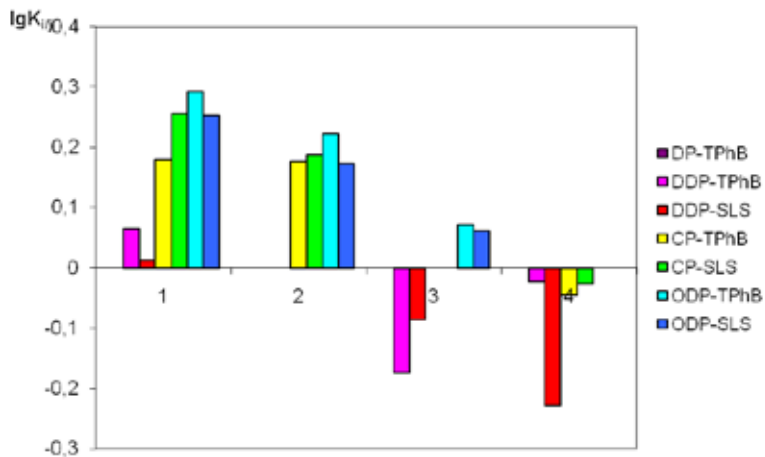
Fig. 2. Coefficients of potentiometric selectivity of surfactant sensors based on various electrode active components in the solutions of outsider ions: DP (1), DDP (2), CP (3), ODP (4).

The slopes of electrode functions in four surfactant solutions (DP, DDP, CP and ODP) were used to calculate the parameters of sensors' cross- sensitivity. The results are shown in Table 2.

Table 2

Cross-selectivity parameters of surfactant sensors

Electrode active component	S, mV/pC	F	K
DP-TPhB	51	1,2	56
DDP-TPhB	54	3,1	78
DDP-SLS	52	1,9	49
CP-TPhB	53	1,8	55
CP-SLS	53	2,4	108
ODP-TPhB	51	1,9	132
ODP-SLS	50	5,4	100

Thus, the membranes are sensitive both to main and outsider ions, which means they are not selective. The sensors meet all requirements for application in «electronic tongue» type multisensor systems: they have low selectivity

and high cross-sensitivity, reproducibility and stability of the electrochemical characteristics.

An array comprised of 7 sensors was used to analyze binary mixtures of alkylpyridinium homologues. Concentration ranges of cationic surfactants were varied in the range $5 \times 10^{-3} – 1 \times 10^{-6}$ M in different ratios. Analytical signals from sensors arrays were treated using artificial neural networks with reverse error propagation in Neuropro 0.25 program. The obtained data was randomly divided into Calibration (17 solutions), Validation (3 solution) and Test (5 solutions) mixtures. Three-layer unidirectional neural networks were used for processing of analytical signals of sensors array. The number of neurons in the input and output layers correspond to the number of sensors in the array and the number of test components, respectively. The results of DP and DDP determination in the binary model solutions are presented in Table 3.

Table 3

The results of simultaneous determination of decylpyridinium and dodecylpyridinium concentrations in two-component test solutions ($n = 3$, $p = 0,95$).

Sample	Introduced, mg·l⁻¹		Found ($\overline{m} \pm \Delta m$), mg·l⁻¹			
	DP	DDP	DP	D, %	DDP	D, %
1	1,02	0,33	1,04±0,03	1,7	0,32±0,02	1,8
2	2,04	1,15	2,04±0,02	0,1	1,14±0,02	0,8
3	6,39	1,64	6,29±0,09	1,6	1,73±0,05	5,3
4	7,67	4,92	7,73±0,08	0,8	4,85±0,07	1,5
5	6,39	8,20	6,40±0,04	0,2	8,29±0,09	1,1

The average error of determination is 0.9% for DP and 2.1% for DDP.

Thus, multisensor method with mathematical data processing (using artificial neutral networks) allows determining concentration of alkylpyridinium homologues in binary mixtures.

REFERENCES:

Кулапина Е. Г. Электрохимические методы анализа : учеб. пособие для студ. хим. фак. Саратов : Изд-во Сарат. ун-та, 2007. 108 с.

Кулапина Е. Г., Чернова Р. К., Кулапин А. И. Потенциометрические сенсоры для определения синтетических поверхностно-активных веществ. Саратов : Научная книга, 2008. 179 с.

Доленко С. А.,Запорожец О. А., Шевченко В. В., Кущевская Н. Ф. Сорбционно-фотометрическое определение катионых ПАВ в воде // Химия и технология воды. 2006. Т. 28. № 2. С. 125–133.

Легин А. В., Рудницкая А. М., Смирнова А. А. Изучение перекрёстной чувствительности плёночных катион чувствительных сенсоров на основе поливинилхлорида // ЖПХ. 1999. Т. 72. Вып. 1. С. 105–112.

Михалева Н. М., Кулапина Е. Г., Колотвин А. А., Лобачев А. Л. Определение гомо-логического распределения алкилбензолсульфонатов натрия в технических препаратах сульфонола // ЖАХ. 2007. Т. 62. № 11. С. 1205–1209.

Перевощикова Н. Б., Азиатцева Ю. А. Количественное определение поверхностно-активных веществ различной природы в водных растворах // Вестн. Удмурт. ун-та. 2010. № 2. С. 54–65.

Heinig K., Vogt C., Werner G. Determination of cationic surfactants by capillary electrophoresis // *Fresenius J. Anal. Chem.* 1997. Vol. 358. № 6. P. 500–505.

Heinig K., Vogt C., Werner G. Determination of cationic surfactants by capillary electrophoresis with indirect photometric detection // J. Chromatogr. A. 1997. Vol. 781. № 1–2. P. 17–22.

Merino F., Rubio S., Perez-Bendito D. Mixed aggregate-based acid-induced cloud-point extraction and ion-trap liquid chromatography–mass spectrometry for the determination of cationic surfactants in sewage sludge // J. of Chromatography A. 2003. Vol. 998. № 1–2. P. 143–154.

Patel R., Patel Kh. S. Simple and specific method for flow injection analysis determination of cationic surfactants in environmental and commodity samples // Talanta, 1999. Vol. 48. № 4. P. 923–931.

Peng Xi-T., Shi Zh.-G., Feng Yu-Qi. Rapid and high-throughput determination of cationic surfactants in environmental water samples by automated on-line polymer monolith microextraction coupled to high performance liquid chromatography–mass spectrometry // J. of Chromatography A. 2011. Vol. 1218. № 23. P. 3588–3594.

Safavi A., Karimi M. A. Flow injection determination of cationic surfactants by using N-bromosuccinimide and N-chlorosuccinimide as new oxidizing agents for luminol chemiluminescence // Anal. Chim. Acta. 2002. Vol. 468. № 1. P. 53–63.

Власов Ю. Г., Легин А. В. Химические сенсоры на пороге XXI века : от единичных «селективных» сенсоров до систем неспецифичных (неселективных) сенсоров («электронный нос», «электронный язык») / Б. П. Никольский. Жизнь труда, школа. СПб. : Изд-во С.-Пб. ун-та. 2000. С. 231–235.

THE EFFECT OF SUBSTITUENT GROUPS ON ELECTRON-DONOR PROPERTIES OF SEVERAL AROMATIC ORGANIC ACIDS: QUANTUM CHEMICAL STUDY

M. V. Pozharov

Saratov State University

1. INTRODUCTION

Today rare-earth metals (REM), including lanthanides, and their compounds have many applications in radio engineering, electronic engineering and both ferrous and non-ferrous metal industry as dopant and effective deoxidizing agents and desulfurizers for steels and other alloys of various composition. Traditionally REM compounds are used as dyes which are used in paints, coatings and glasses (including metal glass) (*Yu H. B., Yu P.,*

Bai H. Y., 2008). They can also be used as dopants for ceramic materials in order to improve their performance characteristics (*Qiu Guanming, Li Xikun, Qiu Tai et al, 2007*). According to (*Parac-Vogt T. N., Deleersnyder K. and Binnemans K., 2004*), several ytterbium (III) salts with aromatic sulfonic acids can be used as catalysts for toluene nitration. REM stearates were proposed to be used as dopants for lubricating oils due to their good antifriction properties (*Захарова Т. В., Макушова Г. Н., Баранова Т. А., Аббакумова С. А., 1999*).

However, the most prominent application of REM compounds is luminescent material production. In the past decade there have been many works dedicated to synthesis of REM compounds with organic ligands and study of luminescent properties of the said compounds (*Tsaryuk V., Zhuravlev K., Zolin V. et al., 2006; Li Hong-Yan, Wu Jing, Huang Wei et al., 2009; Hou Ke-Ling, Bai Feng-Ying, Xing Yong-Heng etc., 2011*). All rare-earth metals possess luminescent properties due to 4f-orbital screening by electrons of 6s-orbital which allows f-electron transfers within 4f-orbital even during low energy excitation. However, the energy emitted during such electron transfers is insufficient to promote durable and intensive luminescence. This problem can be solved by introducing an electron-donor ligand (a substance with an excess of uncoupled electrons) into REM complex. Such substances include both neutral molecules, for example, 1,10-phenantroline (*Xia Li, Chun-Yan Wang and Huai-Ming Hu, 2008*) and 2,2'-bipyridine (*Rogachev A. Yu., Kuz'mina N. P., Nemukhin A. V. et al, 2007*), and anions of aromatic organic acids (*Tsaryuk V., Zhuravlev K., Zolin V. et al., 2006; Rui-Sha Zh., Ling Y., Hong D. et al, 2008*). Theoretical analysis of electron structure of such molecules can be used to predict their potential as electron-donor ligands for REM complexes without the need to perform sometimes expensive and time-consuming experiments.

Thus, the primary objectives of this work are to evaluate electron-donor properties of several aromatic organic acids, namely: salicylic acid, 5-sulfobenzoic acid, 3-amino-5-sulfobenzoic acid, benzenesulfonic acid, 2-aminobenzenesulfonic acid, 3-aminobenzenesulfonic acid and 4-aminobenzenesulfonic acid, and to study the effect of substituent groups on electron-donor properties of these acids.

2. METHOD OF STUDY

Graphic formulas of studied compounds are presented in Fig. 1. Electron structure and geometry of studied compounds were calculated by Gamess-Firefly, a quantum chemical program, using ab initio basis UHF-SBKJC and hybrid DFT basis B3PW91 which, as evidenced by recent work (*Rogachev A. Yu., Kuz'mina N. P., Nemukhin A. V. et al, 2007*), can be used for geometry optimization and further study of molecules which contain an atom of rare-earth metal.
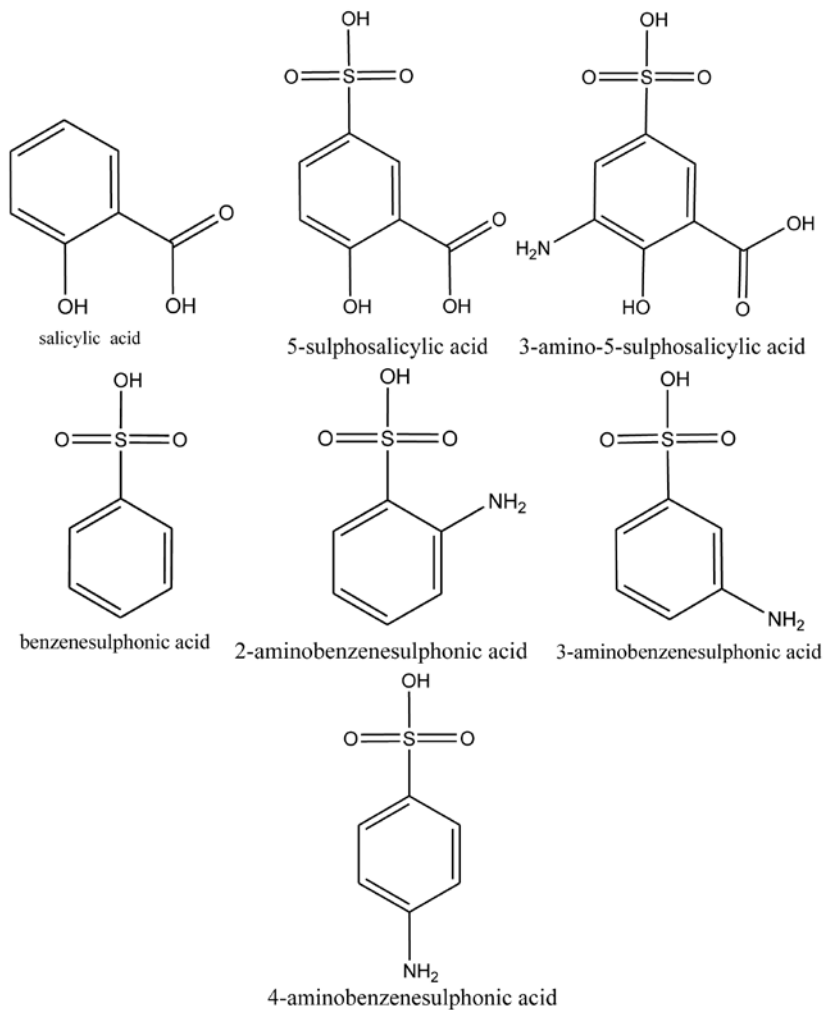
Fig. 1. Graphic formulas of studied compounds

3. RESULTS AND DISCUSSION

According to calculated electron structure parameters of salicylic acid and its derivatives (5-sulfosalicylic and 3-amino-5-sulfosalicylic acids), in salicylic acid electron density is mostly located on carboxylic group which

is evidenced by a relative negative charge on carbonyl carbon (–0,476) and carbonyl oxygen (–0,239) in the said group (see Table 1).

Electron structure parameters of salicylic acid and its derivatives

Compound	$q(C_{carb})$	$q(-O_{carb})$	$q(N)$	$q(O_{-S})$	μ, D
Salicylic acid	–0,476	–0,239	–	–	2,934
5-sulfosalicylic acid	–0,349	–0,188	–	–0,411	9,028
3-amino-5-sulfosalicylic acid	–0,455	–0,221	–0,278	–0,295	4,930

Introduction of sulfonate group into the molecule of salicylic acid leads to decrease of absolute value of negative charge on carbonyl carbon (–0,349) and carbonyl oxygen (–0,188) and emergence of a relatively high negative charge on the atom of oxygen of sulfonate group (–0,411). Moreover, if we compare absolute values of relative negative charges on sulfonate oxygen (–0,411) and carbonyl oxygen (–0,188), we can see that relative negative charge of sulfonate oxygen is much bigger than the carbonyl one. This means that in 5-sulfosalicylic acid electron density is mostly shifted to sulfonate group and that, during lanthanide complex formation, sulfonate group of 5-sulfosalicylic acid will play the primary role. This statement can be proved by data of X-ray structural analysis of praseodymium 5-sulfosalicylate (*Баранова Т. А., 1989*) where it was found out that internal coordination sphere of this complex is comprised by 8 water molecule and 1 molecule of 5-sulfosalicylic acid which is coordinated with lanthanide atom via sulfonate oxygen while carboxylic oxygen did not participate in complex formation. It should also be noted that introduction of sulfonate group into the molecule of salicylic acid leads to significant increase of molecular polarity represented by dipole moment value (which shifted from 2,934 D to 9,028 D).

Introduction of amino group, which has electron-donor properties due to the lone electron pair of nitrogen atom, into 3-position of benzene ring of 5-sulfosalicylic acid leads to the shift of electron density from sulfonate group back to carboxylic group as evidenced by decreasing value of negative charge on sulfonate oxygen (from –0,411 to –0,295) and increasing value of negative charge on carbonyl carbon (from –0,349 to –0,455) and carbonyl oxygen (from –0,188 to –0,221). It should also be noted that introduction of amino group into the molecule of 5-sulfosalicylic acid leads to decrease of dipole moment (from 9,028 D to 4,930 D). This means that electron-donor properties of 3-amino-5-sulfosalicylic acid are much weaker compared to 5-sulfosalicylic acid.

From Table 2 we can see that benzenesulfonic acid is a polar molecule (its dipole moment is 4,965 D) where the relative negative charge is concentrated on sulfonate oxygen (–0,414) and relative positive charge is concentrated on the atom of sulfur (0,395).

Electron structure parameters of benzenesulfonic acid and its derivatives

Compound	$q(N)$	$q(O_{-S})$	$q(S)$	μ, D
Benzenesulfonic acid	–	–0,414	0,395	4,965
2-aminobenzenesulfonic acid	–0,122	–0,390	0,342	6,552
3-aminobenzensulfonic acid	–0,058	–0,413	0,389	5,385
4-aminobenzenesulfonic acid	–0,041	–0,416	0,373	6,734

Introduction of amino group into 2-position of benzene ring of benzene-sulfonic acid, leads to partial shift of electron density to the atom of nitrogen, as evidenced by decreasing absolute values of negative charge on sulfonate oxygen (from –0,414 to –0,390) and positive charge on sulfur (from 0,395 to 0,342). Introduction of amino group also leads to increasing dipole moment (from 4,965 D to 6,552 D) which means that 2-aminobenzenesulfonic acid's molecule is more polar.

Introduction of amino group into 3-position of benzene ring of benzene-sulfonic acid leads to increase of dipole moment (from 4,925 D to 5,385 D), which is, however, not as much as in case of 2-aminobenzenesulfonic acid (6,552 D). Moreover, the introduction of amino group in this case doesn't lead to any significant shifts of electron density (see Table 2).

Introduction of amino group into 4-position of benzene ring of benzene-sulfonic acid leads to conjugation between amino group and sulfonate group which is evidenced by miniscule relative negative charge on nitrogen (–0,041), decrease of relative positive charge on sulfur (from 0,395 to 0,373) and in-crease of dipole moment (from 4,964 D to 6,734 D).

The abovementioned examples show that while introduction of amino group always leads to increase of molecular polarity, its electron-donor po-tential still varies depending on the position of introduced functional group. According to Table 2, electron-donor properties decrease from 4-aminobenze-nesulfonic acid to 2-aminobenzenesulfonic acid and, finally, to 3-aminobenze-nesulfonic acid.

4. CONCLUSION

Electron structure and geometry of several aromatic organic acid mol-ecules, whose anions can be potentially used as electron-donor ligands for REM complexes, have been calculated. According to calculated data, out of all studied substances 5-sulfosalicylic acid possess the best electron-donor properties which is evidenced by the highest value of dipole moment, a big negative charge on sulfonate oxygen and the presence of additional electron suppliers – carbonyl and hydroxyl oxygens. In addition, 2-aminobenzenesulfonic and 4-aminobenze-nesulfonic acids have also proved to have good electron-donor properties.

5. ACKNOWLEDGEMENTS

REFERENCES

1. *Баранова Т. А.* Синтез и физико-химическое исследование РЗЭ с ароматическими кислотами, содержащими амино- и сульфогруппы : дис. … канд. хим. наук. Саратов, 1989. 200 с.
2. *Захарова Т. В., Макушова Г. Н., Баранова Т. А., Аббакумова С. А.* Синтез, физико-химическое исследование стеаратов РЗЭ и испытание их в качестве присадок к смазочным материалам // Изв. вузов : Химия и химическая технологи. 1999. Т. 42. Вып. 6. С. 145–149.
3. *Ke-Ling H., Feng-Ying B., Yong-Heng X. etc.* Synthesis, structure and luminescence of a new series of rigid–flexible lanthanide coordination polymers constructed from benzene sulfonic acid and glutaric acid // Inorganica Chimica Acta. 2011. Vol. 365, Iss. 1, P. 269–276.
4. *Hong-Yan L., Jing W., Wei H. et al.* Synthesis and photoluminescent properties of five homodinuclear lanthanide ($Ln^{3+}=Eu^{3+}$, Sm^{3+}, Er^{3+}, Yb^{3+}, Pr^{3+}) complexes // J. of Photochemistry and Photobiology A : Chemistry. 2009. 208, P. 110–116.
5. *Xia L., Chun-Yan W., Huai-Ming H.* The first example of tetranuclear lanthanide complexes with 2-sulfobenzoate and 1,10-phenantroline // Inorganic Chemistry Communications. 2008. Vol. 11, № 3. P. 345–348.
6. *Guanming Q., Xikun L., Tai Q. et al.* Application of Rare Earths in Advanced Ceramic Materials // J. of rare earths. 2007. Vol. 25. P. 281.
7. *Parac-Vogt T. N., Deleersnyder K., Binnemans K.* Lanthanide (III) complexes of aromatic sulfonic acids as catalysts for the nitration of toluene // J. of Alloys and Compounds. 2004. Vol. 374, Iss. 1–2. P. 46–49.
8. *Rogachev A. Yu., Mironov A. V., Troyanov S. I. et al.* Synthesis, crystal structures and theoretical study of mixed ligand complexes of lanthanides acetylacetonates with o-phenanthroline and 2,2'-dipyridyl : The unexpected inverted electrostatic trend in stability // J. of Molecular Structure. 2006. 789. P. 187–194.
9. *Rogachev A. Yu., Kuz'mina N. P., Nemukhin A. V. et al* Mixed-ligand complexes based on asymmetric gadolinium β-diketonates : Synthesis, crystal structure, and theoretical modeling // Russian Journal of Inorganic Chemistry. 2007. Т. 52, № 9. P. 1365–1377.
10. *Tsaryuk V., Zhuravlev K., Zolin V. et al.* Regulation of excitation and luminescence efficiencies of europium and terbium benzoates and 8-oxyquinolinates by modification of ligands // J. of Photochemistry and Photobiology A : Chemistry. 2006. Vol. 177, Iss. 2–3, P. 314–323.
11. *Yu H. B., Yu P., Bai H. Y.* Lutetium and thulium based rare earth bulk metallic glasses // J. of Non-Crystalline Solids. 2008. 354, P. 4539–4542.
12. *Rui-Sha Zh., Ling Y., Hong D. et al.* Synthesis, structures, luminescence, and magnetism of four 3D lanthanide 5-sulfosalicylates // J. of Solid State Chemistry. 2008. Vol. 181, Iss. 3, P. 567–575.

DYNAMICAL PROPERTIES OF DISCRETE MODELS
(THE IMPACT OF ITERATIONS)

S. A. Startseva

Saratov State University

Introduction

Discrete mappings are significant class of the simplest mathematical models that serves to nonlinear dynamics needs. In general Formula (1.1) represents discrete mapping:

$$x_{n+1} = f(x_n), \tag{1.1}$$

where *n* is number of approximation (discrete time), $n = 0, 1, 2, \ldots, x_0$ is initial approximation (zero-order approximation). Mode, range of definition and range of values of function *f* are specified by experimental data, x_0 is a number, an experimental value that we take as an initial value.

Discrete mappings are applicable for dynamic systems studying in nonlinear dynamics. Dynamic system is a mathematical model that aspires to exact forecast of the future conditions on the basis of current conditions.

Iteration is a repeated influence of the function *f* on the initial value x_0. *K*–th iteration of the function *f* is an influence of the *f* on the $(k-1)$-th approximation x_{k-1}, or it is an influence of the repeated *k* times function *f* on the x_0. Formula (1.2) represents a mathematical expression of the *k*-th iteration (*Danilov*, 2001).

$$x_k = f(x_{k-1}) = \underbrace{f(f(f(\ldots(f}_{k \text{ times}} (x_0 \underbrace{))))\ldots)}_{k \text{ times}} \tag{1.2}$$

Phase space is a set of all states that are possible for the system. Each of possible states of the system corresponds to a point in the phase space.

Attractor is a subset of the phase space of a dynamical system, all trajectories from the subset's certain surroundings of which tend to it as time tends to infinity (*Belyh*, 2004).

Attractor may be a Point Attractor (Fig. 1A), a Cycle Attractor (Fig. 1B), a Torus Attractor (Fig. 1C) which is an infinitely thin thread that winds up on the roll, or a Strange Attractor (Fig. 1D) which is a fractal set in a limited area of phase space (*Barton,* 1994).

Phase space of the system is divided into domains of attraction – *basins of attraction*. Attractor for which the mapping tends to is dependent on initial conditions. In other words, it depends on mapping's basin of attraction under given initial conditions.
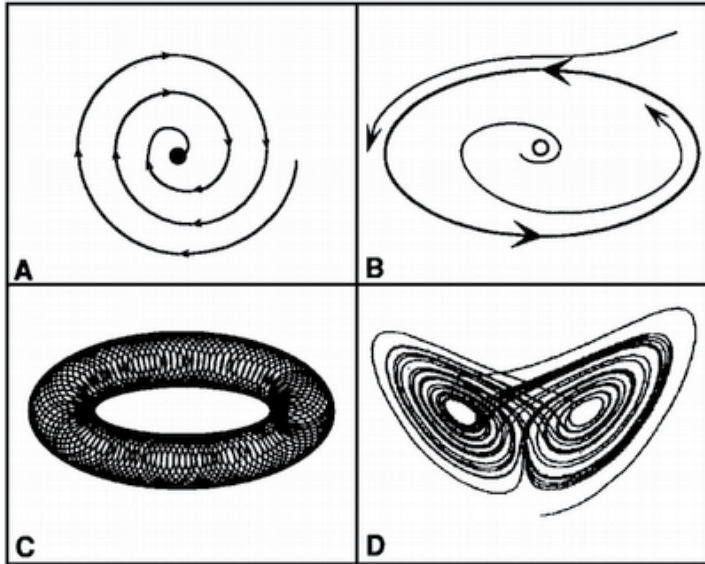
Fig. 1: A) Point Attractor; B) Cycle Attractor; C) Torus Attractor; D) Strange Attractor

Theoretical Part

The computer program «Logistic Map» was designed for the visual study of mapping properties. It allows building iteration diagrams of the logistic map and its iterations. Iterations behavior has shown that *if the period of a cycle and number of iteration has no common multipliers except unity, the iteration has the same mode of the stable equilibrium as the mapping.*

The given statement is easily demonstrable:

Suppose there is a sequence of values with a cycle period N

$$x_1, x_2, x_3, x_4, ..., x_N, x_1, x_2, x_3, x_4, ..., x_N, x_1, x_2, x_3, x_4, ..., x_N, x_1, x_2, x_3, x_4, ..., x_N,$$

We write the $N+1$-th iteration of the following sequence:

$$x_1, \overline{x_2, x_3, x_4, ..., x_N, x_1}, x_2, \overline{x_3, x_4, ..., x_N, x_1, x_2}, x_3, \overline{x_4, ..., x_N, x_1, x_2, x_3}, x_4, \overline{...., x_N}$$

$$x_1, \overline{x_2, x_3, x_4, ..., x_N, x_1}, x_2, \overline{x_3, x_4, ..., x_N, x_1, x_2}, x_3, \overline{x_4, ..., x_N, x_1, x_2, x_3}, x_4, \overline{...., x_N}$$

You can see that the sequence of values has not changed. When choosing the order of iteration $K = q \times N + 1$, where q is a natural number, the numbering of the sequence does not change. Fig. 2 illustrates this case as an example of the first and third iterations of the logistic map. The period cycle N is equal to 2, the iteration order K is equal to 3. Iteration of the first and third order after a transient period has come to the same stable oscillations.

Fig. 2: Iteration diagram in the mode of stable periodical oscillation for the first and third logistic map iterations. Logistic map follows the formula $x_{n+1} = A \times x_n \times (1 - x_n)$, $A = 3.4$, $x_0 \in (0; 1)$.

We write the $N + m$-th iteration, where $1 < m < N$. Period of the stable oscillation remains the same, but the sequence of values has changed. For example, if $K = q \times N - 1$, where q is a natural number, then members of the sequence alternate in the reverse order. The next example illustrates the discussed above case. We take a sequence with a cycle of the period 4 and its 7th iteration:

$$x_1, \cancel{x_2, x_3, x_4, x_1, x_2, x_3}, x_4, \cancel{x_1, x_2, x_3, x_4, x_1, x_2}, x_3, \cancel{x_4, x_1, x_2, x_3, x_4},$$

$$\cancel{x_1}, x_2, \cancel{x_3, x_4, x_1, x_2, x_3, x_4}, x_1, \cancel{x_2, x_3, x_4, x_1, x_2, x_3}, x_4, \cancel{x_1, x_2, x_3, x_4}$$

Practical part

The oscillation cycle period depends on mapping parameters, so the above mentioned thesis verity check is required in all used ranges of parameters. We have developed a computer program especially for this check. On input it has iteration number, parameters and initial conditions ranges, parameters and initial conditions sample rates. On output it pictures a coincidence map. Each point assigns one of the four following values in the space of parameters:

1) a cycle period and a sequence of values have not changed is marked with green color;

2) a cycle period has not changed, but a sequence of values has changed is marked with yellow color;

3) a cycle period has changed is marked with red color;

4)random oscillations in the mapping is marked with grey color.

Also the program shows whether it is possible to replace the mapping by the given iteration without a change of the cycle period in the used ranges of parameters and variables.

Coincidence maps of the second (Fig. 3), third (Fig. 4) and fifth (Fig. 5) iterations of the logistic map are shown below. They completely correspond to the formulated in the theoretical part thesis. Also they show that *iteration and mapping relations depend on the set parameters and the initial conditions, therewith an influence of the initial conditions is unessential and the influence of the parameters is crucial. A stable equilibrium of the mapping is not influenced by the initial conditions in the overwhelming majority of ranges of parameters.*

Coincidence maps of the fourth and sixth iterations are almost completely identical to the coincidence map of the second iteration, as well as a coincidence map of the seventh iteration is identical to the coincidence map of the third iteration, therefore, they are not shown in this work.
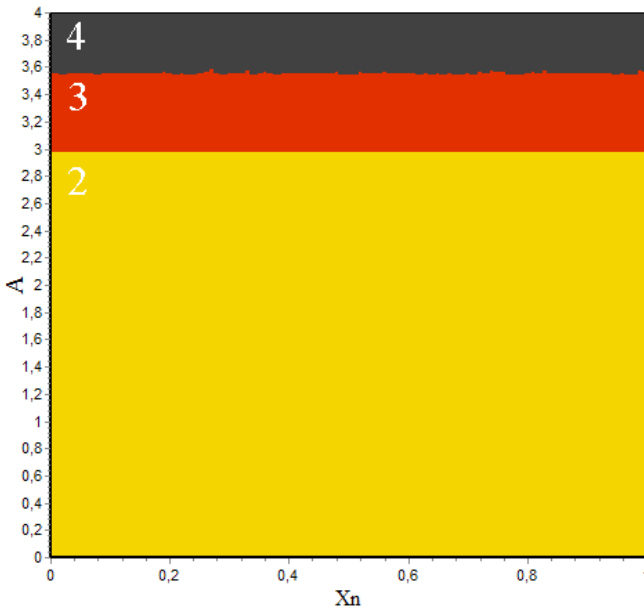
Fig. 3: A coincidence map of the second logistic map iteration; 2 – the cycle period has not changed, but the sequence of values has changed; 3 – the cycle period has changed; 4 – random oscillations in the mapping.
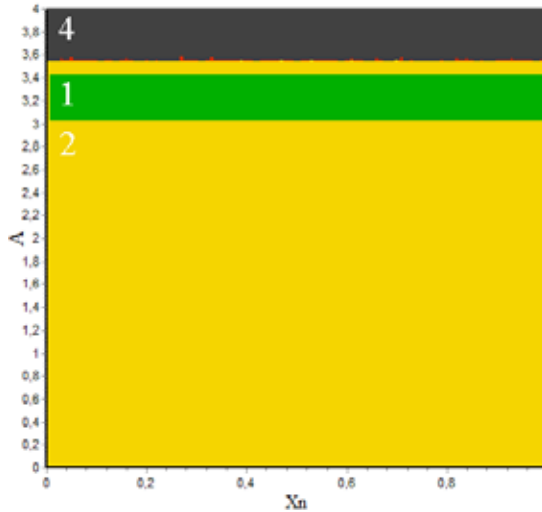
Fig. 4. A coincidence map of the third logistic map iteration; 1 – the cycle period and a sequence of values have not changed; 2 – the cycle period has not changed, but the sequence of values has changed; 4 – random oscillations in the mapping.
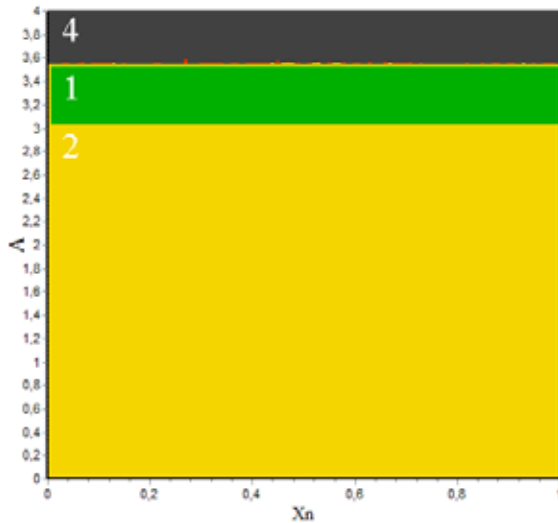
Fig. 5. A coincidence map of the fifth logistic map iteration; 1 – the cycle period and a sequence of values have not changed; 2 – the cycle period has not changed, but the sequence of values has changed; 4 – random oscillations in the mapping.

Advantages of mapping by iteration replacement: duration of the transition period has significantly reduced; a new way to change sequence of values in cycle has appeared.

Lacks of mapping by iteration replacement: computing formula for the following element gets more complicated as iteration order gets higher.

Conclusion

In this article we investigated the dynamic properties of discrete models in various iterations. The theoretical theses are based on properties of sequences and are not connected with mapping mode, so they are valid for each and every mapping. We have developed a computer program to compare properties of mapping and it's iteration in tolerance range of parameters and variables. The program's functionality is shown as research of logistic map properties; however it is possible to preset any other discrete mapping and investigate its properties.

REFERENCES

1. *Belyh V. N.* One-dimensional Mapping : Self-similarity, bifurcations, Chaos // Soros Educational Journal. 2004. Vol. 8(2), P. 106–111.
2. *Danilov Y. A.* Lectures on Nonlinear Dynamics : An Elementary Introduction, Postmarket. M., 2001.
3. *Kuznetsov S. P.* Dynamical Chaos (Lectures), Physmathlit, M., 2001.
4. *Malinetskij G. G.* Mathematical Basics of Synergetics: Chaos, Structures, Computational Experiment, Publishers LKI, M., 2007.
5. *Barton S.* Chaos, Self-organization, and Psychology, American Psychologist. 1994. Vol. 49(1). P. 5–14.
6. *Kronover R.* Fractals and Chaos in Dynamical Systems, Technospheare, M., 2006.

CLOUD POINT EXTRACTION SOME DYES

N. B. Shestopalova, R. K. Chernova

Saratov State University

INTRODUCTION

Extraction as a method for preconcentration and separation is widely used in chemical analysis for the determination of trace level compounds in several matrices. As extractants are the most common organic solvents, but they are toxic, flammable and explosive. In this regard, is the search for new environmentally friendly extractants. One such area is the extraction of micellar phase of nonionic surfactants, based on the extraction of compounds of organic and inorganic nature of the aqueous solutions at a cloud point temperature.

The advantages of this method include the achievement of high preconcentration factors when using small sample volumes and the ability to extract both hydrophobic and hydrophilic substrates. The simplicity and rapidity of the method, good compatibility with the physical – chemical methods of analysis, as well as the environmental safety of the analysis makes the micellar extraction is an alternative to extraction with organic solvents [1].

Upon heating of aqueous solutions of nonionic surfactant to a certain temperature, there is a destruction of hydrogen bonds between the oxygen atoms of polyoxyethylene chain and water molecules. Dehydration leads to a sharp increase in the size of the micelles and the solution becomes cloudy. This temperature is called cloud point temperature. Near the cloud point of emulsion separation begins micellar phase, which is a liquid concentrate, enriched with nonionic surfactant. At slightly higher temperatures, the growth of micelles continues, which leads to phase separation. The result is two phases, one of which is replete with surfactants – micellar phase, which consisting of large micellar aggregates and water, the other – the aqueous phase, in which the surfactant concentration is very low or close to the critical micelle concentration [2]. For the purposes of the concentration of surfactant-rich phase is used.

In the phase separation of nonionic surfactant cloud point temperature affects supplements of strong electrolytes. In this connection, it is interesting changes in the parameters extracted in the presence of these additives.

The aim of this work – to assess the possibility of micellar extraction of some water-soluble food and technical dyes with individual phases of nonionic surfactant OP-10, and in the presence of strong electrolytes.

MATERIALS AND METHODS

We used sodium chloride, indicator bromophenol blue (BFS), analytical grade education Food dyes: tartrazine, sunset yellow FCF, azorubine, green S, indigo carmine were the designs, the basic substance containing not less than 90%. As a nonionic surfactant polyoxyethylated alkylphenol used with an average ethoxylation degree 10–12. The choice of this substance was due to the ability of OP-10 to rapid phase separation during heating solutions. Compact and high viscosity of the micellar phase can easily separate the aqueous phase by decantation. Working solutions were prepared by dissolving exact portions of distilled water.

The absorption spectra of solutions were measured with a spectrophotometer Shimadzu UV – 1800. The acidity of the medium was measured using a pH meter-millivoltmeter 150 МП.

Determination of cloud point and the separation of nonionic surfactant OP-10 was carried out by the following procedure. Aqueous solutions of OP-10 (10%) were placed in test tubes dimensional volume of 10 ml, fixed on a tripod, immersed in a heat-resistant glass with water and heated to 100 ° C at a rate of 1,0 ° C per minute. The temperature was monitored with a thermometer

immersed directly in a water bath. When heated, the water is mechanically stirred to keep the temperature in all parts of the bath was the same. Upon reaching the cloud point (Tc) observed a characteristic opalescence of solutions. With further heating the solutions gradually separation (Ts). Visually observed the formation of two phases.

Micellar extraction of dyes was carried out by a similar method. Aqueous solutions of OP-10, containing all the necessary components were placed in a calibrated dimensional tubes of 10 ml, was heated in a water bath to a temperature of separation. Solutions cooled to room temperature, the aqueous phase was decanted. The distribution of dyes monitored spectrophotometrically. For this measured absorption of aqueous solutions before and after phase separation, and the micellar phase after its dilution. The extent of extraction (R, %) and distribution coefficients (P_0) dyes are calculated.

RESULTS AND DISCUSSION

The phase separation of aqueous solutions of OP-10 (10%) occurs at a temperature around 90ºC. Volume ratio of aqueous and micellar phases is 4. The addition of sodium chloride (5%) lowers the cloud point temperature to 69ºC, and temperature separation to 76ºC, almost without affecting the volume of the aqueous and micellar phases.

Investigation of influence of the acidity of the medium on the phase separation of the OP-10 was carried out at a cloud point temperature in the pH range from 1 to 12. Found that the acidity of the medium has no effect on the character of the phase separation of OP-10 with increasing temperature.
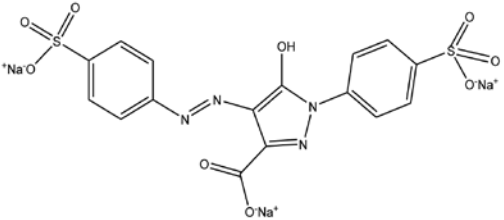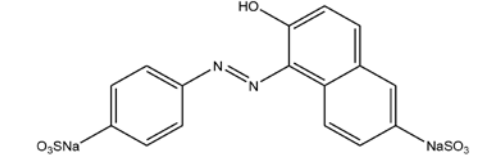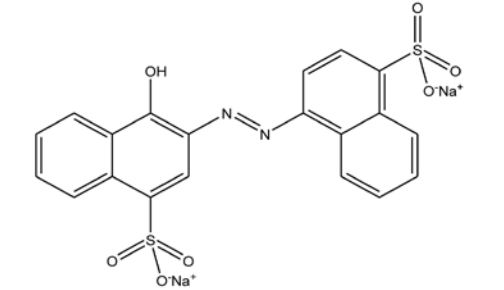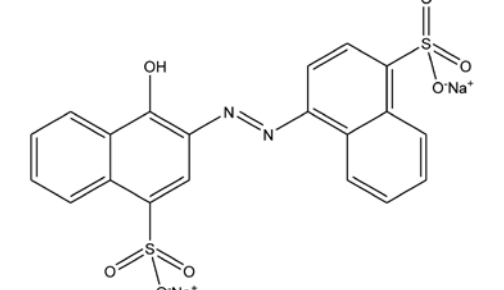
Features micellar extraction at cloud point with phases OP-10 were studied for a number of hydrophilic compounds that are used as food dyes and indicators. Structural formulas are given in Table 1.
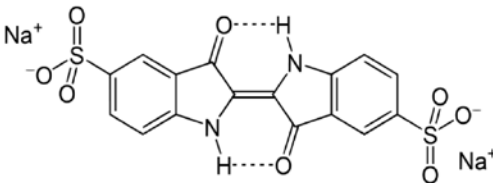
Table 1

The studied water-soluble dyes

Substance	Chemical structure	М.м., g/mol
Acid-base indicator		
Bromophenol blue (BPhB)		669.961

124

Substance	Chemical structure	М.м., g/mol
	Food dyes	
Tartrazine (E102)		534,37
Sunset Yellow FCF (E110)		452,37
Azorubine (E122)		502,43
Green S (E142)		576,62

Substance	Chemical structure	М.м., g/mol
Indigo carmine (E132)		466,36
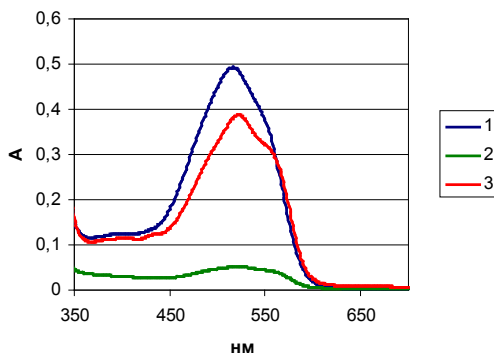
Fig. 1. The absorption spectra of a Azorubine (E122). 1 – original aqueous solution $C(E122) = 1 \times 10^{-3}$ mol·l^{-1}, 2 – aqueous phase after extraction, 3 – solution of the micellar phase. $C(OP\text{-}10) = 10\%$, $C(NaCl) = 5\%$.

Absorption spectra were taken of aqueous solutions of dye and water and the micellar phase in pH 7. Forms of molecular spectras and maximum of absorption for each dye were identical, thus making the assumption of finding them in the different phases in the same manner. In Fig. 1 shows the absorption spectra of the BPhB in aqueous solution and micellar solution after extraction.

The form of the dye in different phases after micellar extraction does not change. The extent of extraction (R,%) and distribution constants (P_0) were calculated. The data obtained are presented in Table 2.

The efficiency of extraction is influenced by the presence of inorganic salts in the system as a salting-out agent. In this regard, we studied the effect of additives of sodium chloride on the extent of extraction dyes. The influence of small concentrations of salting-out agent on the extraction of dyes was studied when added in a solution of 5% NaCl. The data obtained are presented in Fig. 2.

The presence of sodium chloride as the salting-out agent is ambiguous effect on the characteristics of the extraction of dyes, which probably depends on the structure of the dye and its hydrophilic properties.

Quantitative characteristics of the extraction of dyes

Dyes	R, %	P_0
BPhB	94	59,0
Tartrazine	25	0,97
Sunset Yellow FCF	66	3,48
Azorubine	99	314
Indigo carmine	53	2,61
Green S	76	8,77
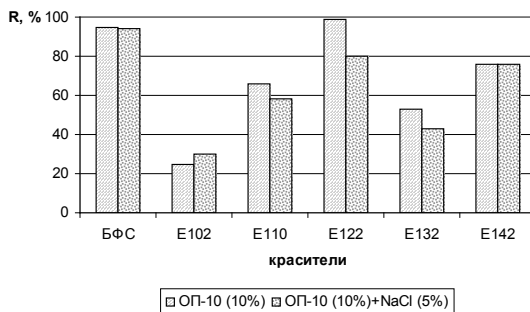
Fig. 2. Effect of NaCl on the extent of extraction of the dyes in the OP-10 at a temperature of cloud point C(OP-10) = 10%, C(NaCl) = 5%.

CONCLUSIONS

The possibility of cloud point extraction of some water-soluble food and technical dyes with phase of the OP-10 at a temperature is shown. The studied systems are suitable for the most efficient extraction of food dye azorubine from aqueous solutions. The extent of extraction of its individual phases of OP-10 exceeds 95%.

REFERENCES

1. *Кущевская Н. Ф., Горбачевский А. Н., Дорощук В. А., Куличенко С. А.* Мицеллярно-экстракционное концентрирование микрокомпонентов фазами неионных ПАВ при температуре помутнения // Химия и технология воды. 2008. Т. 30. № 5. С. 521–543.
2. *Шинода К., Накагава Т., Тамамуси Б., Исемура Т.* Коллоидные поверхностно-активные вещества. М. : Мир, 1966. 330 с.

MECHANICAL AND ELECTRICAL PROPERTIES OF BILAYER GRAPHENE NANORIBBONS: THEORERICAL INVESTIGATION

V. V. Shunaev, O. E. Glukhova, M. M. Slepchenkov

Saratov State University

Introduction

The application of carbon-based materials in various areas of physics research increases and graphene is the one of the brightest and most promising representatives of the carbon materials. Graphene is a two-dimensional structure of atomic thickness, in which carbon atoms are packed in a hexagonal lattice. The discovery of graphene marked the emergence of a new, rapidly evolving science – grafenika. Due to its unique properties graphene structures have a wide range of applications. On the basis of graphene such devices as transistors [1, 2], spin filters [3], supercapacitors [4], memory elements [5] are produced. At the present time the attention of researchers is focused on finding effective ways to control the properties of graphene. In particular, the layered structure of graphene is studied.

It was found that bilayer graphene has high strength properties. On the basis of molecular dynamic simulations with the Brenner methods authors of [6] found that the Young's modulus of bilayer graphene is 0.8 TPa. Also in this work the dependence of the elastic modulus of the bilayer graphene from temperature is revealed. At low temperature (about 20 K) Young's modulus of bilayer graphene is 14% lower than at room temperature. Particular attention is paid to the influence of interlayer sp^3-bonding on the strength properties of bilayer graphene. In [7] molecular-dynamics study of bilayer graphene, the individual atoms of which have sp^3-connection, is carried out. The interaction between atoms is described by method based on the potential REBO, which is well proved in the study of the mechanical properties of carbon structures. The calculations showed that Young's modulus of bilayer graphene with sp^3-bonding is 0.907 TPa, tensile strength and breaking up strength of this structure are 86.55 GPa and 0.135 GPa, respectively.

One of the main features of bilayer graphene is the appearance of an energy gap in the electron spectrum under the influence of an external field. It's showed theoretically and experimentally that bilayer graphene is the first semiconductor controlled by an external energy gap. In the presence of an external perpendicular electric field bilayer graphene is characterized by four energy bands. Two of energy bands are parabolically related to each other at zero energy, so the behavior of particles in graphene is like massless Dirac fermions. In [8] it is found that the energy gap of bilayer graphene spectrum is 0.4 eV according to the results of calculations by quantum-chemical method and 0.34 eV according to ab initio method. Also, it's possible to control the

energy gap of bilayer graphene using a homogeneous deformation, which is applicable to each of the bilayer graphene layers [9]. It's revealed that the energy gap of the spectrum appears only at 14% tensile strain along the edges of graphene armchair and few percents along the edge of graphene zigzag. However, under tension by more than 9% the energy gap of the spectrum starts to decrease. Thus, the energy gap of the spectrum is sensitive to the direction of deformation. The purpose of this paper is to study the mechanical and electronic properties of strained bilayer graphene. In particular, we investigate the effect of axial compression on the properties of bilayer graphene.

Mechanical properties

In order to studying the mechanical properties of bilayer graphene, we applied axial compression deformation to bilayer graphene nanoribbons. The objects of research were zigzag and armchair nanoribbons. Simulation of axial compression was carried by molecular dynamics method using the force field of Amber, which described the interaction of atoms in the structure. Uniform compression proceeded along the longitudinal axis. The velocity of uniform compression was 20m/sec.

Bilayer graphene armchair

Model of bilayer graphene, subjected to axial compression, was simulated by 2 nanoribbons. Each nanoribbon consisted of 646 atoms and had a length of 71Å, width of 22.4Å. The distance between the graphene layers was 3.4 Å. At the initial stage of compression graphene structure retained flat configuration. However, when the magnitude of compression reached 99.4% of the initial length, we observed phase transition: the structure of the waveform became undulating. By compressing the structure up to 98% of the initial length picture of the distribution took an explicit form: nanoribbon of this structure had two half-waves. Geometrical characteristics of bilayer graphene compressed to 98% of the initial length are presented in Table 1.

Table 1

Geometrical characteristics of bilayer graphene armchair compressed to 98% of the initial length

Amount of half-wawes	Amount of atoms in structure	Nanoribbons' length, Å	Half-wawe's length, Å	Half-wawe's amplitude, Å	Amount of hexagones in half-wawe	Half-wawe's width, Å
2	1292	71.0	33.5	3.4	9	22.4

With further compression the atomic structure of bilayer graphene rebuilt again and transformed to one half-wave. This phase transition occurred at a

compression of the structure up to 95%. Subsequent deformation did not cause the changes. We can suggest that the configuration of the structure of bilayer graphene with one half-wave is stable.

We designed map of the local stress of the atoms for considered graphene nanoribbons (Figure 1). We calculated the stress with the original method developed in [9]. It is based on the quantum model of finite-dimensional graphene nanoribbons and empirical method for calculating the energy of one atom. We have found that stress in the 1.7–1.8 GPa is critical for the nanoribbons. Higher stress may cause defects in the form of bond break or atoms' elimination.
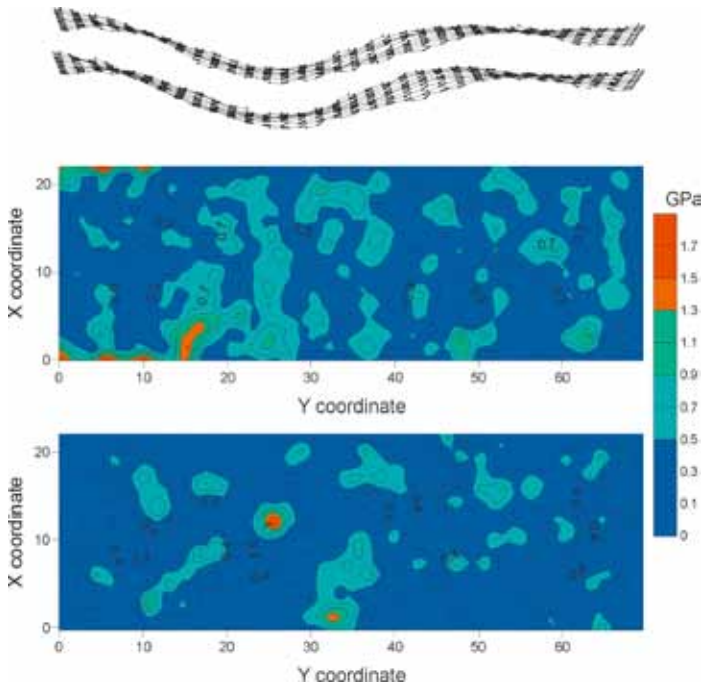
Fig.1. Map of the local stress of the atoms for graphene nanoribbons armchair

Bilayer graphene zigzag

Bilayer graphene zigzag, which is studied in this work, was simulated by 2 nanoribbons. Each nanoribbon consisted of 550 atoms and had a length of 71Å, width of 22.4Å. The distance between the graphene layers was 3.4 Å. Modeling of axial compression had the same scheme as modeling of bigraphene armchair. Phase transition from flat structure to undulating was

observed at 0,4%-compression. At this amount we got two half-wawes on big-raphene's surface. Next compression caused transformation of two half-waves to one. This transition was observed at compression up to 92.8% of the initial length. Geometrical characteristics of bilayer graphene compressed to 98% of the initial length are presented in Table 2.

Geometrical characteristics of bilayer graphene zigzag compressed to 98% of the initial length

Amount of half-wawes	Amount of atoms in structure	Nanorib-bons' length, Å	Half-wawe's length, Å	Half-wawe's amplitude, Å	Amount of hexagones in half-wawe	Half-wawe's width, Å
2	1100	65	33.58	3.4	12	19.88

We calculated the map of the local stress of the atoms for considered graphene nanoribbons.
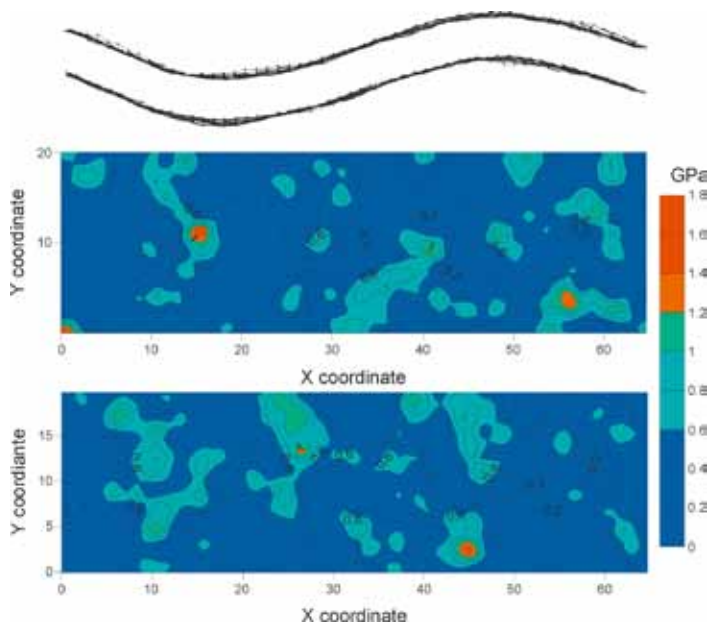
Fig.2. Map of the local stress of the atoms for graphene nanoribbons zigzag

We have found that stress in the 1.7–1.8 GPa is also critical for the bilayer graphene nanoribbons zigzag.

Electronic properties

During the compression process we investigated the changes in the electronic structure of bilayer graphene. Conclusions about the features of the electronic properties of deformed bands were built on the basis of data about the electronic density of states of the structure, in which each orbital is represented as a spectral line, was built to calculate the electronic density of states of the energy spectrum of the structure. Further, each line was replaced by a Gaussian distribution with half-width at given half-maximum of 0.1 eV. The intensities of all distributions for each value of the energy were evolved. The results of calculations for the bilayer graphene nanoribbons zigzag and armchair, compressed to 98% of the initial length, are presented in Figure 3. The vertical line marked level of HOMO (the last filled level).
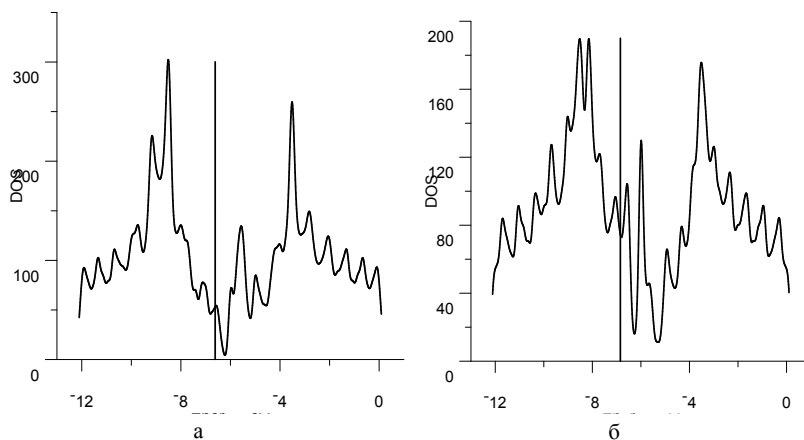
Figure 3. The density of π-electronic states of bilayer graphene: a) armchair type; b) zigzag type

The deformed bilayer graphene armchair is characterized by the increase in the density of states near the HOMO-LUMO levels of the electron spectrum in comparison with the flat bigrafene. For the deformed bilayer graphene zigzag π-density of electronic states near the energy gap practically does not change in comparison to the flat bigrafene. The ionization potential of compressed bilayer graphene nanoribbons is ~ 6.8 eV.

Conclusions

The theoretical study showed that bilayer graphene becomes undulating under compression. The strain at which the pattern of distribution of half-waves took explicit form was 98% of the original length. With further increase

in compression ratio of bilayer graphene nanoribbons we observed the transition from two half-wawes to one. We can say that configuration of bilayer graphene with one half-wave is stable.

For considered graphene nanoribbons we calculated maps of local stresses for the atoms of the deformed structure. It's found that the stress of the 1.7–1.8 GPa is critical for bilayer graphene nanoribbons in different configurations.

Investigation of the electronic structure of compressed bilayer graphene showed that the density of the π-electronic states of bilayer graphene armchair increases near the energy gap in comparison to planar bilayer graphene.

REFERENCES

1. *Stampfer C., Schurtenberger E., Molitor F., Guttinger J., Ihn T., Ensslin K.* Carbon Nanotubes : Synthesis, Properties and Applications // Nano Letters. 2008. Vol. 8. № 8. P. 2378–2383.
2. *Lin Y. M., Jenkins K. A., Valdes-Garcia A., Small J. P., Farmer D. B., Avouris P.* Operation of Graphene Transistors at Gigahertz Frequencies // Nano Letters. 2009. Vol. 9. № 1. P. 422–426.
3. *Saffarzadeh A. , Farghadan R.* A spin-filter device based on armchair graphene nanoribbons // Appl. Phys. Lett. 2011. Vol. 98. P. 023106-1-023106-3.
4. *Wang Y., Shi Z., Huang Y., Ma Y., Wang C., Chen M., Chen Y.* Supercapacitor Devices Based on Graphene Materials // J. Phys. Chem. C 2009. Vol. 113. P. 13103–13107.
5. *Hong S. K., Kim J. E., Kim S. O., Choi S. Y., Cho B. J.* Flexible Resistive Switching Memory Device Based on Graphene Oxide // IEEE Electron Device Letters, Vol. 31. № 9. September 2010. P. 1005–1007.
6. *Neek-Amal M., Peeters F. M.* Nanoindentation of a circular sheet of bilayer graphene // Physical Review B 81. 2010. P. 235421.
7. *Zhang Y. Y., Wang C. M., Cheng Y., Xiang Y.* Mechanical properties of bilayer graphene sheets coupled by sp3 bonding // Carbon. 2011. 49. P. 4511–4517.
8. *Zhang Y., Tang T. T., Girit C., Hao Z., Martin M. C., Zettl A., Crommie M. F., Ron Shen Y., Wang F.* Direct observation of a widely tunable bandgap in bilayer graphene // Nature. 2009. Vol. 459. P. 820–823.
9. *Choi S. M., Jhi S. H., Son Y. W.* Controlling Energy Gap of Bilayer Graphene by Strain // Nano Lett. 2010. 10(9). P. 3486–3489.
10. *Glukhova O. E., Slepchenkov M. M.* Theoretical investigation of didtribution of local stress for grapheme nanoribbons / Nano and Microsystem Technology. 2011. № 7. P. 2–4.

DEVELOPMENT OF TECHNOLOGY FOR OBTAINING PROTEIN ISOLATES FROM NON-TRADITIONAL VEGETABLE RAW MATERIALS

N. V. Vorobieva, I. L. Kazantseva, L. F. Ramazaeva

Engels Technological Institute (branch) Saratov State Technical University

Production of protein products is one of the most steadily developing branches of food industry in the world. Needs of the population in the animal protein are satisfied from other sources because of its deficit, so that role of crop production in the world protein resources is considerable. In 2001–2003, the main source of food protein in the world are grains and legumes (49.5%), oil seeds (23.5%), meat industry (9.7%), dairy farming (4.8%), sea fishing and fish industry (5.4%) (Lishchenko, 2006). Soy protein concentrates and isolates are the most industrially developed food vegetable proteins in the world. There is no doubt that soy protein is one of the most high-grade vegetable food proteins. Although, considering the fact that imports of genetically modified soya continue to play a significant role in supplying soy proteins of Russian industry, the interest in new sources of vegetable protein is growing.

Therefore, chickpea is a promising non-genetically modified high-protein legume for the Saratov region. Chickpea is an undemanding plant which can be easily cultivated and its cost is cheaper than that of soy. Table 1 shows the chemical composition of chickpea grades "Krasnokutskiy 28" and "Priva –1", which are used in the research.

Table 1

Physicochemical properties of chickpea

Index name, unit.	Grade "Krasnokutskiy 28"	Grade "Priva -1"
Mass fraction of moisture, %	9	8.5
Mass fraction of protein, %, in terms of dry matter	24	20.7
Mass fraction of fat, %	3.7	4.3
Mass fraction of ashes, %	3.3	3.15
Mass fraction of starch, %, in terms of dry matter	46	41.8

One of the useful and important properties of chickpea is the chemical composition of protein in its seeds. There are two main indicators for assessing the quality of proteins: content of individual protein groups or fractions and amino acid composition of proteins. For determining individual protein groups in the general protein complex in this paper we used the classical method of Osborn, which is based on unequal solubility of the protein fractions in various solvents (Pleshkov, 1976). The study of fractional compositions of chickpea proteins has found that it consist mainly of albu-

mins (water-soluble proteins) and globulins (salt-soluble proteins) (the total content of these protein fractions is about 96%). Prolamins (alcohol-soluble proteins) and glutelins (alkali-soluble proteins) have been also extracted but their amount is negligible (Table 2).

<div align="right">*Table 2*</div>

Fractional composition of chickpea proteins

Fractions	Mass fraction of cuts, % of sum total of nitrogen extracted by dissolving	
	"Krasnokutskiy 28"	"Priva -1"
Albumins and easily soluble globulins extracted with water	80.2	93.2
Globulins extracted with 1M KCl	16.4	4.87
Prolamins	1.34	0.29
Glutelins	2.01	1.63

Proteins of chickpea seeds are characterized by a high balance of amino acid composition. Basing on the calculation of amino acid score, methionine and cystine are limiting amino acids.

For the extraction of protein isolates from chickpea we used the classical technology, which is based on the isolated extraction of proteins by separating the ballast associated components. The arillus was removed during processing soy seeds at one of the initial stages. It contains a large amount of nondigestible polymer carbohydrates (90%), residual protein (1.5–3.5% according to different researches) and fat (0.5-0.9%) (Begeulov, 2006; Lahmotkina, 2011). Chemical composition of the chickpea arillus was studied to determine the need for the operation of peeling. Table 3 shows the chemical composition of the chickpea arillus and beans peeled from arillus.

<div align="right">*Table 3*</div>

Chemical composition of chickpea beans and chickpea arillus of grade "Krasnokutskiy 28".

Index name	The arillus of chickpea	The beans peeled from arillus
Mass fraction of protein, %	4.9	20.2
Mass fraction of fat, %	0.4	*
Mass fraction of ashes, %	4.1	2.8
Mass fraction of moisture, %	10.9	8.2
Mass fraction of cellulose, %	40.2	*
Mass fraction of starch, %	3.69	*

* Index was not determined.

Data in Table 3 implies that the chickpea arillus of grade "Krasnokutskiy 28" is characterized by sufficiently large content of protein. Removal of arillus will lead to decrease of protein yield. Therefore, in our research for separating the protein from chickpea seeds of grade "Krasnokutskiy 28" peeling operation was not applied.

To determine the conditions of minimum protein isoelectric point solubility of chickpea proteins, we used the following methodology (Pleshkov, 1976, p. 57). The experiment proved that isoelectric point of the dissolved proteins has pH of 4.1–4.4.

Basing on the study of physicochemical composition of chickpea and results of chickpea proteins fractionation, we have selected the rational technological scheme of protein separation from chickpea. It includes the following operations:

1. Beans of chickpea are cleared of impurities, crushed and degreased. Separation of protein from lipids provides increased storage periods, improvement of the functional and organoleptic properties and reduction of cost price. Improvement of organoleptic properties of protein is due to separation of fat-soluble flavoring and aromatic substances, the prevention of formation of products of hydrolysis and oxidation of lipids.

2. Extraction of oil from chickpea grain is carried out with hexane or diethyl ether in two stages. Ratio of chickpea meal to extractant is 1 to 10 in the first stage and 1 to 5 in the second stage. Duration of extraction took 18 hours in the first stage and 4 hours in the second stage.

3. The extract is separated from precipitate by decantation.

4. Extracts from the first and second stages are combined and filtered through filter paper to separate fine suspension.

5. Fat-free chickpea meal is dried on filter paper for two days and then ground in laboratory mill to produce flour.

6. Extraction of protein from fat-free chickpeas flour is performed. Ratio of flour to extractant is 1 to 5, temperature is 20±2°C. Solutions of sodium hydroxide, sodium sulfite, baking soda are tested as extractants.

7. Extract is separated from the insoluble residue pH of extract brought to 4.1–4.4 by titration with hydrochloric (or acetic) acid.

8. Isoelectric sediment is separated by centrifugation at 1000 r/min for 10 minutes.

9. Supernatant is carefully decanted; isoelectric sediment is neutralized to a neutral reaction of medium by titration with 0.5M solution of NaOH.

10. Protein paste is dried at temperature of 40°C to obtain a powdery product, whose physicochemical and functional properties are shown in Table 4.

Standard methods and methodology of investigation of physicochemical indicators of protein isolates and raw materials (chickpea) were used in the work. Functional properties of protein isolates (FHC, WHC, FEC, FFA, SF) were determined by the methodology described in (Alvan, Minakova, Shcherbakov, 1999). Experimental data show that the chickpea protein isolate

has high indicators of many functional properties. It can be used as emulsifier, foaming agent and to improve water- and fat-holding capacity of food system. High functional properties of chickpeas isolates show perspective of its use in food technology of emulsion and whipped type. Comparative analysis of physicochemical and functional properties of chickpea protein isolate and soy protein preparations (Borisova, Barkhatova, Amurov, 2005) industrially produced shows that basic properties of chickpea protein product do not yield analogs and correspond with the performance standards.

Table 4

Parameters of protein isolates from chickpea

Index name	Value
Mass fraction of moisture, %	6.0
Mass fraction of protein, %, in terms of dry matter	90.0
Mass fraction of fat, %	0.4
Mass fraction of ashes, %	4.9
pH of 1% water solution	7.2
Water-holding capacity (WHC), %	400
Fat-holding capacity (FHC), %	142
Fat emulsifying capacity (FEC), %	61
Foam forming ability (FFA), %	39.8
Coefficient of foam forming ability, %	32.1
Foam stability (SF), %	66.7
Foam stability coefficient	0.91

We developed and approved technical specifications TS 9147-003-05286136-11 for the chickpea protein isolate, registered catalog sheet in the Saratov CSM (№ 054/004324 from 14.11.2011).

We investigated and confirmed the obtained chickpea protein isolate in technology of making sausages (Ramazaeva, Kazantseva, 2011), mayonnaise sauces (Potkin, Tyrsin, Kazantseva, Ramazaeva, 2011), meat and vegetable canned food in order to obtain functional foods.

Study of literature data shows that the technology of production of food protein as well as the technology of its processing into food products is at stage of intense formation and improvement. Any of the industrial technology, any of its variants can not be considered finally formed. Analysis of modern tendency and promising area of development of technological decisions of extraction of vegetable proteins, which is made on the basis of literature reviews, allows to identify following perspective trends.

In the production of isolates the application of membrane technology is rather promising for the concentration and cleaning it of unwanted impurities (oligosaccharides, phytates). In obtaining proteinate necessity to use acid to precipitate the protein and alkali for its neutralization disappears; the problems

of cleaning and using waste water are solved; protein yield increases; energy cost for drying are reduced. Ultrafiltrate which is formed by the concentration of protein solution was concentrated by method or reverse osmosis, getting the water used again in the process (Tolstoguzov, 1987).

Recently methods of simultaneous extraction of valuable components from soy beans with water or its fractionation in water media attracted attention. According to data (Tolstoguzov, 1987) the technology of simultaneous water extraction of proteins and lipids from the untrimmed flour which is combined with membrane technology of concentration of protein, gives interesting results.

In order to intensify the operation of extraction, in particular for increasing the yield of protein from defatted flakes it was suggested to use ultrasound technology (Karki, Lamsal, Jung, Pometto, 2010).

To use electro-activated water as reagentless method for producing soy protein concentration (Borisova, Barkhatova, Amurov, 2005) is also interesting.

In view of promising area of improvement of technology of the extraction of food proteins from vegetable raw materials further research work will be aimed at improving the efficiency of the operation of extraction from the solution in order to increase its yield with the use of electrochemical methods.

REFERENCES

1. *Альван А. , Минакова А. Д., Щербаков В. Г.* Функциональные свойства белковых продуктов из семян кунжута // Изв. вузов. Пищевая технология. 1999. № 2–3. С. 17–18.
2. *Бегеулов М. Ш.* Основы переработки семян сои. М. : ДеЛи принт, 2006. 181 с.
3. *Борисова М. М., Бархатова Т. В., Амуров В. С. и др.* Электрохимический способ получения соевых белковых концентратов // Изв. вузов. Пищевая технология. 2005. № 4. С. 68–69.
4. *Дорощенкова М. Л.* Современные технологии получения пищевых белков из соевого шпрота // Пищевая промышленность. 2001. № 4. С. 6–10.
5. *Лахмоткина Г. Н.* Пищевые волокна люпина как ингредиент продуктов функционального питания // Пищевая промышленность. 2011. № 11. С. 29–31.
6. *Лищенко В. Ф.* Мировая продовольственная проблема : белковые ресурсы (1960–2005 гг.). М. : Делипринт, 2006. 272 с.
7. *Плешков Б. П.* Практикум по биохимии растений. М. : Колос, 1976. 256 с.
8. *Поткин Н. А., Тырсин Ю. А., Казанцева И. Л., Рамазаева Л. Ф.* Соусы на основе белкового изолята из нута // Сб. материалов IX междунар. науч.-практ. конф. «Технологии и продукты здорового питания. Функциональные пищевые продукты», Москва, МГУПП. 24–25 ноября 2011 г. М. : Изд. компл. МГУПП, 2011. С. 286–291.
9. *Рамазаева Л. Ф., Казанцева И. Л.* Инновации и перспективы производства и применения продуктов переработки нута // Хранение и переработка сельхозсырья. 2011. № 3. С. 67–71.
10. *Толстогузов В. Б.* Новые формы белковой пищи. М. : Агропромиздат, 1987. 303 с.
11. *Karki B., Lamsal B. P., Jung S., van Leeuwen J., Pometto A. L.* Enhancing protein and sugar release from defatted soy flakes using ultrasound technology // J. Food Eng. 2010. 96. № 2. С. 270–278.

DIGITAL HOLOGRAPHIC MICROSCOPY

Y. V. Tarakanchikova, S. A. Savonin, V. P. Ryabukho

Saratov State University

Introduction

Digital hologram techniques of registration and wave-front reconstruction have considerably developed during last years. In ordinary schemes of holography register in the presence of a coherent reference wave a light field from a subject, essentially diffuses owing to diffraction or diffusive dispersion. However the basic feature of holography connected with the possibility of preservation of the information on phases of waves diffused by a subject, is exhibited as well as a reference wave on a plane of the sharp (focused) image. Holograms of the focused images possess a number of specific features keeping the property of registration.

Experiment statement

Feature of record of digital holograms consists of thenecessity of the speckle resolution of image structure of the object and hologram interference structure. The strong speckle noise is connected with essentially smaller resolving power of digital CMOS sensors (50–100 lin/mm) in comparison with classical photosensitive materials. From the theorem of Kotelnikov the basic condition of record of the digital hologram, including the necessity of use of small enough corners between reference and objective waves [1]:

$$\theta_{max} \sim \frac{\lambda}{2\Delta x} \tag{1}$$

where Δx is the distance between pixels. In our experiments is $\theta_{max} \leq 5.6$.

The scheme of registration digital lensless Fourier holograms of the focused images is resulted on fig. 1. The coherent light of a laser is divided into a wavefront set carried out in a way that essentially simplifies realization of a method of digital holography [2–5].

The bunch He-Ne of laser *LSR* is collimated by system of lenses *L1-L2* and divided into object and reference waves. The object wave is weakened by neutral filter *F1*, propagated through investigated phase object *C*. Object lens *LO* forms the image of investigated object on a plane of a matrix of digital sensor *CMOS*. The reference wave propagates through lens *LR* and weakened by filter *F2*, used reflection in system of mirrors *M1-M2*, and is focused on back focal plane *FP* of lens *LO*. Both waves, propagate through neutral filter *F3*, are blocking at a small angle in a plane of a matrix of sensor *CMOS*.
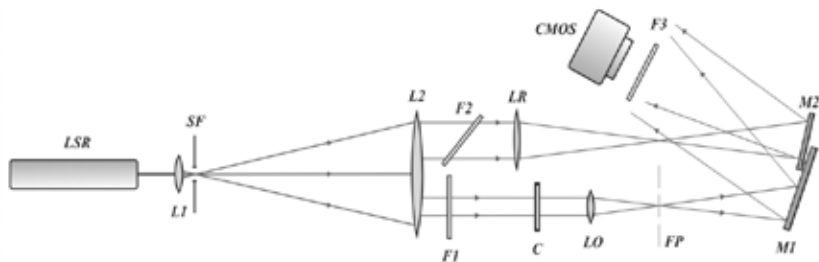
Рис. 1. The scheme of registration of the digital hologram of the focused image: LSR – He-Ne laser; SF – spatial filters; L1-L2 – collimator; F1,F2,F3 – neutral filters; C – phase object; LO – object lens; LR – reference lens; FP – focal plane of lens LO; M1,M2 – mirror; CMOS – digital sensor.

The developed software allows us to realize procedures of numerical reconstruction of complex amplitude and intensity of an objective field in a plane of image, from the written down digital hologram, and also the subsequent multiexposition interference analysis of dynamics of change of phase object. The digital hologram (fig. 2) as the distribution matrix intensity on a plane of a matrix sensor control is exposed as discrete Fourier to transformation which is defined by expression:

$$U_D(\xi,\eta) = \sum_{x=0}^{M-1}\sum_{y=0}^{N-1} I(x,y)U_r(x,y)\exp\left(-i2\pi\left(\frac{x\xi}{M}+\frac{y\eta}{N}\right)\right) \qquad (2)$$

$U_r(x,y)$ is complex amplitude reconstruction plane; $\xi = 0, 1, 2, ..., M-1$ and $\eta = 0, 1, 2, ..., N-1$.

This is the result of calculated Fourier massif representing a complex spectrum of spatial frequencies of the hologram (fig. 3). The spatial frequencies from the given spectrum corresponding to an objective field (fig. 4) are allocated. The filtered spectral range is exposed to the second Fourier transformation for reconstruction of complex amplitude of a field of the focused image of object.
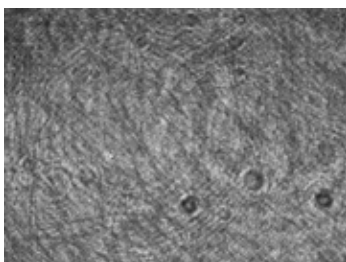
Рис.2. Digital hologram
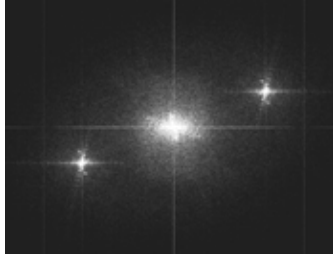
Рис.3. Spectrum of spatial frequencies of the hologram
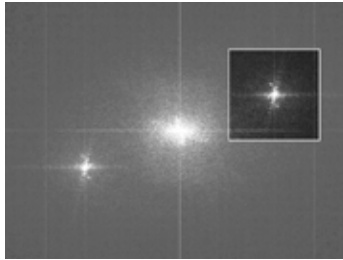
Рис.4. Spatially the frequency filtration of the hologram

The digital holography keeps the main advantage of classical holography which is the possibility of reconstruction of complex amplitude of an objective field allows to carry out interference research of controllable phase object. The picture of fringes – a digital interferogram – reflects phase changes of investigated object.

Research of modeling system

The developed method was applied to research of kinetics of morphology of RBC (red blood cells). As the investigated sample blood dab is taken. Formed digital interferograms qualitatively and quantitatively show changes of the form of RBC of blood under the influence of different factors.
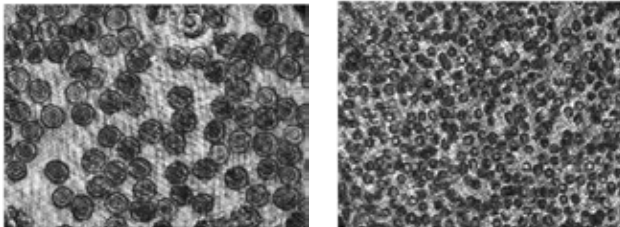
Рис.5. Digital interferograms

141

Investigations show that the morphology of RBC is an important parameter which displays the general condition of biological systems and level of their response to action of artificial and natural factors, and also pathological changes of organism.

Conclusion

The original scheme of registration digital lensless Fourier holograms of the focused images for research of dynamics of changes of phase objects is introduced. The software is developed for realization of procedure of numerical restoration of complex amplitude and intensity of an objective field in a plane image.

REFERENCES

1. *Басараб М. А., Зелкин Е. Г., Кравченко В. Ф. и др.* Цифровая обработка сигналов на основе теоремы Уиттекера-Котельникова-Шеннона. М. : Радиотехника, 2004, 72 с.
2. *Shaked N. T., Newpher T. M., Ehlers M. D., et al*. Parallel on-axis holographic phase microscopy of biological cells and unicellular microorganism dynamics // Appl. Opt., 2010. Vol. 49. № 15. P. 2872–2878.
3. *Marquet P., Rappaz B., Magistretti P. and et al*. Digital holographic microscopy: a non-invasive contrast imaging technique allowing quantitative visualization of living cells with subwavelength axial accuracy // Optics letters. 2005. Vol. 30. № 5. P. 468–470.
4. *Kemper B., von Bally G.* Digital holographic microscopy for live cell applications and technical inspection // Appl. Opt. 2008. Vol. 47. № 4. P. 52–61.
5. *Dubois F., Schockaert C., Callens N. et al.* Focus plane detection criteria in digital holography microscopy by amplitude analysis // Optics Express. 2006. Vol. 14. № 13. P. 5895–5908.

CONTENT

УДК 5(082)
ББК 20я43
  П71

В данном сборнике опубликованы материалы участников секции естественных наук научной конференции молодых ученых «Presenting Academic Achievements to the World», которая состоялась в Саратовском государственном университете 14-15 марта 2012 года. В сборник включены статьи с результатами исследований в области физики, химии, географии, геологии и информационных технологий.

This publication assembles papers given at the conference for young scientists «Presenting Academic Achievements to the World» which was held in March 14-15, 2012 at Saratov State University. The articles present the results in such fields of natural science as Physics, Chemistry, Geography, Geology and Information Technology.

Работа издана в авторской редакции

Саратовский государственный университет им. Н. Г. Чернышевского

Представляем
научные достижения миру.
Естественные науки

Материалы научной конференции молодых ученых
«Presenting Academic Achievements to the World»

Март 14–15, 2012
Саратов

В ы п у с к 3